3-14-2007

Spacecraft Proximity Operations Used to Estimate the Dynamical & Physical Properties of a Resident Space Object

Abraham F. Brunner

SPACECRAFT PROXIMITY OPERATIONS USED TO ESTIMATE THE DYNAMICAL & PHYSICAL PROPERTIES OF A RESIDENT SPACE OBJECT

THESIS

Abraham Franz Brunner, First Lieutenant, USAF

AFIT/GA/ENY/07-M03

DEPARTMENT OF THE AIR FORCE
AIR UNIVERSITY

AIR FORCE INSTITUTE OF TECHNOLOGY

Wright-Patterson Air Force Base, Ohio

The views expressed in this thesis are those of the author and do not reflect the official policy or position of the United States Air Force, Department of Defense, or the United States Government.

AFIT/GA/ENY/07-M03

SPACECRAFT PROXIMITY OPERATIONS USED TO ESTIMATE THE DYNAMICAL & PHYSICAL PROPERTIES OF A RESIDENT SPACE OBJECT

THESIS

Presented to the Faculty

Department of Aeronautics and Astronautics

Graduate School of Engineering and Management

Air Force Institute of Technology

Air University

Air Education and Training Command

in Partial Fulfillment of the Requirements for the

Degree of Master of Science in Astronautical Engineering

Abraham Franz Brunner, B.S.

First Lieutenant, USAF

March 2007

AFIT/GA/ENY/07-M03

SPACECRAFT PROXIMITY OPERATIONS USED TO ESTIMATE THE DYNAMICAL & PHYSICAL PROPERTIES OF A RESIDENT SPACE OBJECT

Abraham Franz Brunner, B.S.

First Lieutenant, USAF

Approved:

William E. Wiesel 14 Mar 07

Dr. William E. Wiesel — Date
Thesis Advisor

14 MAR 07

Dr. Jonathan Black — Date
Committee Member

14 Mar 07

LtCol Kerry Hicks, Ph.D. — Date
Committee Member

Abstract

When conducting a space proximity operation, developing high-fidelity estimates of the dynamical and physical properties of a Resident Space Object (RSO) based on post-rendezvous observational data acquired, is imperative for the understanding of the RSO itself and the operating environment. This research investigates the estimation of relative motion dynamics, rotational dynamics, and the feasibility of estimating the moments of inertia of a RSO. Using the Hill-Clohessy-Wiltshire equations, rigid-body dynamics, and estimation theory, a nonlinear least squares estimation algorithm is implemented in the processing of range data from tracked observation points on the RSO body. Through simulation, it was determined that accurately estimating the relative motion and rotational dynamics is possible. However directly estimating the moments of inertia using range data proved to be problematic and exposed a possible observability limitation. Yet in general, the solutions were heavily dependent on the quality of the *a priori* knowledge as well as the reduction of solution ambiguity through the use of multiple observational data sets.

Ich widme diese Arbeit meinen lieben Eltern.

Acknowledgements

For the creative, humorous, and always interesting advice, conversation, and historical insight, I must thank my advisor, Dr. William Wiesel. It has truly been a privilege to be a student of this brilliant professor. I would like to acknowledge my committee members for their guidance. I am also grateful to my classmates for making this a memorable experience.

Special thanks goes to my sister and niece for their laughter and advice and to my mother for her love and support. Thank you Lord.

Abraham Franz Brunner

Table of Contents

List of Figures

List of Tables

List of Symbols

Symbol Page

List of Abbreviations

SPACECRAFT PROXIMITY OPERATIONS USED TO ESTIMATE THE DYNAMICAL & PHYSICAL PROPERTIES OF A RESIDENT SPACE OBJECT

I. Introduction

Major advances in the area of relative navigation and rendezvous are leading to new applications of spacecraft missions which will greatly further our capability to operate in space. With the developing engineering and technology of autonomous rendezvous missions, the next logical step is conducting autonomous proximity operations on or about a Resident Space Object (RSO). This is a very exciting and promising field with incredible futuristic applications for both the civilian and the military space communities. Conducting a proximity operation requires the performing spacecraft to carefully function in a very active and dynamic environment; where typically, very little is known for certain. The complexity of the operating environment can be successfully managed if the dynamical parameters required to operate near the RSO can be accurately characterized and understood [1]. Whether the proximity mission is solely limited to making observations of the RSO or if the observation activity is a precursor to a more involved and intrusive stage of a proximity mission, understanding the dynamics and physical properties of the RSO provides valuable insight into the operating environment, as well as the RSO itself.

This thesis will explore the use of nonlinear least squares theory to estimate the dynamical and physical properties of a RSO. Specifically, the relative motion dynamics, rotational dynamics, and moments of inertia will be estimated using range observations made by an observing spacecraft performing a space proximity operation in the vicinity of the RSO.

1.1 A Historical Perspective

Several milestone space programs in the history of astronautics have led to today's advances in autonomous rendezvous and ultimately to the feasibility of performing autonomous proximity operations and observations. First demonstrating the initial concepts of rendezvous and docking techniques were the Gemini and Apollo programs [2]. The Space Shuttle program then furthered the versatility and frequency of rendezvous and proximity operation missions in low earth orbit (LEO) [2]. The move from a human-controlled operation to a new era of autonomous rendezvous and autonomous proximity operations has been underway as seen in recent programs such as the XSS-11 mission and the Hayabusa mission [2, 3].

1.1.1 The Gemini & Apollo Programs. In 1965, a modified Titan II Intercontinental Ballistic Missile (ICBM) booster launched the first Gemini mission from Cape Canaveral [4]. This program led to the first American space walk; and in December of 1965, the revolutionary rendezvous and docking concept was demonstrated by the joint rendezvous mission of the Gemini VI and Gemini VII spacecrafts [5, 4]. Prior to the conclusion of the Gemini program in 1966, work had already begun on the Apollo program. This manned program used the rendezvous techniques learned during the Gemini program as the foundation for the mission to the Moon. In the Apollo Moon mission, after leaving the Lunar surface, the Lunar Excursion Module (LEM) was required to rendezvous and dock with the Command Service Module (CSM) using radar during long-range separations and crew observations for the final docking stages [2]. Zimpfer *et al.* [2] explains further that the rendezvous calculations were performed on the ground while the on-board system was able to automatically control thruster firings. Again, the terminal phase of capture between the LEM and CEM was manually controlled by the on-board crew. The Apollo program demonstrated the fundamentals of guidance, navigation, and rendezvous & capture, with minimal computer power that still serves as the foundation for today's concepts.

1.1.2 Space Shuttle Program. Perhaps one of the most well known space vehicles today, the Space Shuttle has repeatedly demonstrated the ability to rendezvous in LEO and perform what could be considered the start of proximity operations since the 1980's. Major rendezvous and proximity operations accomplished by the Space Shuttle Program include the Discovery STS-51I mission in 1985, where the Shuttle crew captured, repaired, and redeployed the SYNCOM IV-4 (LEASAT-4) communications satellite [6]. In years following, the Orbiter has docked with the Soviet-made Mir space station and the International Space Station (ISS). In general, the rendezvous maneuver sequence is planned by ground operators, and with crew command, executed by the on-board Guidance Navigation & Control (GN&C) system [2]. The GN&C system performs rendezvous functions, relative navigation, targeting, and control; yet, the Orbiter crew manually performs the final docking maneuvers using visual aids and data from a LIDAR Trajectory Control Sensor [2]. Including the Space Shuttle program and prior programs, the level of computer and sensor technology involved in actually *performing* the rendezvous and proximity operations has increased dramatically. Yet the final stage, the action defining a space proximity mission, still remains in the control of a human operator performing the final action *using* today's available computing and sensor technology.

1.1.3 Recent Programs. In recent years there have been several programs designed to explore autonomous navigation and autonomous proximity operations and planning. Some of these missions include the Experimental Satellite System-11 (XSS-11) of the USAF and the Japanese Hayabusa mission [2, 3].

The USAF Air Force Research Laboratory (AFRL) and Lockheed Martin Space Systems Co., Waterton, CO, developed the XSS-11 spacecraft to demonstrate autonomous rendezvous, autonomous proximity operations, and autonomous mission planning. Launched by a Minotaur I booster in April 2005 from Vandenberg Air Force Base, the spacecraft successfully performed proximity operations with its expended upperstage from distances between $500\,m$ and $1.5\,km$ [7]. The spacecraft has

performed over 75 natural motion circumnavigations of the Minotaur upperstage [7]. XSS-11 uses advanced on-board planning and guidance algorithms including an event planner, a monitor & forward thinking resource manager, and a proximity operations guidance system developed by Draper Laboratory [2]. The 100-kilogram spacecraft is equipped with an active LIDAR sensor and a passive camera used for relative navigation [2, 7]. Figure 1.1 shows an image taken by the 30-kilogram XSS-10 spacecraft (the predicessor of the XSS-11) of its Boeing Delta II upperstage in 2003. Figure 1.2 is from an image taken by the XSS-11 spacecraft of its Minotaur upperstage from a distance of 500 meters with the Earth in the background [7].

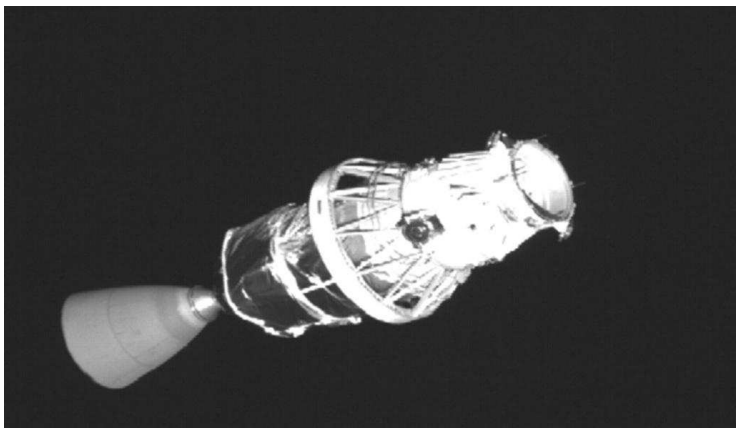

Figure 1.1 XSS-10 Image of Delta II Upperstage (USAF Photo)

Figure 1.2 XSS-11 Image of Minotaur Upperstage (USAF Photo)

In May 9, 2003, the Hayabusa (MUSES-C) spacecraft was launched with a M-V booster from the Kagoshima launch site by the Japan Aerospace Exploration Agency (JAXA) [8]. The Hayabusa spacecraft was developed for a sample return mission to the asteroid *Itokawa* (25143), named after the late Dr. Hideo Itokawa, considered the father of the Japanese space program [8]. The mission is being used to demonstrate technology needed for the spacecraft to autonomously retrieve scientific samples from a small celestial body and return the sample back to Earth. JAXA states that the Hayabusa mission objectives are to demonstrate the following four key technologies: interplanetary travel using ion engines, autonomous navigation and guidance using optical measurements, sample collection under micro gravity from *Itokawa*, and direct re-entry to Earth from an interplanetary orbit [3]. After successfully navigating itself to the asteroid without human guidance, the spacecraft began its proximity operations and had autonomously observed the asteroid by hovering 7 to 20 kilometers above its surface [8]. Using a Telescope Wide-View Camera, LIDAR, and a Near-Infrared Spectrometer, Hayabusa has mapped the surface of the asteroid and its features so that its geometry, mass properties, and composition can be determined [3, 8]. Figure 1.3 shows an image of the asteroid taken by the Hayabusa spacecraft camera from a distance of approximately 8 kilometers [3].

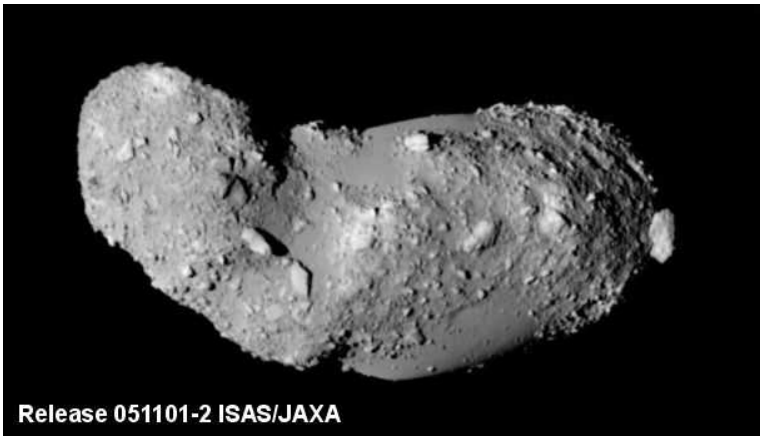

Figure 1.3 Asteroid Itokawa (courtesy of JAXA)

1.2 Applications

In a paper written by D.J. Scheeres [1], he explains the difficulty of a spacecraft or surface vehicle operating in the vicinity of a small solar system body. Mainly, the difficulty is due to a lack of knowledge and uncertainty of the physical characteristics of the Target body and its possible chaotic dynamical environment[1]. Scheeres writes, "To successfully carry out close proximity operations about these bodies requires an understanding of the orbital dynamics close to them, a knowledge of the physical properties of the body and the spacecraft, and an appropriate level of technological sensing and control capability onboard the spacecraft [1]." Having the ability to derive and estimate physical and dynamical properties of an RSO based on post-rendezvous observations has obvious civilian and military applications. In all cases, the pre-programmed model of the operating environment formed by Earth-based sensor data (including the dynamics of the Target) can be updated by the Observer with a more accurate data set in real-time; thereby, reducing the uncertainty of the operating environment. As with the Hayabusa mission, a civilian application requiring the need to understand the physical properties and dynamics of an asteroid or small moon is a sample return mission. Closer to Earth, the inspection of space-based assets, such as the ISS, Hubble telescope, etc., could be made allowing for repair or servicing. Possible non-aggressive military applications, for a maneuverable and autonomous spacecraft capable of collecting observational data and making physical and dynamical estimates of a Target range from damage inspection of larger US satellites, on-orbit repair, re-fuelling, and possibly RSO identification and characterization.

1.3 Key Terms

This section will define and elaborate on key terms and concepts referred to in this research. A general definition for proximity operations and dynamical &

physical characterization is given below as well as clarification on nomenclature used in this thesis.

1.3.1 Space Proximity Operations. In general, spacecraft proximity operations is defined in this research as one or more spacecraft bodies conducting an activity in the close vicinity of a RSO. The solution to the relative motion of the spacecraft and RSO operating in close proximity to each other is given by the Clohessy-Wiltshire equations [9]. These relative motion equations along with their assumptions are explained in Chapter 2. Although no specific and agreeable definition was found in the literature quantifying the terms *proximity* or *vicinity*, dynamically, Equation 2.5 must be satisfied for the Clohessy-Wiltshire equations to hold true. It would be acceptable to say that relative distances measured in the order of $\sim 10^3$ meters or less could be classified as proximity operations. Traditionally, the passive body of interest, in which the observations or operations are being conducted on, is termed the *Target*. The body (i.e. spacecraft) that is actively performing the proximity operations (e.g. observations) is termed the *Chaser*. Other terms typically found in literature refer to these bodies as *Chief & Deputy*, *Master & Slave*, and *Target & Observer*, respectively. This paper will use the terms of *Target & Observer*; where the *Observer* is a spacecraft performing the proximity operation and the *Target* is the Resident Space Object of interest. Post-rendezvous, the Observer spacecraft will position itself in the vicinity of the Target in preparation to carry out its proximity operation mission. In general, proximity operations may include specific activities such as taking measurement observations of the Target, docking with the Target to make repairs, or performing a scientific return sample mission. In this thesis, the proximity activity is taking observable range measurements of the Target as explained in later sections.

1.3.2 Spacecraft Proximity Sensors. A spacecraft performing proximity operations would be equipped with a sensor suite used to perform standard attitude

control and relative navigation which would be needed to travel to the point of rendezvous where the proximity mission would take place. This sensor suite commonly includes some of the following: a sun sensor, earth sensor, star sensor, ring laser gyro, magnetometer, and Global Positioning System (GPS) unit [10]. The use of a star sensor (i.e. star camera) is a method of far-range photogrammetry where the distance setting of the source is essentially infinity and object measurements are made from photographic images or line-of-sight measurements. The use of close-range photogrammetry, where the distance of the source is finite, can be employed to determine position *and* attitude of an object; where as, far-range photogrammetry can only be used to estimate attitude [11]. Close-range photogrammetry was used for the the XSS-10, XSS-11, and Hayabusa missions. Using photogrammetry and pattern-recognition methods, position, attitude, and physical feature information can be derived from the imaged target, passively.

Another essential sensor for space rendezvous and proximity activities is the scanning Light Detection and Ranging (LIDAR) instrument. Rendezvous Laser Vision (RELAVIS) and the Rendezvous Laser System (RLS) scanning LIDAR technology, built by Optech Inc., Ontario, Canada, was used on the XSS-11 mission as the active rendezvous instrument and similar LIDAR technology is planned for use on the Mars Sample Return mission (MSR) mission as the primary instrument for autonomous rendezvous [12]. An example of LIDAR specifications are shown in Table 1.1 [12].

Table 1.1 LIDAR RELAVIS Instrument Specifications (Optech Inc.)

Min Range	0.5 m
Max Range	5000 m
Mass	15 kg
FOV	10 deg
Sample Rate	5 Hz
Range Accuracy	1 cm
Bearing Accuracy	0.35 mrad
Attitude Accuracy	1 deg

A scanning time-of-flight LIDAR sensor uses a pivoting mirror to steer laser pulses sent and then measures the optical time-of-flight required for the pulses to return and illuminate the focal plane array along with measuring the angle of reflection. This type of LIDAR sensor provides range and bearing of the target and can also be used to render a three-dimensional point-cloud image of the RSO. The Hayabusa spacecraft combined LIDAR range data with camera imagery to accurately estimate the spacecraft's position relative to the asteroid [3]. Figure 1.4 shows a data cloud image of the asteroid *Itokawa* created from the LIDAR range measurements taken by the spacecraft and plotted against a model developed by S. Ostro *et al.* using ground-based radar [3].

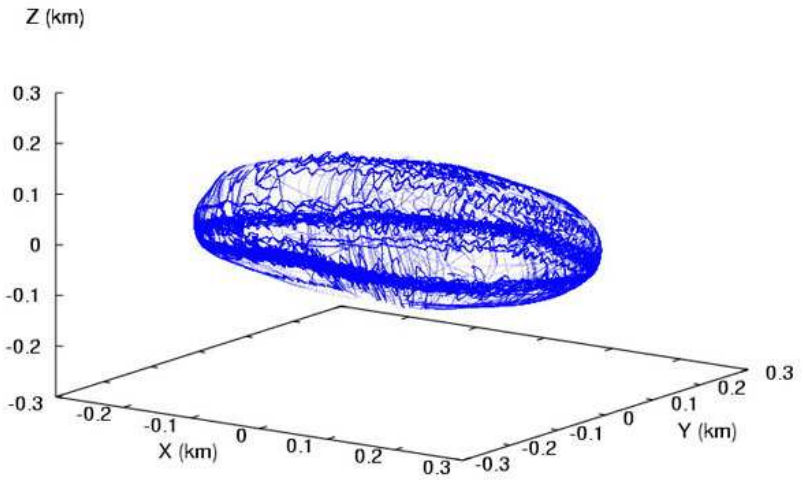

Figure 1.4 LIDAR Data Cloud of Asteroid Itokawa (courtesy of JAXA)

This 3-D shape model was developed while the spacecraft made its early observations on the asteroid's equatorial plane. As a result, insufficient data models the characteristic neck of the asteroid in the polar regions as seen by the optical navigation camera image shown earlier in Figure 1.3 [3]. Additional data fusion will eventually resolve this.

To explore the meaningfulness and possible limitations of minimal data types, this research will assume that the only available data from the sensors of the Observer spacecraft are *range* measurements of the RSO during a finite period of time when the proximity operation occurs.

1.3.3 Physical & Dynamical Properties. For this research, the physical properties of the target body are specifically limited to the moment-of-inertia components of the RSO. The dynamical properties are characterized by the relative position and velocity states as well as the angular velocity and Euler orientation angle states. Scheeres *et al.* [13] explains that using ground-based radar observations, Ostro *et al.* were able to create a model of the asteroid *Itokawa* and estimate its rotational states from Earth. Based on the polyhedral shape model, Scheeres *et al.* were able to determine estimates of the asteroid's physical properties such as its dimensions, volume, center-of-mass location, and moments of inertia as a function of the unknown mass [13]. By using these estimates as *a priori* knowledge, a spacecraft could perform observations post-rendezvous, re-estimate the dynamical states of the RSO at a significantly closer range (improving observational accuracy), and update the pre-programmed earth-based data set resulting in a high-fidelity model and accurate state estimates. Physical properties such as mass, moments of inertia, geometry could be validated and well characterized to relatively high accuracy. With an updated high-fidelity model of the RSO, and with new rotational state information, understanding the dynamical properties of the RSO (e.g. axis of rotation and spin stability) is greatly enhanced.

1.4 Literature Review

This thesis primarily involves spacecraft dynamics and estimation theory. Literature is abundant for both relative motion dynamics and rotational kinematics for a rigid-body. Texts by W. Wiesel [9] and B. Wie [14] cover both relative motion and rigid-body dynamics quite well. For this research, those references are the primary

source for the dynamics theory developed in Chapter 2. Another text written by W. Wiesel [15] provides a very complete foundation and guide for the implementation of least squares estimation theory for orbit determination, which is heavily used in this research. In addition, numerous journals authored by D. Scheeres [13, 1] provides insight into applications of estimation techniques using LIDAR and photogrammetry, proximity missions, and methods in characterizing physical and dynamical properties of an asteroid. Finally, theses authored by T. Storch, J. Heslin, and V. Chioma utilized least squares estimation methods for various orbit estimation applications. However, methods in directly estimating the moments of inertia of a rigid body based solely on range observations of the rotating body was not found in this literature review.

1.5 Research Objective

This thesis will explore the ability of a nonlinear least squares algorithm to estimate the relative motion, rotational states, and moments of inertia of a RSO by processing range data collected from tracked observational points on the RSO body from a simulated proximity mission.

II. Theoretical Basis

2.1 Background

This chapter will discuss the theory that is the foundation of the methodology used in this thesis. The theoretical basis of this research involves relative motion and rotational dynamics, linearization of nonlinear dynamical systems, and estimation theory; specifically, the nonlinear least squares method.

2.2 Dynamics

This section defines the reference frames used and develops the equations of motion necessary to describe relative motion and rotational kinematics following derivations provided by Wiesel [9], Wie [14], Meirovitch [16], and Curtis [17]. This section results in the formation of the dynamics state matrix for the Target body as seen by the Observer spacecraft.

2.2.1 Reference Frames. The coordinate frames used in this research are all Cartesian dextral frames. Along with each frame is a set of basis vectors and their associated scaler coordinates.

2.2.1.1 Earth-Centered Inertial. The Earth-Centered Inertial (ECI) reference frame is denoted as $\mathfrak{F}_i$ with the origin at the center of mass (CM) of the Earth. The $\mathfrak{F}_i$ frame has basis vectors of $\{\hat{\mathbf{I}}, \hat{\mathbf{J}}, \hat{\mathbf{K}}\}$ where, the $\hat{\mathbf{I}}$ unit vector points in the direction of the vernal equinox, traditionally denoted by γ. The $\hat{\mathbf{K}}$-axis is defined as the axis aligned with the spin-axis of the Earth and points out of the geographic north pole. The $\hat{\mathbf{J}}$-axis completes this orthogonal frame shown below in Figure 2.1.

The scalar coordinates associated with the basis vectors of this frame are (X, Y, Z). The $\mathfrak{F}_i$ frame is considered inertial and is therefore, *fixed* in space and does not rotate with the Earth.

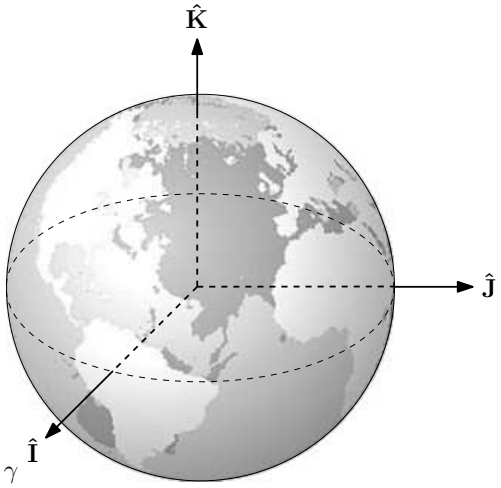

Figure 2.1 Earth-Centered Inertial Frame, $\mathfrak{F}_i$

2.2.1.2 Orbital Frame. The orbital reference frame, denoted as $\mathfrak{F}_e$, is also referred to as the Euler-Hill frame in most relative motion literature. The rotating orbital frame has basis vectors of $\{\hat{\mathbf{e}}_R, \hat{\mathbf{e}}_\theta, \hat{\mathbf{e}}_N\}$ where the origin of $\mathfrak{F}_e$ lies on a circular orbit defined by the vector, $\mathbf{R}_{tgt}$, measured from the $\mathfrak{F}_i$ origin at the center-of-mass of the Earth. The orbital frame rotates about the $\hat{\mathbf{e}}_N$-axis with the mean orbital motion, n, defined later in this chapter. The $\hat{\mathbf{e}}_\theta$-axis, referred to as the in-track direction, points along the velocity vector of the motion and is tangent to the circular orbit during the entire orbital period. The $\hat{\mathbf{e}}_N$-axis is perpendicular with the orbital plane and is termed the cross-track direction. The $\hat{\mathbf{e}}_R$-axis points radially outward, in the radial-track direction, the same direction as $\mathbf{R}_{tgt}$ and completes the dextral reference frame shown in Figure 2.2.

The center of mass of the Target body is centered with the origin of $\mathfrak{F}_e$. Therefore, the vector $\mathbf{R}_{tgt}$ points from the origin of $\mathfrak{F}_i$ to the origin of $\mathfrak{F}_e$–where the CM of the Target is located. It is important to note that the Target body has freedom of rotation, with the constraint, that the CM of the Target remains fixed on the $\mathfrak{F}_e$ origin. The scalar coordinates associated with the basis vectors of $\mathfrak{F}_e$ are $(\delta x, \delta y, \delta z)$. Note that δx and δy do not necessarily have to represent rectilinear coordinates. They can be interpreted as cylindrical curvilinear coordinates where δx represents

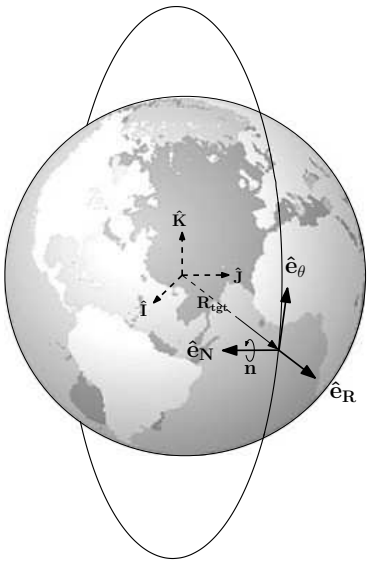

Figure 2.2 Orbital Frame of Target, $\mathfrak{F}_e$

a radial displacement, δr, and δy represents the curved flight-path displacement, $r_{obs}\delta\theta$, without change to the mathematical expressions [18, 9]. Using a curvilinear coordinate system does not restrict the magnitude of the $\hat{\mathbf{e}}_\theta$ displacement; and therefore, extends the validity of the relative motion solution [9, 14]. However, in this research the Target-Observer distances are so small that differences between the two frames are considered negligible; therefore, no distinction will be made between the linear and curvilinear frames.

2.2.1.3 Body Frame. The body reference frame of the Target, denoted as $\mathfrak{F}_b$, is non-inertial and fixed to the body of the Target. The origin of $\mathfrak{F}_b$ is placed at the center-of-mass of the Target. The $\mathfrak{F}_b$ frame has basis vectors of $\{\hat{\mathbf{b}}_1, \hat{\mathbf{b}}_2, \hat{\mathbf{b}}_3\}$ which are aligned with the principal axes of inertia of the Target body. Figure 2.3 illustrates a generic RSO and its body frame. The associated scalar coordinates are (b_1, b_2, b_3).

2.2.2 Relative Motion Dynamics. Originally introduced by Hill in 1878, W. H. Clohessy and R. S. Wiltshire developed a linearized set of equations of relative

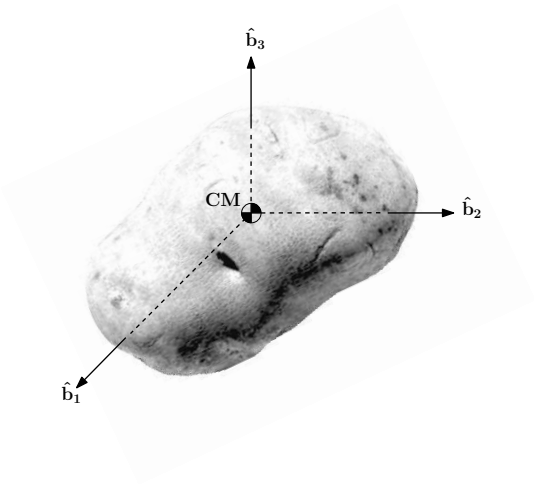

Figure 2.3 Body Frame of Target, $\mathfrak{F}_b$

motion in 1960 [19]. Termed the Clohessy-Wiltshire (CW) equations, also known as Hill's equations, they describe the relative motion of two satellites in close proximity while one satellite is in a circular orbit around a central body. The classic CW equations that are derived in this section assume the Target body follows a circular reference orbit around the Earth and neglects any disturbance forces. It should be mentioned, that the CW equations have been modified by others for application in eccentric reference orbits and to also include perturbations.

2.2.2.1 Hill-Clohessy-Wiltshire Equations. The governing equation of motion for the classic two-body problem of a satellite and central body is

$$\ddot{\mathbf{r}} = -\frac{\mu \mathbf{r}}{r^3} \tag{2.1}$$

where $\ddot{\mathbf{r}}$ is the acceleration of the body and $\mathbf{r}$ is the position vector of the body. Applying two-body motion to the Target in circular orbit around the Earth results in Equation 2.1 re-written as

$$\ddot{\mathbf{R}}_{tgt} = -\frac{\mu_\oplus \mathbf{R}_{tgt}}{R_{tgt}^3} \tag{2.2}$$

where $\mu_\oplus$ is the gravitational parameter of the Earth.

The position vector of the Target $\mathbf{R}_{tgt}$ from the origin of $\mathfrak{F}_i$ is defined as

$$\mathbf{R}_{tgt} = R_{tgt}\hat{\mathbf{e}}_R \tag{2.3}$$

and in conducting a space proximity operation, consider the Observer spacecraft operating in close vicinity to the Target. Keep in mind that the center of mass of the Target is fixed to the origin of the rotating orbital frame, $\mathfrak{F}_e$. The relative position vector of the Observer from the Target, $\delta\boldsymbol{\rho}$, is defined by the equation below

$$\delta\boldsymbol{\rho} = \delta x\hat{\mathbf{e}}_R + \delta y\hat{\mathbf{e}}_\theta + \delta z\hat{\mathbf{e}}_N \tag{2.4}$$

A major assumption is that the magnitude of $\delta\boldsymbol{\rho}$ is relatively small compared to the magnitude of $\mathbf{R}_{tgt}$. That is

$$\frac{\|\delta\boldsymbol{\rho}\|}{\|\mathbf{R}_{tgt}\|} \ll 1 \tag{2.5}$$

With that assumption in mind, the Observer follows two-body motion as well

$$\ddot{\mathbf{r}}_{obs} = -\frac{\mu_\oplus \mathbf{r}_{obs}}{r_{obs}^3} \tag{2.6}$$

where the position vector from the origin of $\mathfrak{F}_i$ to the Observer spacecraft is $\mathbf{r}_{obs}$. The vector relation between the Observer and Target is then given by the relation below and shown by the exaggerated illustration in Figure 2.4.

$$\mathbf{r}_{obs} = \mathbf{R}_{tgt} + \delta\boldsymbol{\rho} \tag{2.7}$$

Substituting Equations 2.3 and 2.4 in Equation 2.7 results in

$$\mathbf{r}_{obs} = (R_{tgt} + \delta x)\hat{\mathbf{e}}_R + \delta y\hat{\mathbf{e}}_\theta + \delta z\hat{\mathbf{e}}_N \tag{2.8}$$

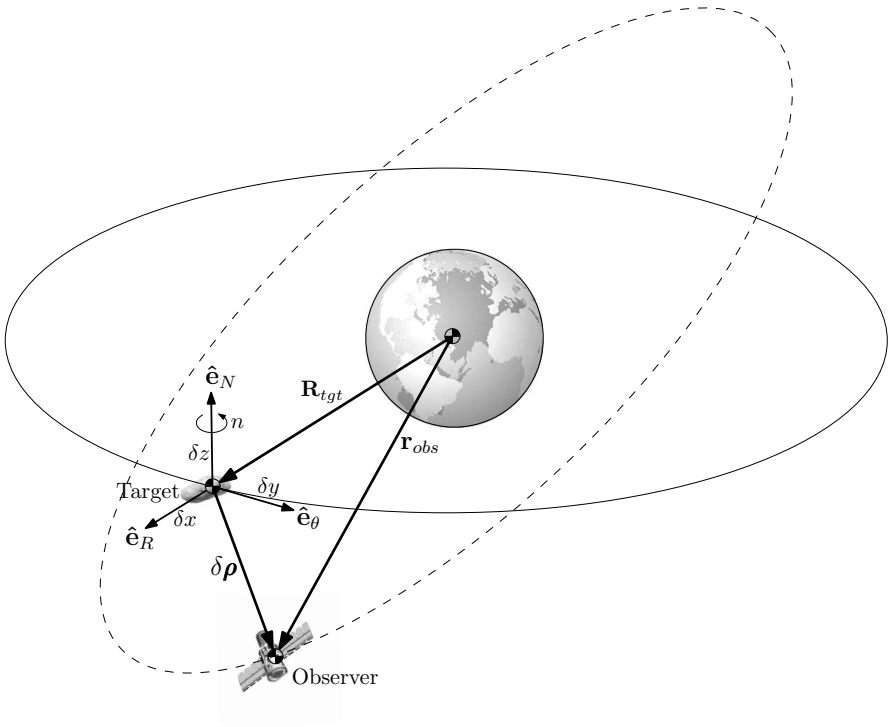

Figure 2.4 Relative Motion System

The following acceleration formula [9, 17] along with the circular orbit assumption

$$\ddot{\mathbf{r}}^i = \dot{\boldsymbol{\omega}}^{ei} \times \mathbf{r}^e + \boldsymbol{\omega}^{ei} \times (\boldsymbol{\omega}^{ei} \times \mathbf{r}^e) + 2\boldsymbol{\omega}^{ei} \times \dot{\mathbf{r}}^e + \ddot{\mathbf{r}}^e \tag{2.9}$$

is used where the superscripts i and e indicate the reference frames $\mathfrak{F}_i$ and $\mathfrak{F}_e$, respectively. The inertial acceleration of the Observer spacecraft is found by taking the first and second derivatives of Equation 2.8 with respect to time and making the proper substitutions into Equation 2.9 resulting in

$$\ddot{\mathbf{r}}_{obs} = [\delta\ddot{x} - 2\omega\delta\dot{y} - \omega^2(R_{tgt} + \delta x)]\hat{\mathbf{e}}_R + (\delta\ddot{y} + 2\omega\delta\dot{x} - \omega^2\delta y)\hat{\mathbf{e}}_\theta + \delta\ddot{z}\hat{\mathbf{e}}_N \tag{2.10}$$

where ω is the angular velocity between the frames $\mathfrak{F}_e$ and $\mathfrak{F}_i$. With the assumption that the Target body follows a circular orbit, the orbital frame rotation is equal to

the mean orbital motion of the Target

$$\boldsymbol{\omega}^{ei} = \omega\hat{\mathbf{e}}_N = n\hat{\mathbf{e}}_N \quad \text{or simply} \quad \omega = n \tag{2.11}$$

where the mean orbital motion of the Target, n, is defined as

$$n = \sqrt{\frac{\mu_\oplus}{R_{tgt}^3}} \tag{2.12}$$

Substituting Equation 2.8 into Equation 2.6, now results in

$$\ddot{\mathbf{r}}_{obs} = -\frac{\mu_\oplus[(R_{tgt}+\delta x)\hat{\mathbf{e}}_R + \delta y\hat{\mathbf{e}}_\theta + \delta z\hat{\mathbf{e}}_N]}{[(R_{tgt}+\delta x)^2 + \delta y^2 + \delta z^2]^{\frac{3}{2}}} \tag{2.13}$$

Using the binomial theorem in the form of

$$(1+b)^n = 1 + nb + \frac{n(n-1)}{2!}b^2 + ... \tag{2.14}$$

the denominator of Equation 2.13 is expanded as

$$\begin{aligned} r_{obs}^{-3} &= [(R_{tgt}^2 + 2R_{tgt}\delta x + \delta x^2 + \delta y^2 + \delta z^2]^{-\frac{3}{2}} && (2.15)\\ &= \left[R_{tgt}^2\left(1 + \frac{2}{R_{tgt}}\delta x + \frac{\delta x^2}{R_{tgt}^2} + \frac{\delta y^2}{R_{tgt}^2} + \frac{\delta z^2}{R_{tgt}^2}\right)\right]^{-\frac{3}{2}} && (2.16)\\ &= R_{tgt}^{-3}\left[1 - \frac{3}{2}\left(\frac{2\delta x}{R_{tgt}} + \frac{\delta x^2}{R_{tgt}^2} + \frac{\delta y^2}{R_{tgt}^2} + \frac{\delta z^2}{R_{tgt}^2} + ...\right)\right] && (2.17) \end{aligned}$$

Replace the denominator of Equation 2.13 with the binomial expansion and neglect terms higher than first-order. This results in

$$\ddot{\mathbf{r}}_{obs} \approx -\frac{\mu_\oplus}{R_{tgt}^3}[(R_{tgt} - 2\delta x)\hat{\mathbf{e}}_R + \delta y\hat{\mathbf{e}}_\theta + \delta z\hat{\mathbf{e}}_N] \tag{2.18}$$

Equate Equation 2.10 with Equation 2.18, substitute Equations 2.11 and 2.12, resulting in the system of equations

$$\begin{bmatrix} \delta\ddot{x} - 2\omega\delta\dot{y} - \omega^2(R_{tgt} + \delta x) \\ \delta\ddot{y} + 2\omega\delta\dot{x} - \omega^2\delta y \\ \delta\ddot{z} \end{bmatrix} + n^2 \begin{bmatrix} R_{tgt} - 2\delta x \\ \delta y \\ \delta z \end{bmatrix} = \begin{bmatrix} 0 \\ 0 \\ 0 \end{bmatrix} \tag{2.19}$$

Solve each equation (i.e. row) of Equation 2.19 for $\delta\ddot{x}$, $\delta\ddot{y}$, and $\delta\ddot{z}$, respectively. Finally, the system of CW equations [9] describing the relative motion of the Observer spacecraft with respect to the Target is given by

$$\delta\ddot{x} = 3n^2\delta x + 2n\delta\dot{y} \tag{2.20}$$

$$\delta\ddot{y} = -2n\delta\dot{x} \tag{2.21}$$

$$\delta\ddot{z} = -n^2\delta z \tag{2.22}$$

2.2.2.2 Hill-Clohessy-Wiltshire Solution. The closed-form solution to the CW Equations [9, 17] is given below

$$\delta x(t) = (4 - 3\cos nt)\delta x_0 + \frac{\sin nt}{n}\delta\dot{x}_0 + \frac{2}{n}(1 - \cos nt)\delta\dot{y}_0 \tag{2.23}$$

$$\delta y(t) = 6(\sin nt - nt)\delta x_0 + \delta y_0 - \frac{2}{n}(1 - \cos nt)\delta\dot{x}_0 + \frac{4\sin nt - 3nt}{n}\delta\dot{y}_0 \tag{2.24}$$

$$\delta z(t) = \delta z_0 \cos nt + \frac{\delta\dot{z}_0}{n}\sin nt \tag{2.25}$$

Recall that the relative position vector of the Observer spaceraft with respect to the Target in the $\mathfrak{F}_e$ frame is $\delta\boldsymbol{\rho}$ (Equ. 2.4). Therefore, the relative velocity vector, $\delta\dot{\boldsymbol{\rho}}$, is computed by taking the first time-derivative of the position vector; defined as

$$\delta\boldsymbol{\rho} = \begin{Bmatrix} \delta x \\ \delta y \\ \delta z \end{Bmatrix} \quad \text{and} \quad \delta\dot{\boldsymbol{\rho}} = \begin{Bmatrix} \delta\dot{x} \\ \delta\dot{y} \\ \delta\dot{z} \end{Bmatrix} \tag{2.26}$$

Therefore, the analytical solution for the relative velocity components are found by taking the time-derivative of Equations 2.23, 2.24, and 2.25, resulting in the following three expressions:

$$\delta\dot{x}(t) = \delta\dot{x}_0 \cos nt + (3n\delta x_0 + 2\delta\dot{y}_0) \sin nt \tag{2.27}$$

$$\delta\dot{y}(t) = (6n\delta x_0 + 4\delta\dot{y}_0) \cos nt - 2\delta\dot{x}_0 \sin nt - 6n\delta x_0 - 3\delta\dot{y}_0 \tag{2.28}$$

$$\delta\dot{z}(t) = -\delta z_0 n \sin nt + \delta\dot{z}_0 \cos nt \tag{2.29}$$

The CW state vector explicitly written as a function of time is then defined as

$$\mathbf{X}_{cw}(t) = \begin{Bmatrix} \delta\boldsymbol{\rho}(t) \\ \delta\dot{\boldsymbol{\rho}}(t) \end{Bmatrix} = \begin{Bmatrix} \delta x(t) \\ \delta y(t) \\ \delta z(t) \\ \delta\dot{x}(t) \\ \delta\dot{y}(t) \\ \delta\dot{z}(t) \end{Bmatrix} \tag{2.30}$$

Let $\mathbf{X}_{cw}(t_0)$ represent the initial CW state at an initial epoch time, t_0. Then let $\mathbf{X}_{cw}(t)$ represent the propagated CW states at some future time, t. Using both the closed-form CW solution for the relative position and velocity, define the CW state transition matrix, $\boldsymbol{\Phi}(t, t_0)$, as the matrix to propagate from $\mathbf{X}_{cw}(t_0)$ to $\mathbf{X}_{cw}(t)$, as

$$\boldsymbol{\Phi}_{cw}(t, t_0) = \begin{bmatrix} 4 - 3\cos nt & 0 & 0 & \frac{1}{n}\sin nt & \frac{2}{n}(1 - \cos nt)0 & \\ 6(\sin nt - nt) & 1 & 0 & -\frac{2}{n}(1 - \cos nt) & \frac{1}{n}(4\sin nt - 3nt) & 0 \\ 0 & 0 & \cos nt & 0 & 0 & \frac{1}{n}\sin nt \\ 3n\sin nt & 0 & 0 & \cos nt & 2\sin nt & 0 \\ -6n(1 - \cos nt) & 0 & 0 & -2\sin nt & 4\cos nt - 3 & 0 \\ 0 & 0 & -n\sin nt & 0 & 0 & \cos nt \end{bmatrix} \tag{2.31}$$

Finally, the complete solution of the relative motion system in the $\mathfrak{F}_e$ frame is compactly defined as

$$\mathbf{X}_{cw}(t) = \mathbf{\Phi}_{cw}(t, t_0)\mathbf{X}_{cw}(t_0) \tag{2.32}$$

2.2.3 Rotational Dynamics. The rotational equations of motion of a rigid body are given by *two* systems of equations. The first system is a set of three differential equations known as Euler's Equations. The second set consists of three differential equations describing the orientation of the body in terms of the classic Euler angles. It should be mentioned that a singularity does exist when using Euler angles (which will be discussed later in this chapter). One could also obtain the second set of equations of motion using quaternions to describe the rigid body's orientation (without singularities). However, for the scope of this research it is assumed that no operation is taking place at the singularity. It is also assumed that the Target body is a rigid body.

2.2.3.1 Euler's Rotational Equations of Motion. Euler's Equations, as derived in [9] and [14] begins with the relation that the applied torque must equal the inertial time-rate-of-change of the angular momentum of a rigid body (i.e the Target body)

$$\mathbf{M} = \dot{\mathbf{H}} \tag{2.33}$$

where $\mathbf{M}$ is the external moment acting about the CM of the Target body and $\mathbf{H}$ is the angular momentum also about the CM of the Target.

The angular momentum of the Target, in the body frame, is expressed as

$$\mathbf{H} = I\boldsymbol{\omega}^{bi} \tag{2.34}$$

Since this is a rigid body, the moment of inertia matrix, $\mathbf{I}$, is constant in $\mathfrak{F}_b$. Then using what is sometimes referred to as the transport theorem, the time derivative of

the angular momentum in the inertial frame is given by

$$\dot{\mathbf{H}} \equiv \left\{ \frac{d\mathbf{H}}{dt} \right\}^{i} = \left\{ \frac{d\mathbf{H}}{dt} \right\}^{b} + \boldsymbol{\omega}^{bi} \times \mathbf{H} \tag{2.35}$$

where the b and i superscripts refer to the $\mathfrak{F}_b$ and $\mathfrak{F}_i$, respectively, where the time-derivative or quantity is in reference to. The angular velocity, $\boldsymbol{\omega}^{bi}$, is simply the angular velocity of $\mathfrak{F}_b$ with respect to the $\mathfrak{F}_i$ and it is also the same quantity used in Equation 2.34. Substituting Equation 2.34 into Equation 2.35 and recalling that the moment-of-inertia matrix of the body is constant in $\mathfrak{F}_b$ yields Euler's rotational equation of motion in vector form

$$\mathbf{M} = I\dot{\boldsymbol{\omega}}^{bi} + \boldsymbol{\omega}^{bi} \times I\boldsymbol{\omega}^{bi} \tag{2.36}$$

The term $\dot{\boldsymbol{\omega}}^{bi}$ is time-derivative of the angular velocity in the body frame.

Since the $\mathfrak{F}_b$ frame is defined as the principle-axis reference frame of the Target, the moment-of-inertia matrix of the Target body is given by

$$\mathbf{I} = \begin{bmatrix} A & 0 & 0 \\ 0 & B & 0 \\ 0 & 0 & C \end{bmatrix} \tag{2.37}$$

in the $\mathfrak{F}_b$ frame. The angular velocity vector, $\boldsymbol{\omega}^{bi}$ is defined by

$$\boldsymbol{\omega}^{bi} = \omega_1 \mathbf{b}_1 + \omega_2 \mathbf{b}_2 + \omega_3 \mathbf{b}_3 \tag{2.38}$$

In this research, no external torques are applied to the Target. Therefore,

$$\mathbf{M} = 0\mathbf{b}_1 + 0\mathbf{b}_2 + 0\mathbf{b}_3 \tag{2.39}$$

Substituting Equations 2.37 through 2.39 into Equation 2.36 in component form yields Euler's Equations, as derived in [9], [14], and [16], shown below

$$0 = A\dot{\omega}_1 + (C - B)\omega_2\omega_3 \tag{2.40}$$

$$0 = B\dot{\omega}_2 + (A - C)\omega_3\omega_1 \tag{2.41}$$

$$0 = C\dot{\omega}_3 + (B - A)\omega_1\omega_2 \tag{2.42}$$

Solving for the angular accelerations results in the following coupled, nonlinear, first order differential equations of motion

$$\dot{\omega}_1 = \frac{(B - C)}{A}\omega_2\omega_3 \tag{2.43}$$

$$\dot{\omega}_2 = \frac{(C - A)}{B}\omega_1\omega_3 \tag{2.44}$$

$$\dot{\omega}_3 = \frac{(A - B)}{C}\omega_1\omega_2 \tag{2.45}$$

2.2.3.2 Rotational Kinematics. Completing the set of equations of motion for a rigid body are the kinematic differential equations describing the orientation of the Target. A 3-2-1 Euler angle sequence (i.e. roll-pitch-yaw) is used and derived following Wiesel [9], Wie [14], and Meirovitch [16].

The 3-2-1 Euler sequence describes the rotation sequence of a body frame initially coincident with an inertial reference frame rotated to a final orientation described by the angles, θ_1, θ_2, θ_3. In the case of this research, the rotating $\mathfrak{F}_e$ frame is considered quasi-inertial with respect to the $\mathfrak{F}_b$ frame for short and finite periods of time during the proximity operation and acts effectively as a reference frame for the orientation of the Target body frame.

Beginning with the standard sequence to rotate from the orbital reference frame to the body frame, the matrix $[\mathbf{R}]$ is a rotation matrix of sines and cosines. The subscript of $[\mathbf{R}]$ indicates the axis in which a rotation of the specified angle will

occur. The basis vectors $\{\xi, \eta, \zeta\}$ and $\{\xi', \eta', \zeta'\}$ describe the intermediate frames during the rotation sequence.

1. $[\mathbf{R}_3(\theta_3)] : \{\hat{\mathbf{e}}_R, \hat{\mathbf{e}}_\theta, \hat{\mathbf{e}}_N\} \rightarrow \{\xi', \eta', \zeta'\}$
2. $[\mathbf{R}_2(\theta_2)] : \{\xi', \eta', \zeta'\} \rightarrow \{\xi, \eta, \zeta\}$
3. $[\mathbf{R}_1(\theta_1)] : \{\xi, \eta, \zeta\} \rightarrow \{\hat{\mathbf{b}}_1, \hat{\mathbf{b}}_2, \hat{\mathbf{b}}_3\}$

Mathematically, this transition between frames occurs as such

$$\begin{Bmatrix} \xi' \\ \eta' \\ \zeta' \end{Bmatrix} = [\mathbf{R}_3(\theta_3)] \begin{Bmatrix} \hat{\mathbf{e}}_R \\ \hat{\mathbf{e}}_\theta \\ \hat{\mathbf{e}}_N \end{Bmatrix} \tag{2.46a}$$

$$\begin{Bmatrix} \xi \\ \eta \\ \zeta \end{Bmatrix} = [\mathbf{R}_2(\theta_2)] \begin{Bmatrix} \xi' \\ \eta' \\ \zeta' \end{Bmatrix} \tag{2.46b}$$

$$\begin{Bmatrix} \hat{\mathbf{b}}_1 \\ \hat{\mathbf{b}}_2 \\ \hat{\mathbf{b}}_3 \end{Bmatrix} = [\mathbf{R}_1(\theta_1)] \begin{Bmatrix} \xi \\ \eta \\ \zeta \end{Bmatrix} \tag{2.46c}$$

where the elementary matrices are defined as

$$[\mathbf{R}_3(\theta_3)] = \begin{bmatrix} \cos\theta_3 & \sin\theta_3 & 0 \\ -\sin\theta_3 & \cos\theta_3 & 0 \\ 0 & 0 & 1 \end{bmatrix} \tag{2.47a}$$

$$[\mathbf{R}_2(\theta_2)] = \begin{bmatrix} \cos\theta_2 & 0 & -\sin\theta_2 \\ 0 & 1 & 0 \\ \sin\theta_2 & 0 & \cos\theta_2 \end{bmatrix} \tag{2.47b}$$

$$[\mathbf{R}_1(\theta_1)] = \begin{bmatrix} 1 & 0 & 0 \\ 0 & \cos\theta_1 & \sin\theta_1 \\ 0 & -\sin\theta_1 & \cos\theta_1 \end{bmatrix} \tag{2.47c}$$

Equating the intermediate transformation equations, Equations 2.46a-c, yields the relation

$$\begin{Bmatrix} \hat{\mathbf{b}}_1 \\ \hat{\mathbf{b}}_2 \\ \hat{\mathbf{b}}_3 \end{Bmatrix} = [\mathbf{R}_1(\theta_1)]\,[\mathbf{R}_2(\theta_2)]\,[\mathbf{R}_3(\theta_3)] \begin{Bmatrix} \hat{\mathbf{e}}_R \\ \hat{\mathbf{e}}_\theta \\ \hat{\mathbf{e}}_N \end{Bmatrix} \tag{2.48}$$

By performing matrix multiplication in the proper sequence for each elementary rotation matrix yields a single rotation matrix denoted as $\left[\mathbf{R}^{be}\right]$

$$\left[\mathbf{R}^{be}\right] = [\mathbf{R}_1(\theta_1)]\,[\mathbf{R}_2(\theta_2)]\,[\mathbf{R}_3(\theta_3)] \tag{2.49}$$

$$\left[\mathbf{R}^{be}\right] = \begin{bmatrix} \mathrm{c}\theta_2\mathrm{c}\theta_3 & \mathrm{c}\theta_2\mathrm{s}\theta_3 & -\mathrm{s}\theta_2 \\ \mathrm{s}\theta_1\mathrm{s}\theta_2\mathrm{c}\theta_3 - \mathrm{c}\theta_1\mathrm{s}\theta_3 & \mathrm{s}\theta_1\mathrm{s}\theta_2\mathrm{s}\theta_3 + \mathrm{c}\theta_1\mathrm{c}\theta_3 & \mathrm{s}\theta_1\mathrm{c}\theta_2 \\ \mathrm{c}\theta_1\mathrm{s}\theta_2\mathrm{c}\theta_3 + \mathrm{s}\theta_1\mathrm{s}\theta_3 & \mathrm{c}\theta_1\mathrm{s}\theta_2\mathrm{s}\theta_3 - \mathrm{s}\theta_1\mathrm{c}\theta_3 & \mathrm{c}\theta_1\mathrm{c}\theta_2 \end{bmatrix} \tag{2.50}$$

where the abbreviations $\mathrm{s}\theta = \sin(\theta)$, and $\mathrm{c}\theta = \cos(\theta)$ are used. The superscript above the rotation matrix be denotes transformation from $\mathfrak{F}_e \rightarrow \mathfrak{F}_b$. Therefore, a vector described in the orbital frame, denoted as $\{\mathfrak{F}_e\}$, can be transformed into a vector written in body frame components, $\{\mathfrak{F}_b\}$, by pre-multiplying $\{\mathfrak{F}_e\}$ with $\left[\mathbf{R}^{be}\right]$ as shown

$$\{\mathfrak{F}_b\} = \left[\mathbf{R}^{be}\right]\{\mathfrak{F}_e\} \tag{2.51}$$

The rotation matrix, $\left[\mathbf{R}^{be}\right]$, is an orthonormal matrix; hence, it can be shown that the inverse of the rotation matrix is simply its transpose. Therefore, the rotation matrix, $\left[\mathbf{R}^{eb}\right]$, for the inverse transformation, $\mathfrak{F}_b \rightarrow \mathfrak{F}_e$, is simply

$$\left[\mathbf{R}^{eb}\right] = \left[\mathbf{R}^{be}\right]^T \tag{2.52}$$

Since the focus of the this paper is based on the relative motion of the Target and the Observer with respect to $\mathfrak{F}_e$, it will be necessary to describe the orientation

of the Target body with respect to the orbital frame as well. Therefore, a vector written in the body frame, $\{\mathfrak{F}_b\}$, is transformed into a vector written in orbital frame components, $\{\mathfrak{F}_e\}$, using the rotation matrix, $\left[\mathbf{R}^{eb}\right]$, as shown

$$\{\mathfrak{F}_e\} = \left[\mathbf{R}^{eb}\right] \{\mathfrak{F}_b\} \tag{2.53}$$

where

$$\left[\mathbf{R}^{eb}\right] = \begin{bmatrix} \mathrm{c}\theta_2\mathrm{c}\theta_3 & \mathrm{s}\theta_1\mathrm{s}\theta_2\mathrm{c}\theta_3 - \mathrm{c}\theta_1\mathrm{s}\theta_3 & \mathrm{c}\theta_1\mathrm{s}\theta_2\mathrm{c}\theta_3 + \mathrm{s}\theta_1\mathrm{s}\theta_3 \\ \mathrm{c}\theta_2\mathrm{s}\theta_3 & \mathrm{s}\theta_1\mathrm{s}\theta_2\mathrm{s}\theta_3 + \mathrm{c}\theta_1\mathrm{c}\theta_3 & \mathrm{c}\theta_1\mathrm{s}\theta_2\mathrm{s}\theta_3 - \mathrm{s}\theta_1\mathrm{c}\theta_3 \\ -\mathrm{s}\theta_2 & \mathrm{s}\theta_1\mathrm{c}\theta_2 & \mathrm{c}\theta_1\mathrm{c}\theta_2 \end{bmatrix} \tag{2.54}$$

To obtain the kinematic equations of motion, the time-dependence of the Euler angles will be formed. The time derivatives of the 3-2-1 Euler angles, termed Euler rates, are denoted as $\dot{\theta}_1$, $\dot{\theta}_2$, and $\dot{\theta}_3$.

The angular velocity solution of the body is provided by numerical integration of Euler's Equations 2.43, 2.44, and 2.45. The angular velocity vector is equal to the angular velocity of the body frame with respect to the inertial frame as shown earlier in Equation 2.38.

$$\boldsymbol{\omega} \equiv \boldsymbol{\omega}^{be} \tag{2.55}$$

Therefore, with the rotational sequence in mind, one can write the equivalent statement with mixed basis vectors

$$\boldsymbol{\omega} = \dot{\theta}_1 \hat{\mathbf{b}}_1 + \dot{\theta}_2 \boldsymbol{\eta} + \dot{\theta}_3 \boldsymbol{\zeta}' \tag{2.56}$$

This relation describes the angular rate of rotation for each axis during the coordinate frame rotation sequence. Using Equation 2.56 and Equations 2.47a-c results in the

angular velocity expressed solely in the body frame

$$\begin{Bmatrix} \omega_1 \\ \omega_2 \\ \omega_3 \end{Bmatrix} = \begin{Bmatrix} \dot{\theta}_1 \\ 0 \\ 0 \end{Bmatrix} + [\mathbf{R}_1(\theta_1)] \begin{Bmatrix} 0 \\ \dot{\theta}_2 \\ 0 \end{Bmatrix} + [\mathbf{R}_1(\theta_1)]\,[\mathbf{R}_2(\theta_2)] \begin{Bmatrix} 0 \\ 0 \\ \dot{\theta}_3 \end{Bmatrix} \tag{2.57}$$

The result of the multiplication in matrix form is

$$\begin{Bmatrix} \omega_1 \\ \omega_2 \\ \omega_3 \end{Bmatrix} = \begin{bmatrix} 1 & 0 & -\sin\theta_2 \\ 0 & \cos\theta_1 & \sin\theta_1\cos\theta_2 \\ 0 & -\sin\theta_1 & \cos\theta_1\cos\theta_2 \end{bmatrix} \begin{Bmatrix} \dot{\theta}_1 \\ \dot{\theta}_2 \\ \dot{\theta}_3 \end{Bmatrix} \tag{2.58}$$

Finally, solving for the Euler rates yields the remaining system of kinematic differential equations [14] needed for describing the rotational motion of the Target body

$$\begin{Bmatrix} \dot{\theta}_1 \\ \dot{\theta}_2 \\ \dot{\theta}_3 \end{Bmatrix} = \frac{1}{\cos\theta_2} \begin{bmatrix} \cos\theta_2 & \sin\theta_1\sin\theta_2 & \cos\theta_1\sin\theta_2 \\ 0 & \cos\theta_1\cos\theta_2 & -\sin\theta_1\cos\theta_2 \\ 0 & \sin\theta_1 & \cos\theta_1 \end{bmatrix} \begin{Bmatrix} \omega_1 \\ \omega_2 \\ \omega_3 \end{Bmatrix} \tag{2.59}$$

and expressed in three scalar equations for consistency

$$\dot{\theta}_1 = \omega_1 + \omega_2 \sin\theta_1 \tan\theta_2 + \omega_3 \cos\theta_1 \tan\theta_2 \tag{2.60}$$

$$\dot{\theta}_2 = \omega_2 \cos\theta_1 - \omega_3 \sin\theta_1 \tag{2.61}$$

$$\dot{\theta}_3 = \omega_2 \sin\theta_1 \sec\theta_2 + \omega_3 \cos\theta_1 \sec\theta_2 \tag{2.62}$$

The solution to Euler's Equations 2.43, 2.44, and 2.45, provides the angular velocity vector as a function of time. Using that vector in Equation 2.59, and numerically integrating, will provide the orientation of the Target as a function of time.

The major drawback of using Euler angles to describe the orientation of a rigid body is the existence of a singularity. In this rotational scheme, the singularity occurs when $\theta_2 = \frac{\pi}{2}$. As mentioned in the beginning of this section, for the purpose of this research, Euler angles are sufficient to describe the orientation of the Target. It will assumed that the Target body does not operate in this singularity region during the relatively short duration of the proximity operation studied.

2.2.4 Dynamics State Vector. The Target is characterized by its states, including both its relative motion (i.e. CW position and velocity) with the Observer as well as its rotational body dynamics (i.e. angular rotation and Euler orientation angles). Consolidating the state parameters that describe the dynamical uniqueness of the Target at any moment in time during the proximity operation leads to the formation of the complete dynamics state matrix.

Define $\mathbf{X}_{rot}(t)$ as the rotational dynamics portion of the state matrix

$$\mathbf{X}_{rot}(t) = \begin{Bmatrix} \omega_1(t) \\ \omega_2(t) \\ \omega_3(t) \\ \theta_1(t) \\ \theta_2(t) \\ \theta_3(t) \end{Bmatrix} \tag{2.63}$$

Using a Runge-Kutta numerical integration method, the numerical solution of Equations 2.43, 2.44, and 2.45 results in ω_1, ω_2, and ω_3 and the numerical solution of Equations 2.60, 2.61, and 2.62 results in θ_1, θ_2, and θ_3. These parameters of angular velocity and orientation angles form a state vector of the rotational states of the Target as a function of time.

Recall, Equation 2.30 defines the states for the dynamics of the relative motion between the Target and the Observer. Consolidating the CW and rotational state

vectors results in the complete state vector, $\mathbf{X}(t)$, describing the dynamics of the Target body with respect to time.

$$\mathbf{X}(t) \quad = \quad \begin{Bmatrix} \mathbf{X}_{cw}(t) \\ \mathbf{X}_{rot}(t) \end{Bmatrix} \tag{2.64}$$

In expanded form, the transpose of the complete *12-state vector* of the Target's dynamics is defined as

$$\mathbf{X} = \begin{bmatrix} \delta x & \delta y & \delta z & \delta \dot{x} & \delta \dot{y} & \delta \dot{z} & \omega_1 & \omega_2 & \omega_3 & \theta_1 & \theta_2 & \theta_3 \end{bmatrix}^T \tag{2.65}$$

Using the assumption that the moments of inertia of the Target are constant over time. The time-derivative of the Target MOI are given by the following equations

$$\dot{A} = 0 \tag{2.66}$$

$$\dot{B} = 0 \tag{2.67}$$

$$\dot{C} = 0 \tag{2.68}$$

where the MOI states are defined as

$$\mathbf{X}_{moi} \quad = \quad \begin{Bmatrix} A \\ B \\ C \end{Bmatrix} \tag{2.69}$$

By removing the CW states $\mathbf{X}_{cw}$ from Equation 2.64 and including $\mathbf{X}_{moi}(t)$, results in a separate *9-state vector* version defined as

$$\mathbf{X} = \begin{bmatrix} \omega_1 & \omega_2 & \omega_3 & \theta_1 & \theta_2 & \theta_3 & A & B & C \end{bmatrix}^T \tag{2.70}$$

2.3 Dynamics Linearization

Apparently, the world was not created using a linear dynamics model, which simply means most of the dynamical behavior that one would be interested in is simply nonlinear and/or unpredictable in nature. However by limiting our observation time and invoking small state changes, one can essentially linearize the nonlinear systems in regions that would provide approximate results. Using the derivations provided in two texts by Wiesel [15, 20], methods of linearization are formulated below.

2.3.1 Equations of Variation. The dynamical state of the Target-Observer system is described by the relative position, relative velocity, angular velocity components, and Euler orientation angles derived in the last section. These system state variables comprise the dynamics state vector, $\mathbf{X}$. Each system state variable has an associated equation of motion. Therefore, the change of the state vector with respect to time is dictated by the equations of motion

$$\dot{\mathbf{X}} = \mathbf{f}(\mathbf{X}, t) \tag{2.71}$$

To create a trajectory, initial state conditions, $\mathbf{X}_0(t_0)$, must be defined at some epoch time, t_0. Using numerical integration methods, the state vector can then be propagated to some future time resulting in a trajectory $\mathbf{X}_0(t)$. With a slight change in the state vector, $\delta\mathbf{X}$, one would expect a slight change in the trajectory. The resulting trajectory is then said to be close to the original trajectory. This fundamental expectation can be written, in general, as

$$\mathbf{X}(t) = \mathbf{X}_0(t) + \delta\mathbf{X}(t) \tag{2.72}$$

Substituting Equation 2.72 into Equation 2.71 yields

$$\dot{\mathbf{X}} = \dot{\mathbf{X}}_0 + \delta\dot{\mathbf{X}} = \mathbf{f}(\mathbf{X}_0 + \delta\mathbf{X}, t) \tag{2.73}$$

Applying a Taylor series expansion to the equations of motion

$$\sum_{n=0}^{\infty} \frac{f^{(n)}(\alpha)}{n!}(x-\alpha)^n = f^{(0)}(\alpha) + f^{(1)}(\alpha)(x-\alpha) + \frac{f^{(2)}(\alpha)}{2!}\ldots \tag{2.74}$$

about the point $\alpha = \mathbf{X}_0 + \delta\mathbf{X}$ where, $\delta\mathbf{X}$=0, and neglecting second-order terms and higher, results in

$$\dot{\mathbf{X}} \approx \mathbf{f}(\mathbf{X}_0 + 0) + \mathbf{f}^{(1)}(\mathbf{X}_0 + 0)(\mathbf{X}_0 + \delta\mathbf{X} - \mathbf{X}_0 - 0) + \mathcal{O}(2) \tag{2.75}$$

$$\dot{\mathbf{X}}_0 + \delta\dot{\mathbf{X}} \approx \mathbf{f}(\mathbf{X}_0) + \left.\frac{\partial \mathbf{f}}{\partial \mathbf{X}}\right|_{\mathbf{X}_0} \delta\mathbf{X} \tag{2.76}$$

After cancelling Equation 2.71 from both sides, results in the familiar equations of variation used for the linearization of the dynamics

$$\delta\dot{\mathbf{X}} = \left.\frac{\partial \mathbf{f}}{\partial \mathbf{X}}\right|_{\mathbf{X}_0} \delta\mathbf{X} = A(t)\delta\mathbf{X} \tag{2.77}$$

The equations of variation are time-varying linear ordinary differential equations. Matrix A is a square matrix with the dimensions of the number of states. It is formed by the partial derivatives of the equations of motion with respect to the state variables evaluated at some nominal trajectory.

2.3.2 State Transition Matrix. The solution to the Equations of Variation, Equation 2.77, is provided in detail by Wiesel [15]. They are found by summing the individual components of $\delta\mathbf{X}$ at an initial time multiplied by each solution vector,

that is

$$\delta\mathbf{X}(t) = \sum_{i=1}^{N} \delta X_i(t_0)\boldsymbol{\phi}_i(t) \tag{2.78}$$

Arranging the vector solutions, $\boldsymbol{\phi}_i$, into a square matrix format results in the formation of the *State Transition Matrix*, $\boldsymbol{\Phi}$

$$\delta\mathbf{X}(t) = \boldsymbol{\Phi}(t, t_0)\delta\mathbf{X}(t_0) \tag{2.79}$$

The matrix $\boldsymbol{\Phi}(t, t_0)$ propagates the state from time t_0 to time t. Another valid expression of the state transition matrix is the differential equation

$$\dot{\boldsymbol{\Phi}}(t, t_0) = A(t)\boldsymbol{\Phi}(t, t_0) \tag{2.80}$$

From Reference [15], an identity of the state transition matrix is

$$\boldsymbol{\Phi}(t_2, t_0) = \boldsymbol{\Phi}(t_2, t_1)\boldsymbol{\Phi}(t_1, t_0) \tag{2.81}$$

This identity is useful in de-bugging and validation of code for the estimator program that will be mentioned in the next chapter.

2.4 Estimation Theory

Thus far, the theory governing the *deterministic* dynamics of the Target-Observer system has been discussed. Following the detailed derivation provided by Wiesel [15], this section will briefly explore the theory behind the least squares estimation method of data reduction.

The method of least squares estimation is based primarily on the following assumptions:

- Gaussian distribution of error in the observational data

- Deterministic dynamics (i.e. no error in the dynamics model)
- Principle of Maximum Likelihood approach to probability

2.4.1 Probability Theory. French mathematician Abraham de Moivre (1667-1754) first introduced the mathematical equation of the normal distribution curve in 1733 [21]. The normal distribution is often referred to as the Gaussian distribution in honor of the German mathematician and astronomer Carl Friedrich Gauss (1777-1855). Gauss, considered a mathematical *Wunderkind* or child prodigy, is credited for the development of the theoretical basis of least squares in 1795 at the age of eighteen [22, 23]. Gauss introduced and applied his method of least squares in 1801 to accurately re-discover the asteroid Ceres (although the method was officially published by Adrien-Marie Legendre five years later) [22, 23]. Beginning with the Gaussian or normal statistical distribution model [21], explained below, the familiar probability density function is

$$\mathbf{P}(x;\mu,\sigma) = \frac{1}{\sigma\sqrt{2\pi}} exp\left(\frac{(x-\mu)^2}{2\sigma^2}\right) \tag{2.82}$$

Following the derivation provided by Wiesel [15], in least squares estimation theory, the observational data (i.e. the raw physical measurements) contain error, which has a Gaussian distribution expressed as

$$\mathbf{P}(e) = \frac{1}{\sigma\sqrt{2\pi}} exp\left(\frac{-e^2}{2\sigma^2}\right) \tag{2.83}$$

where $\mathbf{P}(e)$ is the probability of obtaining an error, e. Once a range of error is defined, the area under the Gaussian curve will give the probability of the error occurring within the range. Lets describe a measurement, x, as

$$x = x_0 + e + b \qquad \text{or} \qquad e = x - b - x_0 \tag{2.84}$$

where x_0 is the unknown true value, the true random error e in the measurement, and the bias b of the instrument. From another perspective, applying Equation 2.83 and the error function to observational data, the probability of data x lying within a defined interval can then be predicted. The distribution is normalized so that the sum over all values gives a probability of 1. The standard deviation, σ, defines the width of the Gaussian curve which is symmetric about its mean, μ, often defined as the true value and with a bias of zero (no shift). A large σ results in a broad Gaussian curve (i.e. low precision) and a small σ results in a narrow curve (i.e. high precision). Therefore, an instrument is considered precise when it has a relatively small standard deviation because the measurement data points have a smaller spread from the true value, μ. The Gaussian curve shown in Figure 2.5 illustrates that approximately 68% of the data sample (i.e. measurements x) will lie within the range of $\pm 1\sigma$ from the actual true value, $\mu = x_0$.

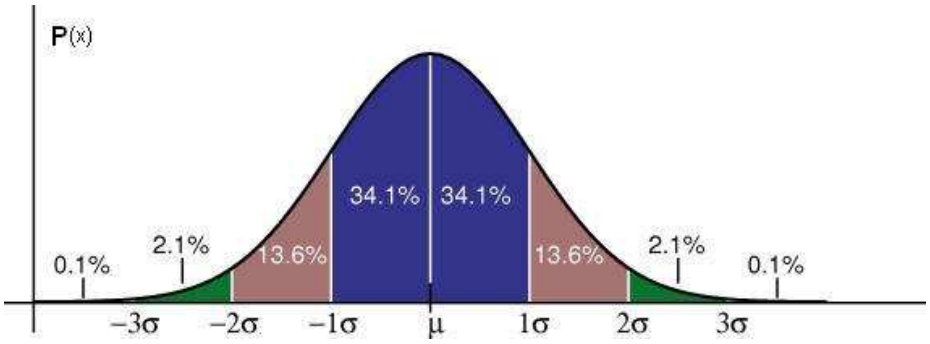

Figure 2.5 Gaussian Distribution, (courtesy of Beirne)

Before proceeding, the Central Limit Theorem should be mentioned. Wiesel [15] describes this theorem as "the keystone of estimation theory" because this theorem is what allowed Gauss to justify the assumption that the statistical behavior of error inherent in measurement data is Gaussian in nature. Although the lengthy proof is not shown here, it can be found in great detail in the text by Wiesel [15].

In the simplest case, multiple measurements are made in an attempt to accurately determine a single true value that one wishes to know exactly. Unfortunately,

the true value is never known exactly to infinite point precision; instead one must settle for an estimate of the true value. Given N independent measurements, x_i, of some exact quantity, x_0, the joint probability is given by the product of the individual Gaussian distributions

$$\mathbf{P}(x_1, x_2, ..., x_N) = (2\pi)^{-\frac{N}{2}} \left[\prod_{i=1}^{N} \sigma_i^{-1} \right] exp\left(-\sum_{i=1}^{N} \frac{(x_i - x_0)^2}{2\sigma_i^2} \right) \tag{2.85}$$

where the instrument standard deviation, σ, describing the measurement error is known. Keep in mind the accuracy of the measurement data described by its σ-value is actually a property of the instrument making the measurement. As mentioned earlier, since the true value that one attempts to know through multiple measurements is actually unattainable, and the true error of the measurement is also unknown, Equation 2.85 leads to an indeterminable condition. In order to make progress in quantifying an unknown quantity, an estimate $\bar{x}$ of the true quantity x_0 will be made. The pessimistic and ultra-conservative approach is to assume that the error in the measurement data is present in its most maximum form possible. This would lead to the estimate of $\bar{x} = \pm\infty$ which would lead nowhere in estimating the true value. Therefore, the optimistic approach or *Principle of Maximum Likelihood* is used. This principle defines the "...estimate $\bar{x}$ as the value of x_0 which maximizes the probability of having obtained the actual data set [15]." Equation 2.85 is used with the substitution of the estimate $\bar{x}$ for the true value x_0

$$\mathbf{P}(x_i) = (2\pi)^{-\frac{N}{2}} \left[\prod_{i=1}^{N} \sigma_i^{-1} \right] exp\left(-\sum_{i=1}^{N} \frac{(x_i - \bar{x})^2}{2\sigma_i^2} \right) \tag{2.86}$$

The next step, using the Principle of Maximum Likelihood, is to maximize the probability. By taking the derivative of the exponential quantity of Equation 2.86 with respect to the estimate $\bar{x}$ and setting it equal to zero minimizes the exponential

quantity which maximizes the probability resulting in *the Method of Least Squares*

$$\frac{d}{d\bar{x}} \sum_{i=1}^{N} \frac{(x_i - \bar{x})^2}{2\sigma_i^2} = 0 \tag{2.87}$$

The least squares method is commonly described as minimizing the sum of the square of the residuals. Taking the derivative yields

$$\sum_{i=1}^{N} \frac{(x_i - \bar{x})}{\sigma_i^2} = 0 \tag{2.88}$$

The key step in this entire formulation was replacing the unattainable true error of

$$e_i = x_i - x_0 \tag{2.89}$$

with the residual

$$r_i \equiv x_i - \bar{x} \tag{2.90}$$

where the *residual* is defined as the difference or essentially the error between the observed quantity and the calculated quantity. Therefore, the statistics of the residuals can give you insight on the estimate. If the estimate is nearly equal to the true value then the residual will be nearly equal to the true error [15].

2.4.2 Linear Least Squares. Following the text by Wiesel [15], the objective is to estimate the state of a linear dynamic system at epoch time t_0 from measurement data $\mathbf{z}_i$ taken at specific observation times t_i.

$$\mathbf{X}_i(t) = \mathbf{\Phi}(t_i, t_0)\mathbf{X}(t_0) \tag{2.91}$$

In linear least squares the key assumption is that the system state at time t_i is linearly related to the data observed at t_i. That is, the data taken at a specific time

$\mathbf{z}_i(t_i)$ can be expressed as the observation relation

$$\mathbf{z}_i(t_i) = H_i\mathbf{X}(t_i) + \mathbf{e}_i \tag{2.92}$$

where the data is simply a scalar multiple, H_i, of the state $\mathbf{X}(t_i)$ and the true error of the data $\mathbf{e}_i$. By substituting the dynamics of Equation 2.91 into Equation 2.92 relates the error from a measurement taken at a current time to the state at epoch time t_0

$$\mathbf{e}_i = \mathbf{z}_i(t_i) - H_i\Phi(t_i, t_0)\mathbf{X}(t_0) \tag{2.93}$$

where

$$T_i \equiv H_i\Phi(t_i, t_0) \tag{2.94}$$

Since there are N observations it is convenient to consolidate the data in matrix format. The single observational data vector $\mathbf{z}_i$ may actually contain more than one measurement taken at a single time t_i (e.g. range, azimuth, elevation data taken simultaneously at each time). All the data vectors are assembled into a larger data vector spanning t_1 to t_N

$$\mathbf{z} = \begin{Bmatrix} \mathbf{z}_1 \\ \mathbf{z}_2 \\ \vdots \\ \mathbf{z}_N \end{Bmatrix} \tag{2.95}$$

The observation matrix is formed as

$$T = \begin{Bmatrix} T_1 \\ T_2 \\ \vdots \\ T_N \end{Bmatrix} \tag{2.96}$$

It will be assumed that each data measurement $\mathbf{z}_i$ is statistically independent and therefore, the instrument covariance matrix can be formed of individual covariances on the diagonal with zeros on the off-diagonals. Each covariance Q_i corresponds to each observation $\mathbf{z}_i$

$$Q = \begin{bmatrix} Q_1 & & & \\ & Q_2 & & \\ & & \ddots & \\ & & & Q_N \end{bmatrix} = \begin{bmatrix} \sigma_1^2 & & & \\ & \sigma_2^2 & & \\ & & \ddots & \\ & & & \sigma_N^2 \end{bmatrix} \tag{2.97}$$

where σ_i is the standard deviation of the measurement by the instrument, also denoted as σ_{instr}. The instrument covariance matrix, Q, is square with the dimensions of $N \times N$ where N is the number of observations. Resulting from the derivation provided by Wiesel [15] the estimate of the linear dynamical system $\bar{\mathbf{X}}$ at epoch time t_0 is given by

$$\bar{\mathbf{X}}(t_0) = (T^T Q^{-1} T)^{-1} T^T Q^{-1} \mathbf{z} \tag{2.98}$$

with an associated state covariance $P_{\bar{X}}$ at epoch time t_0

$$P_{\bar{X}}(t_0) = (T^T Q^{-1} T)^{-1} \tag{2.99}$$

2.4.3 Nonlinear Least Squares. With the linear least squares method defined, the nonlinear method will now be developed following the derivation provided by Wiesel [15]. Nonlinear least squares estimation is used in the case of systems whose dynamics is non-linearly related to the observations made. This is applicable to most real-world systems inherently exhibiting nonlinear behavior. Since the state matrix of the system in this thesis includes nonlinear dynamics, where no linear relationship exists between the states and the observations, this nonlinear least squares method will be used.

Begin with the set of equations of motion of the system whose solutions will be found by numerical integration

$$\dot{\mathbf{X}} = \mathbf{f}(\mathbf{X}, t)$$

This numerical integration would result in the explicit solution as a function of time and the initial conditions or initial states

$$\mathbf{X}(t) = \mathbf{h}(\mathbf{X}(t_0), t) \tag{2.100}$$

Developed in the previous section of Linearized Dynamics, the linearization of a nonlinear system results in following statement

$$\delta\mathbf{X}(t) = \mathbf{\Phi}(t, t_0)\delta\mathbf{X}(t_0)$$

with $\delta\mathbf{X}$ as a small change in the state, and the linearized dynamics formed into the State Transition Matrix, $\mathbf{\Phi}$, linearized about some dynamical trajectory. The objective is still to know the true state, $\mathbf{X}_0$, which is unattainable. Earlier in the subsection of Probability Theory, it was discussed that one must settle for an estimate of the state, $\bar{\mathbf{X}}$. However, to initiate the nonlinear least squares estimation process of finding such an estimate, one must initially use a reference trajectory denoted as $\mathbf{X}_{ref}$. $\mathbf{X}_{ref}$ is initially considered the *a priori* estimate of the initial states of the dynamical system at some epoch of time (i.e. the initial educated guess). Using this least squares method, changes in the state $\delta\mathbf{X}$ will be generated to correct the reference trajectory to a point of satisfaction where it can be declared that the reference trajectory $\mathbf{X}_{ref}$ is the estimated trajectory $\bar{\mathbf{X}}$ of the true state $\mathbf{X}_0$.

The observation relation as a function of the state variables and the observation geometry is defined as

$$\mathbf{z}_i(t_i) = \mathbf{G}(\mathbf{X}(t_i), t_i) \tag{2.101}$$

The true error in the observational data is given by the difference between the actual collected measurement and what would be the perfect or true measurement.

$$\begin{aligned} \mathbf{e} &= \mathbf{z} - \mathbf{z_0} && (2.102)\\ &= \mathbf{G}(\mathbf{X}, t) - \mathbf{G}(\mathbf{X}_0, t) && (2.103)\\ &= \mathbf{G}(\mathbf{X}_0 + \delta\mathbf{X}, t) - \mathbf{G}(\mathbf{X}_0, t) && (2.104)\\ &\approx \frac{\partial \mathbf{G}}{\partial \mathbf{X}} \delta\mathbf{X}(t) && (2.105) \end{aligned}$$

As mentioned earlier, it is expected that the true error will be approximately equal to the residual. In order to develop a relationship describing how the observation function would change with respect to a change in the system states, the observation function is linearized with respect to the state variable about the reference trajectory

$$H_i(t_i) \equiv \left.\frac{\partial \mathbf{G}}{\partial \mathbf{X}}\right|_{\mathbf{X}_{ref}(t_i), t_i} \tag{2.106}$$

The residual vector of the observation can be calculated by the difference of the actual measurement and the expected measurement defined by the observation Equation 2.101

$$\mathbf{r}_i = \mathbf{z}_i - \mathbf{G}(\mathbf{X}_{ref}(t_i), t_i) \tag{2.107}$$

The residuals from the observation data with Equation 2.94 follow as

$$\begin{aligned} \mathbf{r}_i &\approx H_i \delta\mathbf{X}(t_i) && (2.108)\\ &= H_i \mathbf{\Phi}(t_i, t_0) \delta\mathbf{X}(t_0) && (2.109)\\ &= T_i \delta\mathbf{X}(t_0) && (2.110) \end{aligned}$$

Similar to the linear least squares method, the result is

$$\delta\mathbf{X}(t_0) = (T^T Q^{-1} T)^{-1} T^T Q^{-1} \mathbf{r} \tag{2.111}$$

Therefore, the equations for nonlinear least squares estimation are

$$P_{\delta X}(t_0) = (T^T Q^{-1} T)^{-1} \tag{2.112}$$

where after convergence would be defined as

$$P_{\bar{X}} = P_{\delta X} \tag{2.113}$$

and the estimated trajectory would then be expressed as

$$\bar{\mathbf{X}}(t_0) = \mathbf{X}_{ref}(t_0) + \delta\mathbf{X}(t_0) \tag{2.114}$$

When or if the reference trajectory converges to a solution these previous equations describe the estimated state of the true system at some epoch t_0.

2.5 Summary

As mentioned earlier, this research is focused on estimating the relative motion dynamics, rotational dynamics, and moments of inertia of the RSO. The theory provided in this chapter yields the equations of motion and associated assumptions governing the dynamics of the Observer-Target system, estimation theory, and the definition of the state vectors.

For relative motion dynamics, the equations of motion for relative position (Equ. 2.23-2.25) and relative velocity (Equ. 2.27-2.29) of the Observer-Target system are developed and consolidated in the form of a state transition matrix (Equ. 2.31). The equations of motion for the moments of inertia (Equ. 2.66-2.68) are provided as well.

Six ordinary differential equations of motion are required to describe the rotational dynamics of the RSO rigid-body. Euler's rotational equations of motion (Equ. 2.43-2.45) are derived along with the remaining three complimentary Euler rate equations (Equ. 2.60-2.62) using a 3-2-1 Euler rotation sequence.

The estimation theory discussed in this chapter covers the linearization methods needed for the dynamics and observation function and the mathematics for implementing the non-linear least squares method in a computer algorithm. Also of great importance, the states which characterize the Observer-Target system at any instance in time is provided in the form of two state vectors (Equ. 2.65 and 2.70). The 12-state vector is used for estimation cases involving relative motion and rotational dynamics of the RSO. In estimating the rotational dynamics and moments of inertia of the RSO, the 9-state vector version is used.

The general theory and assumptions discussed here serve as the basis for the approach taken in the effort to explore the estimation of the dynamics and physical properties (i.e MOI) of the RSO using range observational data. The theory of this chapter is implemented in the methodology developed in the next chapter, specific to this research effort.

III. Methodology

This chapter will begin by formulating the observation function based on the observation geometry of the Observer-Target system involved in the proximity operation. The formulation of the linearized observation function and dynamics will follow. A computer program written in MATLAB was created to model the two-body dynamics of the Observer-Target system. This program, termed the *truth model*, is used as the dynamics model of the system as well as a generater for simulated range measurement data. Finally, the algorithm for the nonlinear least squares estimator is discussed. The estimator program, written in MATLAB, utilizes the simulated range data to estimate the states of the RSO which will provide insight to its dynamical and physical properties.

The original effort of this thesis was to explore the performance of a nonlinear least squares filter for estimating the dynamics of a Target. The rotational velocities and Euler orientation angles were of particular interest. This led to the use of the 12-state dynamics vector as developed in Equation 2.65. Estimated states include the relative position, relative velocity, angular velocity, and Euler angles. In an effort to explore the feasibility of estimating the moments of inertia of the RSO to provide insight into the object's physical properties, a 9-state version of the state vector was created as shown in Equation 2.70. In a scenario where the relative position and velocities are considered known to sufficient accuracy, the estimated parameters include the angular velocity, Euler angles, and moment-of-inertia components of the RSO. This chapter will focus on the development of the H and $\mathbf{\Phi}$ matrices pertaining to the 12-state variable version. The formulation method for the 9-variable version is identical and the program algorithms are not affected. Details specific to the 9-vector version are found in the Appendix A.

3.1 Observation Function

During the space proximity operation, the Observer spacecraft will be collecting range measurements of continuously tracked points on the Target body for the duration of the observational period. The relative position and velocity states of the Observer as well as the Target's rotational states at a given instant in time are related to the range observation made at that particular time. This leads to the purpose of the observation function. The observation function is an expression that is based on the observation geometry shown in Figure 3.1 that results in expected observations as a function of the dynamic state variables. Therefore, given the dynamic states of the Observer-Target system, the range measurement that should be made by the Observer spacecraft can be predicted. This predicted range measurement and the actual range measurement made (using simulated range data) is at the heart of the least-squares estimation process. The observation relation is derived

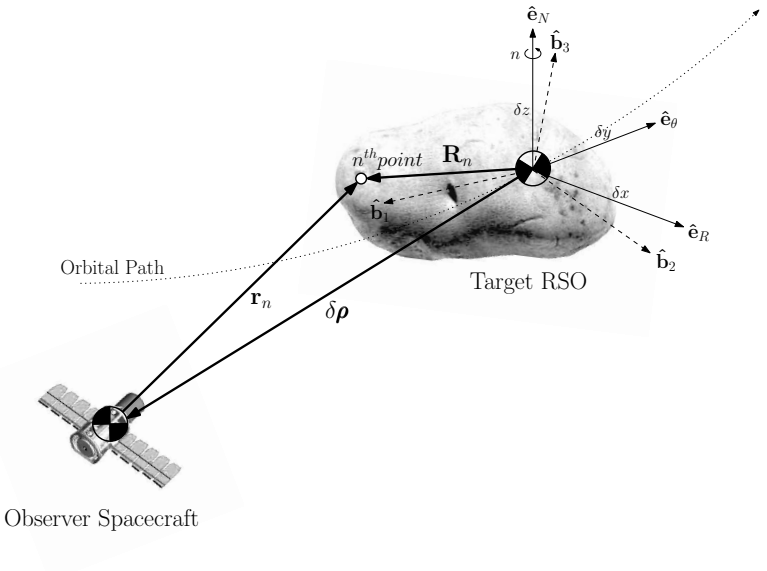

Figure 3.1 Observation Geometry of Observer-Target System

starting with the relative position vector $\delta\boldsymbol{\rho}$. Careful attention is paid to the starting

and terminating points of the vectors.

$$\delta\boldsymbol{\rho} = -\mathbf{r}_n + \mathbf{R}_n \tag{3.1}$$

solving for $\mathbf{r}_n$, yields

$$\mathbf{r}_n = \mathbf{R}_n - \delta\boldsymbol{\rho} \tag{3.2}$$

where the subscript n denotes observation point n on the Target body. The vector $\mathbf{R}_n$ represents the position of point n from the center-of-mass of the Target in $\mathfrak{F}_b$. The vector $\mathbf{r}_n$ is representative of the observation vector as seen from the Observer spacecraft to the observational point on the Target body in $\mathfrak{F}_e$. Although the $\mathbf{r}_n$ vector, by definition, contains magnitude (i.e. range) and directional information, this thesis will only explore range observational data. Therefore, the actual observational quantity is simply the magnitude of the $\mathbf{r}_n$ vector, yielding *range*, denoted by the scalar r_n

$$r_n = \|\mathbf{r}_n\| = \|\mathbf{R}_n - \delta\boldsymbol{\rho}\| \tag{3.3}$$

However, note that the observation function contains vectors of mixed basis. Performing a coordinate frame transformation to $\mathfrak{F}_e$ using the proper rotation matrix (Equ. 2.54) with the previous equation results in the expression below with its time-dependence shown

$$\begin{aligned} \|\mathbf{r}_n^e\| &= \|[\mathbf{R}^{eb}]\mathbf{R}_n^b - \delta\boldsymbol{\rho}^e\| && (3.4)\\ &= \|\mathbf{R}_n^e - \delta\boldsymbol{\rho}^e\| && (3.5)\\ \|\mathbf{r}_n^e(t)\| &= \|\mathbf{R}_n^e(t) - \delta\boldsymbol{\rho}^e(t)\| && (3.6) \end{aligned}$$

define the position vectors of the n^{th} observation point as

$$\mathbf{R}_n^b = \begin{Bmatrix} b_{1_n} \\ b_{2_n} \\ b_{3_n} \end{Bmatrix} \qquad \text{and} \qquad \mathbf{R}_n^e(t) = \begin{Bmatrix} p_{x_n}(t) \\ p_{y_n}(t) \\ p_{z_n}(t) \end{Bmatrix} \tag{3.7}$$

Substituting Equation 3.7 for $\mathbf{R}_n^e$ and Equation 2.4 into Equation 3.6 yields

$$\|\mathbf{r}_n^e\| = \|(p_{x_n}\hat{\mathbf{e}}_R + p_{y_n}\hat{\mathbf{e}}_\theta + p_{z_n}\hat{\mathbf{e}}_N) - (\delta x\hat{\mathbf{e}}_R + \delta y\hat{\mathbf{e}}_\theta + \delta z\hat{\mathbf{e}}_N)\| \tag{3.8}$$

$$\|\mathbf{r}_n^e\| = \|(p_{x_n} - \delta x)\hat{\mathbf{e}}_R + (p_{y_n} - \delta y)\hat{\mathbf{e}}_\theta + (p_{z_n} - \delta z)\hat{\mathbf{e}}_N)\| \tag{3.9}$$

$$r_n = \sqrt{(p_{x_n} - \delta x)^2 + (p_{y_n} - \delta y)^2 + (p_{z_n} - \delta z)^2} \tag{3.10}$$

Finally, the range observation function $\mathbf{G}$ is defined below in terms of the dynamic state variables $\mathbf{X}$ which will predict the range measurement data. This function, as developed here, is unique to the system geometry of this research as illustrated in Figure 3.1.

$$\mathbf{G} = range = \sqrt{(p_{x_n} - \delta x)^2 + (p_{y_n} - \delta y)^2 + (p_{z_n} - \delta z)^2} \tag{3.11}$$

In the case of multiple range measurements to multiple points taken essentially simultaneously, the function $\mathbf{G}$ simply becomes a vector of range measurements for a single observation time

$$\mathbf{G} = \begin{Bmatrix} r_1 \\ r_2 \\ \vdots \\ r_N \end{Bmatrix} = \begin{Bmatrix} \sqrt{(p_{x_1} - \delta x)^2 + (p_{y_1} - \delta y)^2 + (p_{z_1} - \delta z)^2} \\ \sqrt{(p_{x_2} - \delta x)^2 + (p_{y_2} - \delta y)^2 + (p_{z_2} - \delta z)^2} \\ \vdots \\ \sqrt{(p_{x_N} - \delta x)^2 + (p_{y_N} - \delta y)^2 + (p_{z_N} - \delta z)^2} \end{Bmatrix} \tag{3.12}$$

for observation points 1 to N; that is, $n = 1, 2, \ldots, N$.

3.2 Linearization of Observation

This section is devoted to linearizing the observation function to find a linear relationship between the change of the observation with a change in the dynamics state vector. This expression will be denoted as the **H** matrix and will be needed for the estimation algorithm.

In terms of the state variables, note that the final version of the range observation expression, Equation 3.11, is a function of the CW relative position vector and the position vector of the observation point in $\mathfrak{F}_e$. However, the observation point in $\mathfrak{F}_e$ is a function of the Euler orientation angles due to the rotation of the body frame of the Target. The version of the observation function in terms of the relative position state variable, $\delta\boldsymbol{\rho}$, and the Target observation point position, a non-state variable, is given by Equation 3.11 as

$$\mathbf{G} = r_n = \sqrt{(p_{x_n} - \delta x)^2 + (p_{y_n} - \delta y)^2 + (p_{z_n} - \delta z)^2}$$

From Equation 2.106, recall the linearized observation function with respect to the state vector is defined as

$$\mathbf{H}_i(t_i) \equiv \frac{\partial \mathbf{G}}{\partial \mathbf{X}}(\mathbf{X}_{ref}(t_i), t_i) \tag{3.13}$$

Note that the range equation, Equation 3.11, is a function of δx, δy, δz, p_{x_n}, p_{y_n}, and p_{z_n} at any moment in time. In terms of the dynamics state variables, the range equation is only a function of δx, δy, δz, θ_1, θ_2, and θ_3. For simplicity, all other state variables which the range equation is not a function of are ignored till the end. This results in

$$\mathbf{H} = \frac{\partial \mathbf{G}}{\partial \mathbf{X}} = \begin{bmatrix} \frac{\partial \mathbf{G}}{\partial \delta x} & \frac{\partial \mathbf{G}}{\partial \delta y} & \frac{\partial \mathbf{G}}{\partial \delta z} & \frac{\partial \mathbf{G}}{\partial \theta_1} & \frac{\partial \mathbf{G}}{\partial \theta_2} & \frac{\partial \mathbf{G}}{\partial \theta_3} \end{bmatrix} \tag{3.14}$$

Recalling that p_{x_n}, p_{y_n}, and p_{z_n} are functions of the Euler angles at specific moments in time due to the rotation of the Target body, the **H** matrix can simply be found using the chain rule in the following fashion

$$\mathbf{H} = \begin{bmatrix} \frac{\partial \mathbf{G}}{\partial \delta x} & \frac{\partial \mathbf{G}}{\partial \delta y} & \frac{\partial \mathbf{G}}{\partial \delta z} & \frac{\partial \mathbf{G}}{\partial p_{x_n}} & \frac{\partial \mathbf{G}}{\partial p_{y_n}} & \frac{\partial \mathbf{G}}{\partial p_{z_n}} \end{bmatrix} \begin{bmatrix} 1 & 0 & 0 & 0 & 0 & 0 \\ 0 & 1 & 0 & 0 & 0 & 0 \\ 0 & 0 & 1 & 0 & 0 & 0 \\ 0 & 0 & 0 & \frac{\partial p_{x_n}}{\partial \theta_1} & \frac{\partial p_{x_n}}{\partial \theta_2} & \frac{\partial p_{x_n}}{\partial \theta_3} \\ 0 & 0 & 0 & \frac{\partial p_{y_n}}{\partial \theta_1} & \frac{\partial p_{y_n}}{\partial \theta_2} & \frac{\partial p_{y_n}}{\partial \theta_3} \\ 0 & 0 & 0 & \frac{\partial p_{z_n}}{\partial \theta_1} & \frac{\partial p_{z_n}}{\partial \theta_2} & \frac{\partial p_{z_n}}{\partial \theta_3} \end{bmatrix} \tag{3.15}$$

The partial derivatives shown above (and found in Appendix A) are coded into the program and the matrix multiplication is carried out by the computer program. The state variables which are not involved are simply zero. This results in the solution of $\mathbf{H}_i$ for every observation time t_i.

In terms of the 12-state vector, defined as

$$\mathbf{X} = \begin{bmatrix} \delta x & \delta y & \delta z & \delta \dot{x} & \delta \dot{y} & \delta \dot{z} & \omega_1 & \omega_2 & \omega_3 & \theta_1 & \theta_2 & \theta_3 \end{bmatrix}^T$$

the linearized observation function is the solution to

$$\mathbf{H} = \begin{bmatrix} \frac{\partial \mathbf{G}}{\partial \delta x} & \frac{\partial \mathbf{G}}{\partial \delta y} & \frac{\partial \mathbf{G}}{\partial \delta z} & 0 & 0 & 0 & 0 & 0 & 0 & \frac{\partial \mathbf{G}}{\partial \theta_1} & \frac{\partial \mathbf{G}}{\partial \theta_2} & \frac{\partial \mathbf{G}}{\partial \theta_3} \end{bmatrix} \tag{3.16}$$

In terms of the 9-state vector, defined as

$$\mathbf{X} = \begin{bmatrix} \omega_1 & \omega_2 & \omega_3 & \theta_1 & \theta_2 & \theta_3 & A & B & C \end{bmatrix}^T$$

where the relative position variables are considered known constants for each observation time and are then not estimated states, the linearized observation relation is

simply the solution to

$$\mathbf{H} = \begin{bmatrix} 0 & 0 & 0 & \frac{\partial \mathbf{G}}{\partial \theta_1} & \frac{\partial \mathbf{G}}{\partial \theta_2} & \frac{\partial \mathbf{G}}{\partial \theta_3} & 0 & 0 & 0 \end{bmatrix} \tag{3.17}$$

3.3 Linearization of Dynamics

This section will show how the dynamics of the system is linearized resulting in the formulation of the state transition matrix, $\mathbf{\Phi}$. This formulation will be shown for the 12-state vector version. The 9-state vector version will simply follow the same method and is given in Appendix B.

Recall from Equation 2.31 that the CW state transition matrix Φ_{cw} is already known. Therefore, the state transition matrix for the rotational portion of the dynamics is in need. As defined in Chapter 2, the rotational state vector is

$$\mathbf{X}_{rot}(t) = \begin{bmatrix} \omega_1 & \omega_2 & \omega_3 & \theta_1 & \theta_2 & \theta_3 \end{bmatrix}^T$$

Therefore, applying Equation 2.71, the time-derivative of the state vector is shown below. The vector function, $\mathbf{f}$, is then associated with each state equation of motion. Functions f_1, f_2, f_3, correspond to Equations 2.43, 2.44, 2.45 and functions f_4, f_5, f_6, correspond to Equations 2.60, 2.61, and 2.62, respectively.

$$\dot{\mathbf{X}}_{rot}(t) = \begin{Bmatrix} \dot{\omega}_1 \\ \dot{\omega}_2 \\ \dot{\omega}_3 \\ \dot{\theta}_1 \\ \dot{\theta}_2 \\ \dot{\theta}_3 \end{Bmatrix} = \begin{Bmatrix} f_1 \\ f_2 \\ f_3 \\ f_4 \\ f_5 \\ f_6 \end{Bmatrix} = \mathbf{f}(t) \tag{3.18}$$

From Equation 2.77, the partial derivatives of the equations of motion with respect to the state variables of the rotational dynamics are symbolically shown below (the solution is found in Appendix B)

$$A = \begin{bmatrix} \frac{\partial f_1}{\partial \omega_1} & \frac{\partial f_1}{\partial \omega_2} & \frac{\partial f_1}{\partial \omega_3} & \frac{\partial f_1}{\partial \theta_1} & \frac{\partial f_1}{\partial \theta_2} & \frac{\partial f_1}{\partial \theta_3} \\ \frac{\partial f_2}{\partial \omega_1} & \frac{\partial f_2}{\partial \omega_2} & \frac{\partial f_2}{\partial \omega_3} & \frac{\partial f_2}{\partial \theta_1} & \frac{\partial f_2}{\partial \theta_2} & \frac{\partial f_2}{\partial \theta_3} \\ \frac{\partial f_3}{\partial \omega_1} & \frac{\partial f_3}{\partial \omega_2} & \frac{\partial f_3}{\partial \omega_3} & \frac{\partial f_3}{\partial \theta_1} & \frac{\partial f_3}{\partial \theta_2} & \frac{\partial f_3}{\partial \theta_3} \\ \frac{\partial f_4}{\partial \omega_1} & \frac{\partial f_4}{\partial \omega_2} & \frac{\partial f_4}{\partial \omega_3} & \frac{\partial f_4}{\partial \theta_1} & \frac{\partial f_4}{\partial \theta_2} & \frac{\partial f_4}{\partial \theta_3} \\ \frac{\partial f_5}{\partial \omega_1} & \frac{\partial f_5}{\partial \omega_2} & \frac{\partial f_5}{\partial \omega_3} & \frac{\partial f_5}{\partial \theta_1} & \frac{\partial f_5}{\partial \theta_2} & \frac{\partial f_5}{\partial \theta_3} \\ \frac{\partial f_6}{\partial \omega_1} & \frac{\partial f_6}{\partial \omega_2} & \frac{\partial f_6}{\partial \omega_3} & \frac{\partial f_6}{\partial \theta_1} & \frac{\partial f_6}{\partial \theta_2} & \frac{\partial f_6}{\partial \theta_3} \end{bmatrix} \tag{3.19}$$

The state transition matrix for the rotational portion is defined as

$$\mathbf{\Phi}_{rot} = \begin{bmatrix} \phi_{11} & \phi_{12} & \phi_{13} & \phi_{14} & \phi_{15} & \phi_{16} \\ \phi_{21} & \phi_{22} & \phi_{23} & \phi_{24} & \phi_{25} & \phi_{26} \\ \phi_{31} & \phi_{32} & \phi_{33} & \phi_{34} & \phi_{35} & \phi_{36} \\ \phi_{41} & \phi_{42} & \phi_{43} & \phi_{44} & \phi_{45} & \phi_{46} \\ \phi_{51} & \phi_{52} & \phi_{53} & \phi_{54} & \phi_{55} & \phi_{56} \\ \phi_{61} & \phi_{62} & \phi_{63} & \phi_{64} & \phi_{65} & \phi_{66} \end{bmatrix} \tag{3.20}$$

and the time-derivative of the state transition matrix is simply defined as

$$\dot{\mathbf{\Phi}}_{rot} = \begin{bmatrix} \dot{\phi}_{11} & \dot{\phi}_{12} & \dot{\phi}_{13} & \dot{\phi}_{14} & \dot{\phi}_{15} & \dot{\phi}_{16} \\ \dot{\phi}_{21} & \dot{\phi}_{22} & \dot{\phi}_{23} & \dot{\phi}_{24} & \dot{\phi}_{25} & \dot{\phi}_{26} \\ \dot{\phi}_{31} & \dot{\phi}_{32} & \dot{\phi}_{33} & \dot{\phi}_{34} & \dot{\phi}_{35} & \dot{\phi}_{36} \\ \dot{\phi}_{41} & \dot{\phi}_{42} & \dot{\phi}_{43} & \dot{\phi}_{44} & \dot{\phi}_{45} & \dot{\phi}_{46} \\ \dot{\phi}_{51} & \dot{\phi}_{52} & \dot{\phi}_{53} & \dot{\phi}_{54} & \dot{\phi}_{55} & \dot{\phi}_{56} \\ \dot{\phi}_{61} & \dot{\phi}_{62} & \dot{\phi}_{63} & \dot{\phi}_{64} & \dot{\phi}_{65} & \dot{\phi}_{66} \end{bmatrix} \tag{3.21}$$

The matrices above are coded into the estimation program and using a Runga-Kutta algorithm, the numerical solution to Equation 2.80

$$\dot{\mathbf{\Phi}}_{rot}(t,t_0) = A(t)\mathbf{\Phi}_{rot}(t,t_0)$$

is solved for resulting in $\mathbf{\Phi}_{rot}(t,t_0)$. Incorporating the CW portion (Equ.2.31), results in the newly developed 12×12 state transition matrix for the 12-state vector version used in the estimation process

$$\mathbf{\Phi}(t,t_0) \;=\; \left[\begin{array}{c|c} \mathbf{\Phi}_{cw}^{6\times6} & 0^{6\times6} \\ \hline 0^{6\times6} & \mathbf{\Phi}_{rot}^{6\times6} \end{array}\right] \tag{3.22}$$

Following the same methodology, with the omission of the CW states and changes to the A matrix to include the moment-of-inertia terms, the 9-state vector version of the 9×9 state transition matrix is developed and shown in Appendix B.

3.4 Truth Model and Data Generator

A truth model of the dynamics was created to provide a basis for comparison between the simulated actual dynamics and the estimated dynamics. Also, the truth model provides a method of generating observational range data since no real-world experimental data was available for this effort. Both the Truth Model and the Data Generator were coded in MATLAB.

The Truth Model generates two-body deterministic dynamics data for relative position, relative velocity, Target angular velocity, Target Euler angle orientation, and Target moments of inertia for the Observer-Target system for the duration of the proximity operation in which range observations are being made. Assumptions programmed into the Truth Model are as follows:

- Target RSO is in a true circular orbit about the Earth
- Moments of Inertia of the Target are constant

- No perturbations exist

The Data Generator is a program which uses the Truth Model to provide a dynamical scenario in which observational range data would be taken by the Observer spacecraft. With the dynamics data generated for each moment in time, the observation function (Equ. 3.11) is used to generate observational range measurements. Two forms of range measurements are created by this program.

- Perfect range measurements with no error
- Noisy range measurements containing Gaussian noise

The pseudo-random Gaussian noise is added to the perfect range data to simulate real-world data containing measurement error. Assumptions incorporated into the Data Generator are as follows:

- The time vector associated with the dynamics propagation is identical to the observation time vector.
- Observation measurements are taken at constant time steps. A non-continuous data scenario is not considered.
- Observational range sensor and pattern-recognition capability provides an ability to track user-defined points on the Target body for the duration of the observation time vector. Data acquisition limitations due to physical obstructions are not considered.
- For the simulated range data with noise, the standard deviation of instrument error making the range measurements is known and is constant through the observational period.
- All measurements are statistically independent
- Target observation points are known in $\mathfrak{F}_b$

The program architecture of the Truth Model (including the Data Generator) developed for this thesis is shown in Figure 3.2.

Truth Model Program Architecture

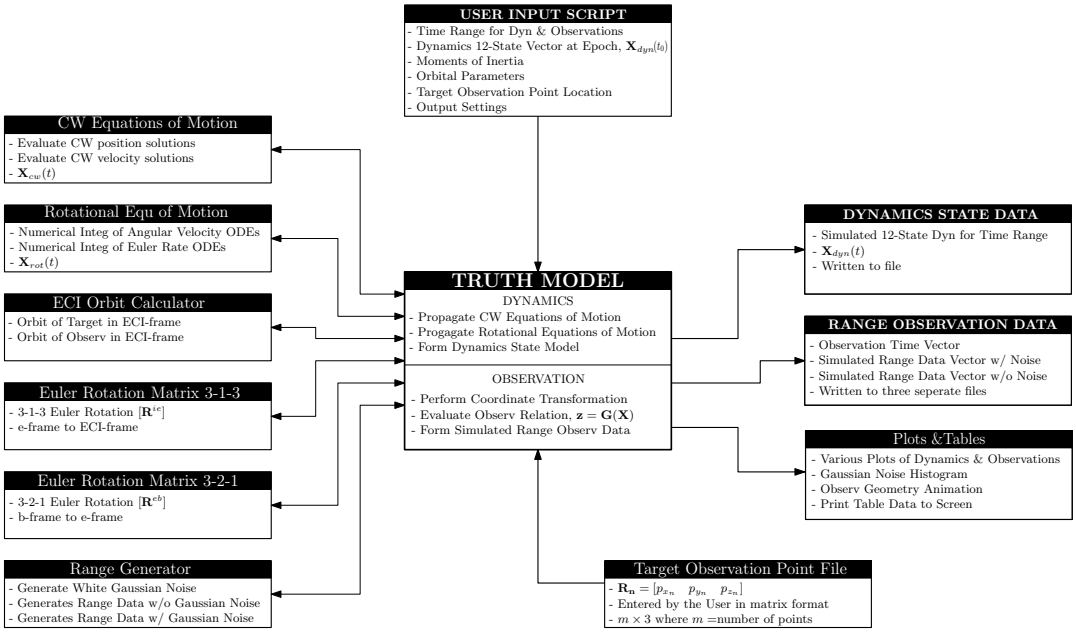

Figure 3.2 Truth Model Architecture

3.4.1 Program Execution. Following Figure 3.2, in the user-input script, the user enters the initial values for the state variables at epoch. That is, the initial conditions for the CW relative position, CW relative velocity, angular velocity of the Target, and Euler orientation angles of the Target, as well as moments of inertia are defined. The altitude of the Target RSO is also entered as well as the epoch start time, time-step, and propagation time in terms of orbital period. For the observation portion of the Truth Model, the number of Target observation points to generate simulated range data for is entered. The standard deviation of the range data is also entered. A separate file containing the vector positions of the observation points in $\mathfrak{F}_b$ is created by the user. This provides the initial conditions and constants needed for the dynamics portion of the Truth Model. Using the CW solutions for relative position and velocity, the CW states are solved for every time, t_i. Using the built-in MATLAB Runga-Kutta *ode45* routine, the numerical solution to the

rotational equations of motion are determined for t_i. This results in the propagated dynamics which is written to a file. The observation portion of the Truth Model reads the dynamics data file and the file containing the observation points, along with the user's input of error to generate simulated range observation data with noise and without. The range data along with the observation time vector is written to separate files for use by the Estimator program. Various plots, histograms, and tables are also produced.

3.4.2 Program Validation. Several methods were used in the validation of the Truth Model code. For the CW relative position and velocity dynamics, the analytical solution was simply verified by hand-calculations for arbitrary data points. Also, test cases using relative velocity components in the cross-track, radial-track, and in-track directions were used to check for the expected effects of orbital drift, eccentricity changes, inclination changes, and combinations of such.

The validation of the rotational dynamics portion of the model was more involved. Hand-calculations were performed for only single-axis rotations to verify angular velocities and Euler orientation angles. Also, using the Target's moments of inertia and angular velocities, test cases were accomplished to check for rotational stability about the major, minor, and intermediate axes. Finally, conservation of angular momentum and conservation of energy checks were built into the code using

$$\|\mathbf{H}\| = \|I\boldsymbol{\omega}^{bi}\| = constant$$

$$KE = \frac{1}{2}\boldsymbol{\omega}^{bi} \cdot I\boldsymbol{\omega}^{bi} = constant$$

where the magnitude of the angular momentum $\mathbf{H}$ is constant in $\mathfrak{F}_b$ (Equ. 2.34). The kinetic energy of the rigid Target body is denoted as KE and given by the dot product shown above. These checks scan through the generated data to ensure

constant values of angular momentum and kinetic energy are within a tolerance set to 10^{-8}.

3.4.3 Simulated Range Data. Using the vector location of the observation point and the CW relative position vector from the generated dynamics data, the observation function (Equ. 3.11) is evaluated to produce simulated range data. Based on the probability theory discussed in Chapter 2, the spacecraft observation sensor will be plagued with measurement errors following a Gaussian distribution (Fig. 2.5); Gaussian noise is added to the perfect range data to simulate real-world data containing measurement error. A MATLAB pseudo-random number generator is used to create the Gaussian noise which is initialized with every execution using the current computer clock time as the seed. Figure 3.3 illustrates a sample distribution of the Gaussian noise for an arbitrary data set spanning one orbital period.

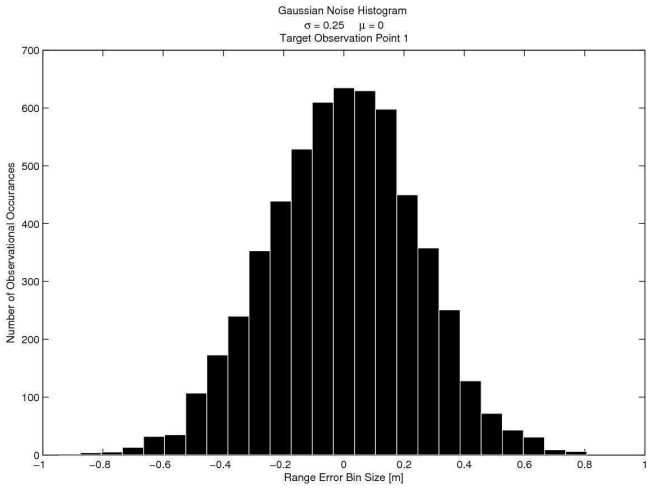

Figure 3.3 Sample Gaussian Noise Distribution

Research indicated that commercially available LIDAR sensors claim range accuracies from $1\,m$ to $7\,mm$ (one sigma) from distances of near $100\,m$ [24, 12, 25]. Since this thesis is focused on estimating the dynamical properties of an RSO for the

intention of performing a proximity operation possibly involving spacecraft-to-target interaction, a range accuracy under one meter is a realistic expectation. Therefore, for the purpose of this research, the range measurement accuracy will be set to 25 cm (one sigma) for all cases. The noise error simulated in a sample data batch is shown in Figure 3.4

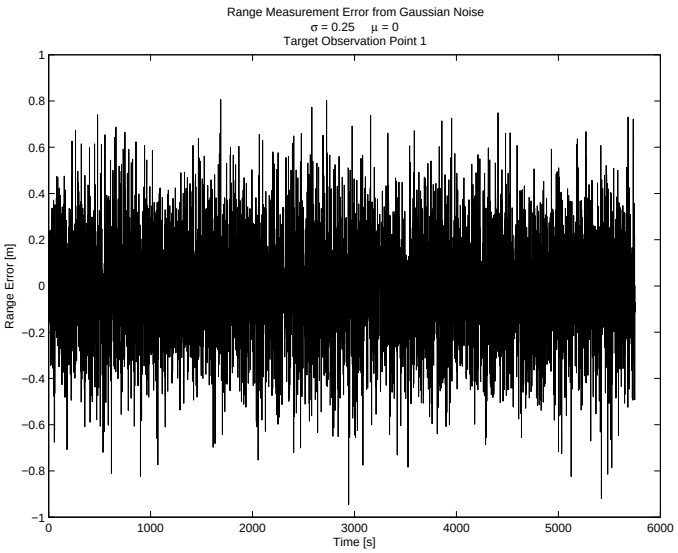

Figure 3.4 Sample Range Measurement Noise Error

3.5 Nonlinear Least Squares Estimator

This section will discuss the nonlinear least squares estimator that was created to estimate the states of the RSO. This program written in MATLAB is illustrated in Figure 3.5. Two different approaches of the estimation are attempted. Although, both versions involve the same process and same methodology, the outcome is different.

The first estimation approach uses the standard 12-state vector (Equ. 2.65) to estimate the relative motion and rotational dynamics of the Target. This method provides an estimate of the CW position, CW velocities, angular velocities, and Euler orientation angles. The second approach used in this thesis was motivated

by an effort to explore the feasibility of estimating the moments of inertia of the RSO directly based on range observations. In this effort, the relative position data is considered known-processed data through some prior estimation filter or data refinement method. That is, the relative position data will not be included in the least squares estimation process; rather, it will be supplied to the algorithm but treated as known information. In this 9-state version (Equ. 2.70), the state variables estimated are the angular velocities, Euler angles, and moments of inertia of the RSO. This method allows the estimator to focus its effort solely on estimating the rotational dynamics and moments of inertia of the Target, providing insight into both its dynamical and physical properties. The results of both approaches will be presented in Chapter 4.

Estimator Program Architecture

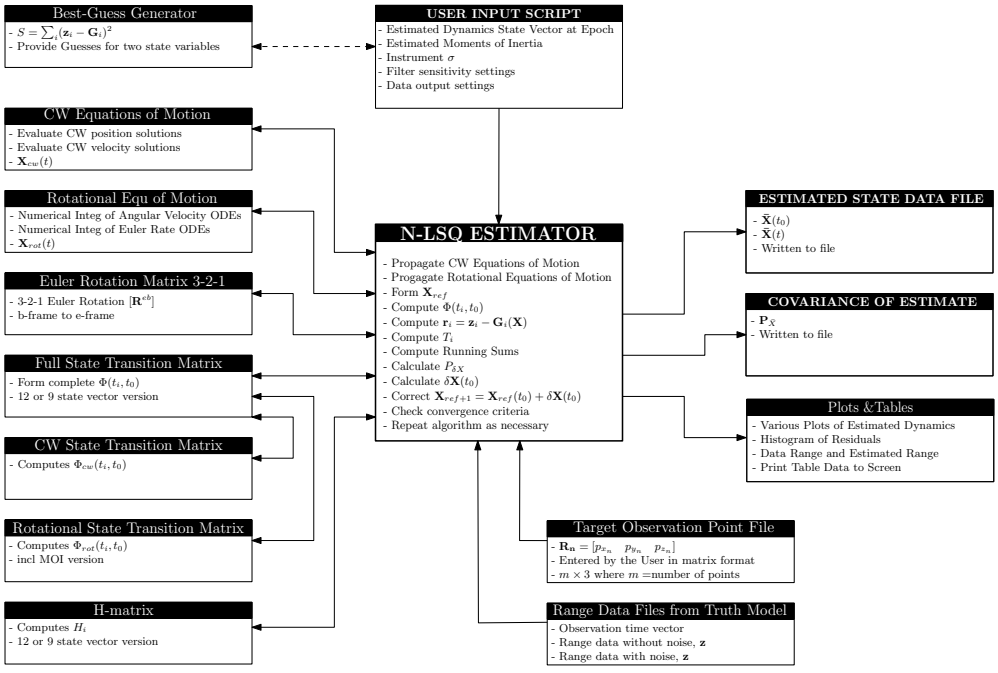

Figure 3.5 Estimator Architecture

3.5.1 Algorithm. Following the theory provided in Chapter 2 for nonlinear least squares and following the algorithm by Wiesel [15], the estimation algorithm is as follows:

1. Input *a priori* estimate of states at epoch
   - $\mathbf{X}(t_0)$
2. Read data files produced by Truth Model
   - Observation time vector
   - Range data with or without noise
   - File containing target observation points
3. Process all observational data for each time t_i
   - Propagate state vector, $\mathbf{X}(t_i)$
   - Calculate $\mathbf{\Phi}(t_i, t_0)$
   - Calculate $\mathbf{r}_i = \mathbf{z}_i - \mathbf{G}(\mathbf{X})$
   - Calculate $T_i = H_i \mathbf{\Phi}(t_i, t_0)$
   - Calculate and store the running sum $\sum_i T_i^T Q_i^{-1} T_i$
   - Calculate and store the running sum $\sum_i T_i^T Q_i^{-1} \mathbf{r}_i$
4. Calculate the correction covariance
   - $P_{\delta X} = \left(\sum_i T_i^T Q_i^{-1} T_i \right)^{-1}$
5. Calculate epoch state correction
   - $\delta \mathbf{X}(t_0) = k_1 P_{\delta X} \left(\sum_i T_i^T Q_i^{-1} \mathbf{r}_i \right)$
6. Correct the Reference Trajectory at epoch
   - $\mathbf{X}_{ref+1}(t_0) = \mathbf{X}_{ref}(t_0) + \delta \mathbf{X}(t_0)$

7. Determine Convergence

   - Covariance criteria check: $|\delta\mathbf{X}_i(t_0)| \ll k_2\sqrt{P_{\delta X_{ii}}}$
   - Residuals σ criteria check: $\sigma_{instr} \approx \sigma_{resid}$, tolerance defined by k_3
   - If criteria is *not* satisfied, begin next iteration at step 3. Otherwise, proceed to step 8

8. Declare Estimate

   - Estimate trajectory is $\bar{\mathbf{X}}(t_0) = \mathbf{X}_{ref}(t_0)$
   - Covariance of estimate is $P_{\bar{X}} = P_{\delta X}$

3.5.2 Validation. Several methods were used to verify the correctness and functionality of the estimator and its major modules. For state propagation and observation relation calculations, the estimator program calls the same validated script files used by the validated Truth Model program. The linearized observation relation was check by this approximation

$$H_{ij} \approx \frac{\mathbf{G}_i(\mathbf{X}_j + \delta\mathbf{X}_j) - \mathbf{G}_i(\mathbf{X}_j)}{\delta\mathbf{X}_j} \tag{3.23}$$

and the linearized dynamics was checked similarly with this relation

$$A_{ij} \approx \frac{\mathbf{f}_i(\mathbf{X}_j + \delta\mathbf{X}_j) - \mathbf{f}_i(\mathbf{X}_j)}{\delta\mathbf{X}_j} \tag{3.24}$$

This was accomplished for rows i and columns (i.e. state variables) j using small ($\sim 10^{-4}$) state changes $\delta\mathbf{X}_j$, one state variable at a time, for arbitrary test cases. The state transition matrix was checked to ensure this property was upheld

$$\mathbf{\Phi}(t_2, t_0) = \mathbf{\Phi}(t_2, t_1)\mathbf{\Phi}(t_1, t_0) \tag{3.25}$$

Overall functionality of the estimator was checked by setting the *a priori* state estimates at t_0 to the actual true states at t_0 used by the truth model to generate the data. As expected, a perfect guess generated a perfect estimate (i.e. the true trajectory) with zero residuals for all observations.

3.5.3 RSS Guess Generator. Step 1 of the estimation algorithm calls for the user to enter the *a priori* estimate of the states at epoch, $\mathbf{X}(t_0)$. Simply put, the key to success in this estimation process is having a *good* initial guess of $\mathbf{X}(t_0)$ for the estimator to begin its iterative routine with. In general, there is no guarantee that the algorithm will converge on the actual trajectory, unless the initial guess matches the actual true states at epoch exactly. But an initial estimate sufficiently close to the truth will drastically improve the outcome. The least squares algorithm, through its iterative process, strives to minimize the sum of the residuals squared, or the function S

$$S = \mathbf{r}^T Q^{-1} \mathbf{r} \tag{3.26}$$

This function is minimized to a *local* minimum. However, this function may actually have other extrema besides the local minimum where the desired solution lies [15]. Movement to any other local minimum would result in a case where the algorithm does not converge to the *desired* solution. For this reason, the Residual Sum Squared (RSS) guess program was created. This program attempts to find the global minimum using

$$RSS(X_1, X_2) = \sum_i (\mathbf{z}_i - \mathbf{G})^2 \tag{3.27}$$

as a function of two state variables that drive $S \longrightarrow 0$. It should be noted that use of the RSS guess program is optional and independent of the estimation program.

This RSS Guess Generator will only provide a best-guess solution for two state variables of interest. It is assumed that the user has *a priori* knowledge of all other variables with a certain level of confidence for input into the estimation algorithm. The limitation to two state variables for this program is simply due to the multi-

dimensional nature of this problem and the computational intensity involved. In this thesis, the rotational states of the Target are of particular interest. Therefore, the guess generator will be used to estimate two of the three rotational velocity components of the Target. The RSS guess generator algorithm flows as such

1. Select two state parameters of interest for a generated guess
    - Choose two of the three: ω_1, ω_2, ω_3
2. Input the guess bound for each state variable
    - Parameter 1: $a \leq \omega \leq b$
    - Parameter 2: $c \leq \omega \leq d$
3. Input the guess increment or step-size within the bound
    - Create a vector of parameter 1 values from a to b
    - Create a vector of parameter 2 values from c to d
4. Compute the predicted range measurements
    - Using every combination of parameter 1 and parameter 2 values, augmented with the remainder of the states, assemble $\mathbf{X}(t_0)$, and propagate the dynamics to each observation time t_i.
    - Compute $\mathbf{G}(\mathbf{X})$ for each observation time t_i
    - Read range data from Truth Model output file, $\mathbf{z}_i$
5. Compute RSS solution
    - Compute sum $RSS = \sum_i (\mathbf{z}_i - \mathbf{G})^2$ for the data batch as a function of parameters 1 and 2
6. Output best-guess solution

- Output: 3-D surface plot where the x-axis corresponds to parameter 1 values, y-axis corresponds to parameter 2 values, and the z-axis corresponds to the RSS value for the combination.
- Locate the global minimum value of RSS.
- Using the RSS global minimum, provide the corresponding parameters 1 and 2 values as the best guess solution.

If computational time is not of concern, and the values of two state variables at epoch are not well known, this tool can provide an extremely good estimate for the two parameters given a range that may span three orders of magnitude. Implementation of this tool will be shown in the next chapter.

3.5.4 Program Execution. To begin, the user enters the *a priori* estimate of the states at epoch with or without the help of the RSS Guess Generator. It is also here that the user must select the 12-state or 9-state version for the estimation process and the number of observational points to use. Also selected is the data mode for the processing of range data with noise or without noise. The user has control of tuning the sensitivity of the estimator algorithm by adjusting the filter setting for the k_1, k_2, and k_3 scaling coefficients. This will be discussed in the next subsection. The maximum number of iterations and the instrument covariance value in terms of σ_{instr} are also defined. This value of σ_{instr} should be consistent with the standard deviation value used in the Truth Model. The user also has the option of processing the entire data batch or a portion as well as forcing the estimator to run a specified number of iterations. Various other switches in the user-input script control the types of output such as plots and tables. Once the program is executed, built-in checks are performed to enure compatible range data, observational points, and time data. The estimator will recursively execute the least-squares algorithm portion of the code until either all convergence criteria are satisfied or the number of maximum iterations is reached. At that point, the program will

leave the iterative loop and propagate the estimated dynamics based on the last valid estimated $\mathbf{X}_{ref}(t_0)$. Depending on the user's output selection, various plots and tables will be displayed or printed. Plots that are available include: comparison plots of actual and estimated dynamics, actual and predicted range observations, and the distribution of residuals. Also filter performance data is printed to the screen such as the standard deviation of the residuals, number of iterations, convergence status, and covariance values.

3.5.5 Convergence Criteria. In the estimation program, two factors are used to judge convergence to an acceptable estimate of the true solution. The first factor is the relative comparison between the state correction $\delta\mathbf{X}$ and its associated covariance term $P_{\delta X_{ii}}$. When successive solutions of $\delta\mathbf{X}$ lie within the error ellipsoid indicated by the covariance matrix, no further iterations are meaningful to compute [15]. This convergence criterion coded into the algorithm is expressed as

$$|\delta\mathbf{X}_i(t_0)| \ll k_2\sqrt{P_{\delta X_{ii}}} \tag{3.28}$$

where the absolute value of the state correction, $\delta\mathbf{X}_i(t_0)$, must be much less that the square root of the diagonal terms of the covariance matrix $P_{\delta X_{ii}}$ scaled down by the coefficient k_2. Typical values explored for k_2 compare $\delta\mathbf{X}_i(t_0)$ to 1% to 50% of $\sqrt{P_{\delta X_{ii}}}$. Specific k_2 values will be stated in the next chapter for actual cases. The diagonal values of the covariance, $P_{\delta X_{ii}}$, effectively correspond to the i^{th} state which is being compared to the corresponding i^{th} state in $\delta\mathbf{X}_i(t_0)$.

The second parameter, used for ensuring convergence, is the statistical distribution of the residuals from the estimated trajectory. Residuals that are sufficiently small enough will result in a Gaussian distribution that has a standard deviation comparable to the original standard deviation of the data batch. A conditional

statement is coded in the algorithm to check if the following relation is true

$$\sigma_{instr} \approx \sigma_{resid} \tag{3.29}$$

where σ_{instr} is the standard deviation associated with the instrument measurements defined in the Q matrix. The standard deviation of the residuals from the estimation is σ_{resid}. The k_3 scaling coefficient is used to specify a percentage of error that is acceptable for Equation 3.29. Although, $\delta\mathbf{X}_i(t_0)$ may be relatively small and meet the first criterion above, the residuals may indicate a different story since the residuals are not dependent on the covariance $P_{\delta X}$. In a common case where the first criterion is met but the residuals are not sufficiently small, results in a σ_{resid} that is near or approaching σ_{instr}. This condition is easily identified by a Gaussian distribution of the residuals which appears to have a non-zero mean. The k_3 coefficient is chosen such that the mean of the residual distribution is *near* zero satisfying Equation 3.29 above. Allowing the algorithm to perform a couple more successive iterations typically corrects this non-zero mean problem and results in a fully converged solution.

Stability of the estimator is controlled by the k_1 scaling coefficient. This coefficient scales the state correction variables proportionally by a constant. A modified form of Equation 2.4.3 is used in the algorithm as shown below

$$\delta\mathbf{X}(t_0) = k_1 P_{\delta X} \sum_i T_i^T Q_i^{-1} \mathbf{r}_i \tag{3.30}$$

Cases exist which the estimator fails to converge on a solution by inadvertently maximizing the S function, easily identified by residuals approaching infinity. By proportionally scaling down the state correction vector using k_1, the algorithm behaves more stable by making smaller corrections and typically moves toward the desired solution, albeit through more iterations than would normally be required.

IV. Simulation & Results

Beginning with a hypothetical scenario that provides a basis for the *a priori* knowledge needed for this estimation process, this Chapter will explore three estimation cases through simulation. The initial conditions formed from the scenario will be the basis for the estimation cases. The three cases will explore the effects of the following on the success of the nonlinear least squares estimator: noisy data, the *a priori* estimates, and the number of observational points used (i.e. number of data batches processed). Each case will result in estimates of the rotational dynamics and moments of inertia, which will provide insight into the dynamical and physical properties of the hypothetical resident space object.

4.1 Scenario

Consistent with the assumptions made in the derivation of the equations of motion for the system dynamics, the Target is assumed to be in a true circular orbit, free from external perturbations, for the duration of the simulated proximity operation in which observational data is being collected. The Target is said to be in LEO with an altitude of $800\,km$ ($497\,mi$). In nonlinear least squares estimations, having initial estimates or *a priori* knowledge of the state parameters is required. Choosing the initial values for these parameters is absolutely critical in the estimation outcome (i.e. convergence vs. divergence) as well as the quality of the estimated solution (i.e. believable or physically impossible). Although it is the goal to ultimately estimate the rotational dynamics and moments of inertia of the RSO, the estimation process cannot start without some initial information for these parameters. Ideally, if the target is categorized as *cooperative*, the technical data of the RSO would be considered available and known with relatively high accuracy. However, for *uncooperative* RSO targets, this may pose a challenge requiring some creativity for developing the initial estimates and associated physical information (i.e. mass, moments of inertia,

dimensions, structure, etc). In such cases several methods and tools exist to aid in the development of this information. One method is space surveillance using ground radar. FGAN Research Institute for High-Frequency Physics and Radar Techniques in Wachtberg, Germany, utilizes a 34-meter Tracking and Imaging Radar (TIRA) to investigate radar techniques for space surveillance applications [26]. One application is providing attitude and configuration information for anomaly resolution [26]. After the Japanese Advanced Earth Observation Satellite-I (ADEOS-I) spacecraft experienced a malfunction in 1997, FGAN was able to use radar imagery of the spacecraft along with a wire-grid model analysis to determine the loss of the $0.5\,mm$-thick solar panel as well as the spacecrafts angular velocity components [26, 27, 28].

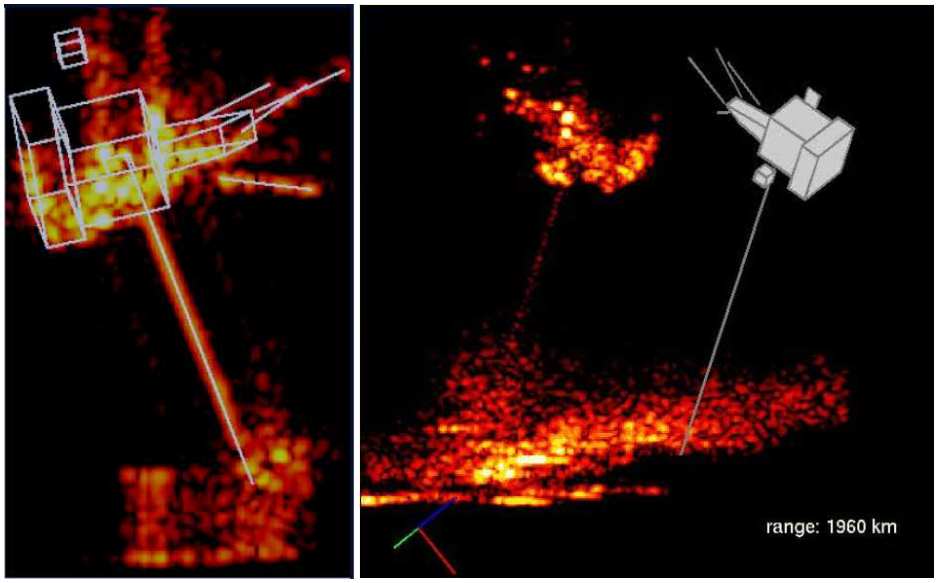

Figure 4.1 Radar Image of the ADEOS I Spacecraft (courtesy of FGAN-FHR)

FGAN determined that the spacecraft was rotating about two axes with angular velocities of approximately $0.1\,deg/s$ and $0.4\,deg/s$ [26, 28]. Using these quantities solely as *a priori* knowledge for this scenario, the angular velocities will be *arbitrarily* assigned to the following axes in the body frame of the Target.

$$\omega_1 = 0.0069\,\frac{rad}{s} \qquad \text{and} \qquad \omega_3 = 0.0017\,\frac{rad}{s} \tag{4.1}$$

Strictly for *visualization* purposes, the ADEOS I spacecraft will represent the generic RSO Target body used in this simulation. Its distinctive geometry and partially known characteristics make it well suited for this scenario. Therefore, Figure 4.2 illustrates the Target along with the assigned body axes in $\mathfrak{F}_b$ and the observational points ($n = 1, 2, 3$) added.

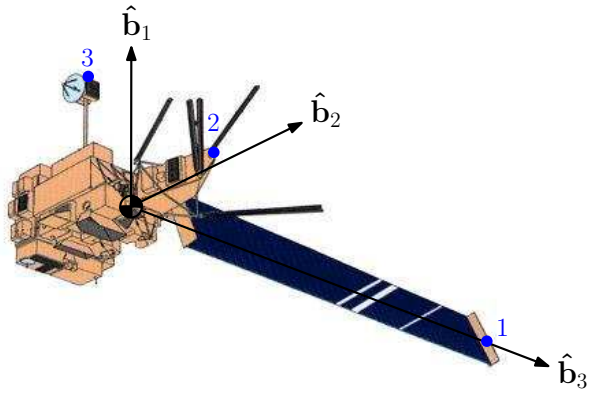

Figure 4.2 Simulated Resident Space Object

With the orbital information, angular velocity information, observation point locations, and the Target geometry illustrated, the states at epoch are now provided. The rotational states of the Target at time t_0 are shown in Table 4.1; for simplicity, the body frame and the orbital frame are aligned at epoch. The relative

Table 4.1 Rotational States of the RSO at Epoch

	$\omega_1\,[rad/s]$	$\omega_2\,[rad/s]$	$\omega_3\,[rad/s]$	$\theta_1\,[rad]$	$\theta_2\,[rad]$	$\theta_3\,[rad]$
A Priori	0.0069	0	0.0017	0	0	0
Truth	0.01	0	0.001	0	0	0

position between the Target and the Observer Spacecraft should be relatively small for a proximity operation. With the example of the RELAVIS LIDAR sensor which has a maximum measurement range of $5\,km$ [12] in mind, the relative motion states are provided in Table 4.2. Although this particular Target would realistically be described as semi-rigid, for the purpose of this thesis and consistent with the deterministic dynamics developed in Chapter 2, the RSO Target is considered a rigid

Table 4.2 Relative Position & Velocity States of the RSO at Epoch

	$\delta x\ [m]$	$\delta y\ [m]$	$\delta z\ [m]$	$\delta \dot{x}\ [m/s]$	$\delta \dot{y}\ [m/s]$	$\delta \dot{z}\ [m/s]$
A Priori	54	55	49	0.01	0.01	0.01
Truth	50	50	50	0.01	0.01	0.01
Error	8%	10%	2%	0%	0%	0%

body for the duration of the observation, having constant moments of inertia shown in Table 4.3. Three trials will be accomplished for the 9-state estimation cases. Each

Table 4.3 Moments of Inertia of RSO

	$A\ [kg\,m^2]$	$B\ [kg\,m^2]$	$C\ [kg\,m^2]$	Error
Trial 1	50.5	33	13.5	10%
Trial 2	54	36	12	20%
Trial 3	58.5	39	10.5	30%
Truth	45	30	15	-

trial will use initial conditions that consistently vary in percent error from the true moment of inertia value.

The tracked observational points used on the Target body, measured from the assumed center-of-mass location, are illustrated in Figure 4.2 and provided in Table 4.4. Since the observation points are not being estimated, no distinction is made between their true location and their approximated location.

Table 4.4 Observational Point Locations on RSO Body

n	$b_{1_n}\ [m]$	$b_{2_n}\ [m]$	$b_{3_n}\ [m]$
1	0	0	20
2	2	6	-1
3	4	-1	-1

With the true initial conditions provided in the tables above, the Truth Model program is executed resulting in the true dynamics model of the Observer-Target system as well as generated data batches for simulated range measurements. The relative position of the Observer with respect to the Target is illustrated in Figure 4.3.

Figure 4.4 depicts the relative motion of the Observer about the Target for one orbital period (of the Target). Figure 4.5 shows the trace that the tracked observational

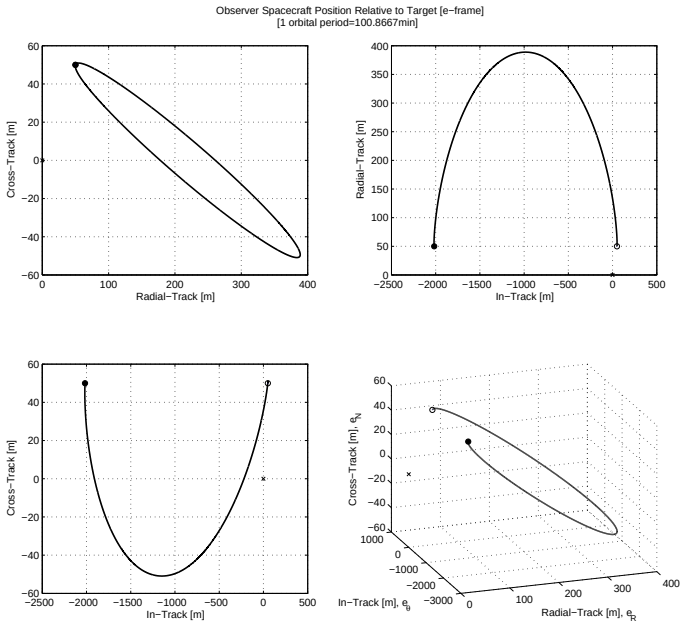

Figure 4.3 Relative Position Multi-View

points make, viewed in $\mathfrak{F}_e$, as the Target body rotates with angular velocities, ω_1 and ω_3, during the span of one orbital period.

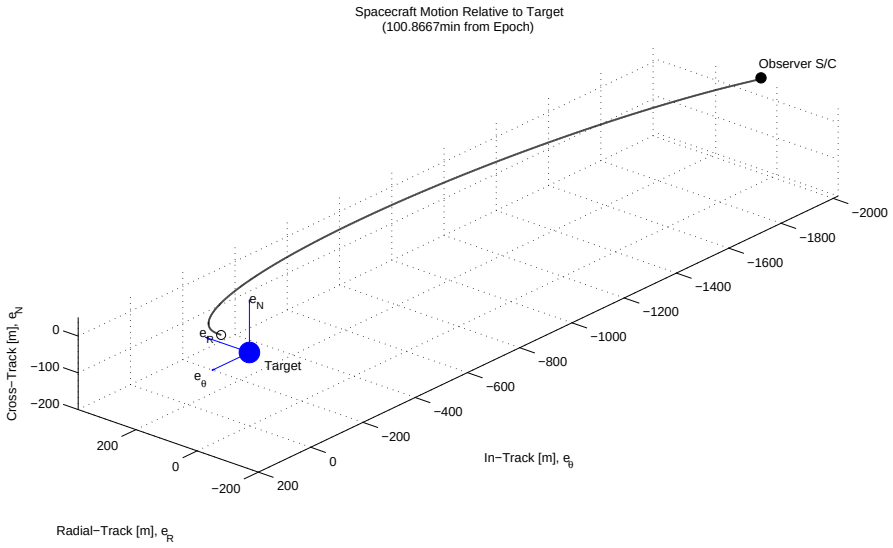

Figure 4.4 Observer Spacecraft & RSO Relative Motion

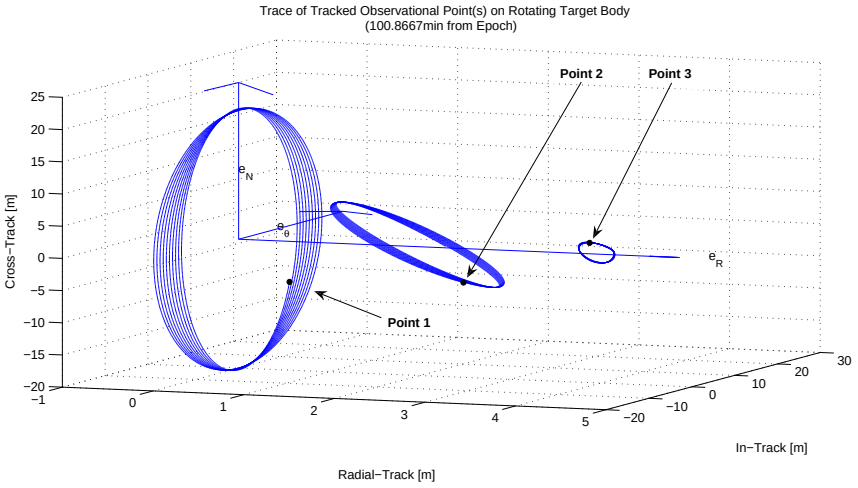

Figure 4.5 Observational Point Trace of RSO Body

4.2 Case I

This case begins with the use of the RSS surface plot method to illustrate the effects of the number of points (i.e. data sets) on local minima and solution ambiguity. Following the RSS analysis and generated best-guess values, one estimation attempt is made using data with no noise. This case involves the following:

- RSS Surface Plot Analysis
- Data Type: Perfect (no noise)
- Number of Observational Points: One for Estimation
- Observational Time Span: $\frac{1}{10}$ Orbital Period of Target
- Estimated States: 12-State Version

4.2.1 RSS Analysis. A method of refining an initial estimate is the use of a residual sum squared surface plot. In the RSS program, the surface plot provides an RSS value as a function of two state variables. The RSS value is essentially a measure of how well the estimate fits the actual data. The two parameter values that provide the minimum RSS value are the initial guess values that should be used in the estimation algorithm.

Consider the that initial estimates for the relative position and velocity states are representative of their true values to some satisfactory level of accuracy. However, also consider that the estimates of the rotational velocities, determined by radar image analysis, is considered a low-confidence estimate. Using the RSS analysis, the low-confidence estimate can be used to develop an estimate that is closer to the actual value. Table 4.1 provides the rough estimates based on the radar image analysis. With the accuracy of the analysis known, the range or bound for the guess is defined. For the purpose of this example, consider that the image analysis values

lead one to believe the true values lie in the following range

$$0.001 < \omega_1(t_0) < 0.02 \qquad \text{and} \qquad -0.0005 < \omega_3(t_0) < 0.05 \tag{4.2}$$

and define ω_1 as parameter 1 and ω_3 as parameter 2. The user's inputs include the *a priori* estimates for relative motion from Table 4.2, the observational points from Table 4.4, and the settings shown in Table 4.5. Since running this program with these

Table 4.5 RSS Guess Generator Boundary Conditions

Parameter	Lower Bound	Upper Bound	No. of Increments
1	0.001	0.020	100
2	-0.0005	0.050	100

settings for all data sets takes approximately eight to ten hours of CPU time, and with memory limitations of the computer used, only one tenth of the total data batch (606 data points) will be used as the sample size for the RSS analysis. This provides an adequate sample for determining the initial conditions of the two parameters for this case. The surface plots and their associated contour plots resulting from the execution of this program are shown in the Figure 4.6.

Figures 4.6a and 4.6b show the computed results of the first RSS solution (Run 1) using observation point number one (i.e. one data batch). Recall that the estimator will strive to minimize the sum of the residuals squared (i.e. the RSS value) by finding a *local* minimum. Within the guess bounds (Equ. 4.2), two distinct local minimums exist as clearly seen in the surface plot. One can see from the contour plot (Fig. 4.6b) that the *a priori* estimates for ω_1 and ω_3 (Table 4.1) lies roughly in between the minimums (the dark regions). This may pose a problem for the estimator, as it may choose the wrong minimum, where the *desired* solution does not lie. Keep in mind the location of the true solution as annotated on the contour figure and given in Table 4.1. The global minimum is determined by the RSS program to be the point where parameter 1 (ω_1) is 0.0050 and parameter 2 (ω_3)

is 0.0102. This can be seen as the region which dips the lowest in surface plot and the other major dark region in the contour plot. However, this is deceivingly the wrong minimum and may very well lead the estimator in the wrong direction to an incorrect solution.

By re-executing the RSS program (Run 2) using observation points one and two (i.e. two independent data batches), the program provides Figures 4.6c and 4.6d. Notice that the global minimum from the first run (Figure 4.6a and 4.6b) is being reduced in depth and that the second local minimum (where the solution actually lies) is now the global minimum in this run.

Run 3 of the RSS program, using a total of three observational points, the program results in the plots seen in Figures 4.6e and 4.6f. Notice that in Figure 4.6e only one major dip (minimum) is seen. From a contour perspective, this is clearly seen in Figure 4.6f, as only one major and defined dark region exists in the location of the true solution. This region is where the program-determined guess lies, which is extremely close to the true location of the solution.

A summary of the results from the three RSS program runs are provided in Table 4.6. The results are shown up to eight decimal digits to illustrate the imperfection. The number of observation points used correspond to the points listed in Table 4.4 starting with $n = 1$. The percent error between the generated guess for ω_1 and ω_3 and the true values (Table 4.1) are also given. By introducing multiple independent batches of data from multiple range observations, the RSS solution is drastically improved.

Table 4.6 RSS Parameter Results

Run No.	Obs Points Used, n	Par. 1 Estimate	Error	Par. 2 Estimate	Error
1	1	0.00503030	50%	0.01021212	921%
2	1,2	0.01040404	4%	0.00256061	156%
3	1,2,3	0.01002020	0.2%	0.00103030	3%

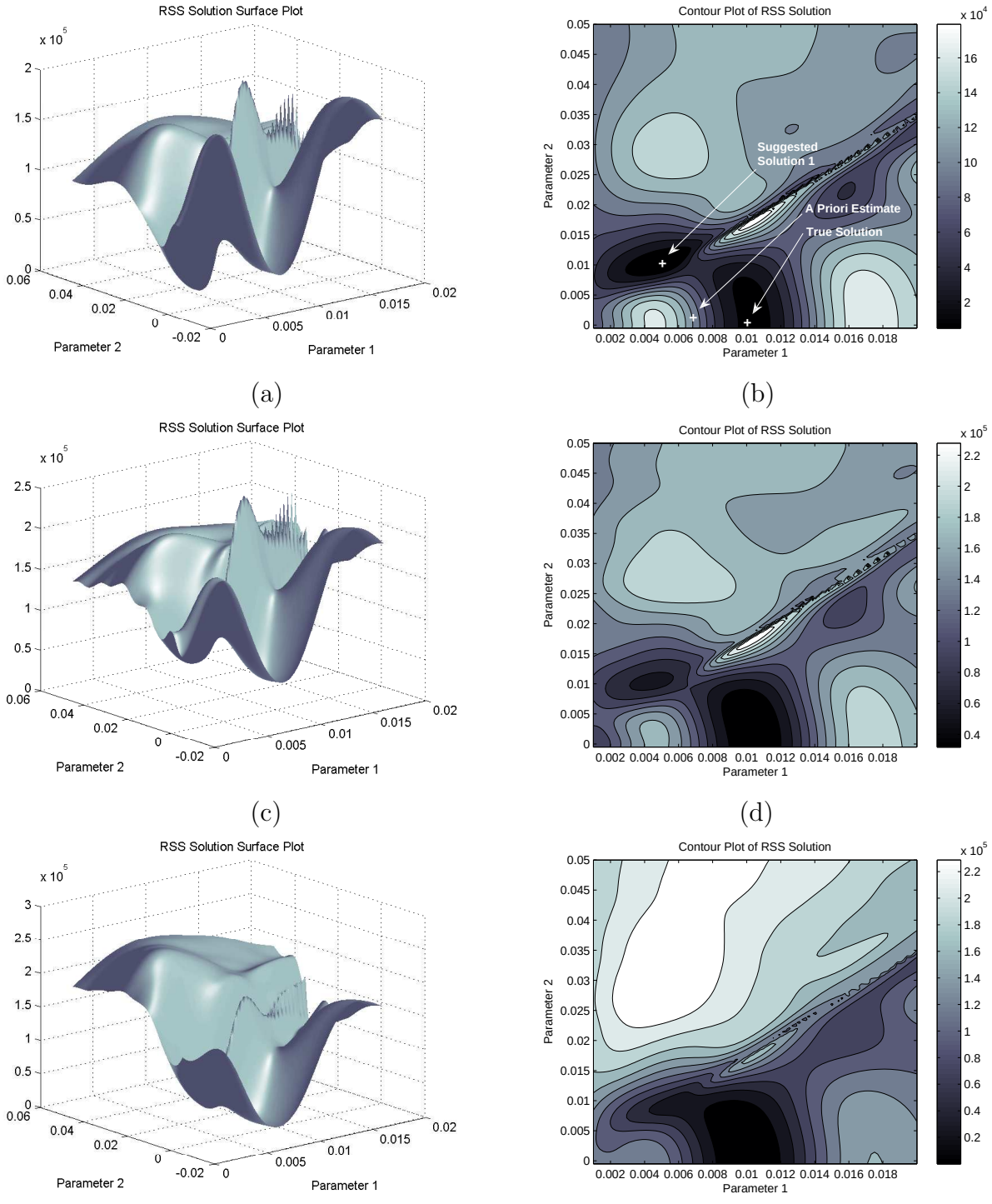

Figure 4.6 RSS Surface & Contour Plots

Theoretically, the program should give a solution for two parameters (state variables) that result in an RSS value of zero, a perfect data fit. However, recall from Chapter 3 that this program is limited to providing a solution to two state variables. In this case because there are 12 total states, 10 of the variables are considered known constants by the RSS program. The imperfect results seen in Table 4.6 are a consequence of imperfect initial values for those other 10 states used in generating this result. The results from this RSS analysis will serve as the initial state estimates for the estimation runs to follow.

The estimation attempt in this case will make use of the results from Run 3. Table 4.7 provides the values used in Case I.

Table 4.7 Case I: Refined Rotational States of the RSO at Epoch

	$\omega_1\ [rad/s]$	$\omega_2\ [rad/s]$	$\omega_3\ [rad/s]$	$\theta_1\ [rad]$	$\theta_2\ [rad]$	$\theta_3\ [rad]$
Case 1A	0.0100	0	0.0010	0	0	0
Truth	0.01	0	0.001	0	0	0

Notice Run 3 of the RSS program (Table 4.6) produced values for ω_1 and ω_3 that are essentially equal to the true state values up to three significant digits. In order to fully make the estimation cases worthwhile and to legitimately test the estimator's performance, values near the true solution but not equal to, are preferred in this study. Therefore, Table 4.8 lists the refined *a priori* initial conditions (from Run 2) used for the Case II and Case III estimations.

Table 4.8 Refined Rotational States at Epoch for Cases II and III

	$\omega_1\ [rad/s]$	$\omega_2\ [rad/s]$	$\omega_3\ [rad/s]$	$\theta_1\ [rad]$	$\theta_2\ [rad]$	$\theta_3\ [rad]$
A Priori	0.0104	0	0.0026	0	0	0
Truth	0.01	0	0.001	0	0	0

4.2.2 Data Batch. The data set processed in this case uses a 606-observation sample of the entire data batch, or one-tenth of the Target's orbital period worth.

This is done only to be consistent with the RSS Analysis, which also used the first 606 measurements. As mentioned, this case will make use of perfect simulated data containing no Gaussian noise. The point number used corresponds to the observational points listed in Table 4.4. Table 4.9 provides a summary of the data set used in this case.

Table 4.9 Case I: Data Batch Summary

Point No. n	Batch Size	Start Time $[s]$	End Time $[s]$	Time Step $[s]$
1	606	0	605	1

4.2.3 Estimation Case 1A. This portion of Case I uses the best-guess solution for ω_1 and ω_3 provided by Run 3 of the RSS surface plot analysis. The initial rotational dynamics states are provided in Table 4.7. Using the initial conditions for relative position and velocity listed in Table 4.2 and observation point number one listed in Table 4.4, the estimator program is executed with the following setting provided in Table 4.10 below. The setting i_{max} represents the user-specified maximum

Table 4.10 Case I: Estimator Settings for 12-State Version

i_{max}	σ_{instr}	k_1	k_2	k_3	$States$	$NumPts$	$NoiseMode$
200	5×10^{-5}	0.25	0.01	0.20	12	1	off

number of iterations allowed before the program automatically terminates, *States* defines the mode (9 or 12) for the estimated state version (Equ. 2.65 or Equ. 2.70), $NumPts$ sets the number of points to be used in the estimation process (i.e. range data batches), and the $NoiseMode$ string simply has the program use the version of the range data containing no noise. Since the data contains no noise, it has a standard deviation of $\sigma_{instr} = 0$. However, to avoid the Q matrix (Equ. 2.97) from becoming singular, $\sigma_{instr} = 0.00005$ is used instead.

The estimator program converged on a solution in 38 iterations. Based on the predicted range measurements, no significant difference exists between the estima-

tor's solution and the actual solution. Table 4.11 compares the true values of the

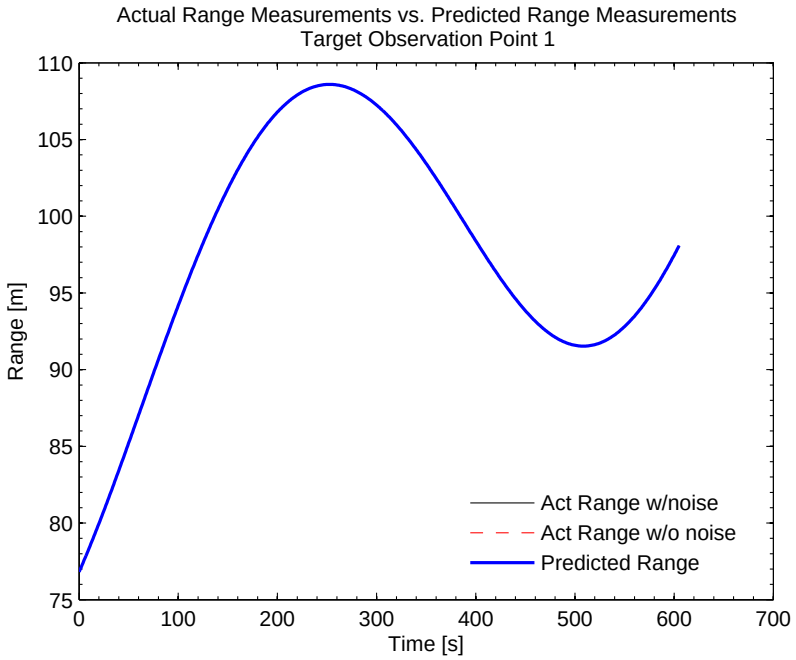

Figure 4.7 Case I: Predicted Range Profile (12-State)

states at epoch and the estimated results for this case. Propagating the estimator's

Table 4.11 Case I: Estimated 12-State Solution at Epoch

State Variable	Estimate, $\bar{\mathbf{X}}(t_0)$	Truth, $\mathbf{X}(t_0)$	Error
$\delta x \quad [m]$	52.16	50	4.3%
$\delta y \quad [m]$	51.84	50	3.7%
$\delta z \quad [m]$	46.42	50	7.2%
$\delta \dot{x} \quad [m/s]$	0.0163	0.01	63%
$\delta \dot{y} \quad [m/s]$	-0.0025	0.01	125%
$\delta \dot{z} \quad [m/s]$	0.0152	0.01	52%
$\omega_1 \quad [rad/s]$	0.0101	0.01	0.0001
$\omega_2 \quad [rad/s]$	0.0001	0	0.0001
$\omega_3 \quad [rad/s]$	0.0010	0.001	0.0001
$\theta_1 \quad [rad]$	-0.1167	0	0.1167
$\theta_2 \quad [rad]$	-0.0224	0	0.0224
$\theta_3 \quad [rad]$	-0.0830	0	0.0830

solution for the states at epoch, results in the dynamics shown for relative position in Figure 4.8. Figure 4.9 illustrates the Euler angles. Additional data is presented

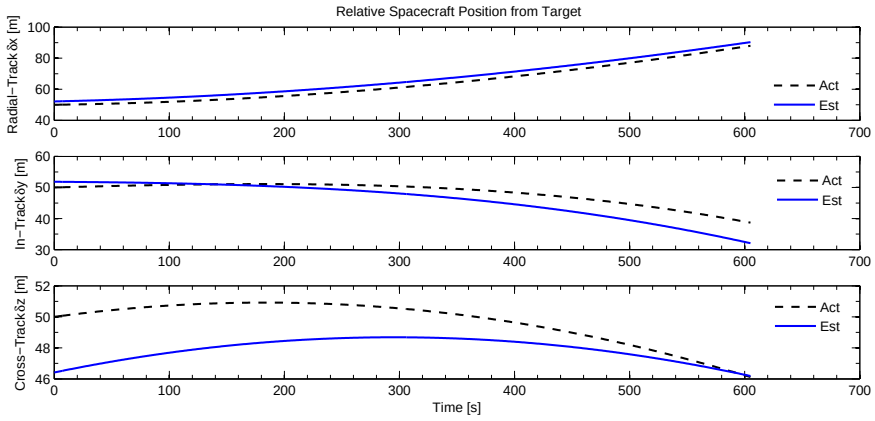

Figure 4.8 Case I: Estimated Relative Position States (12-State)

in Appendix C for this case. It should be mentioned that in this estimation run,

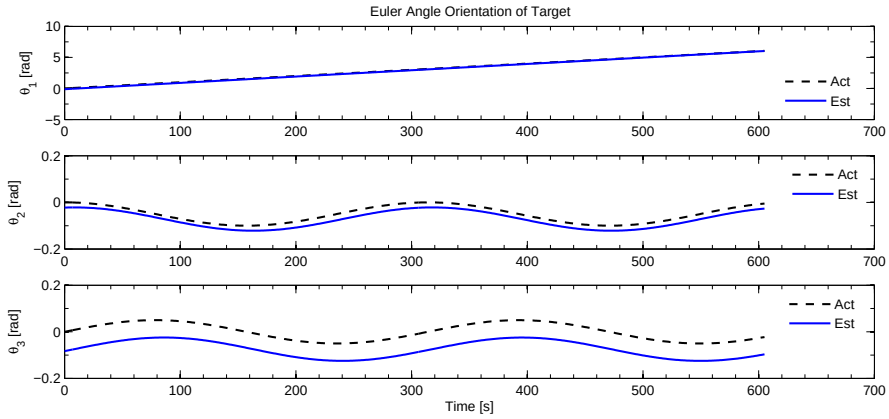

Figure 4.9 Case I: Estimated Euler Orientation Angle States (12-State)

had the σ_{resid} setting been changed to a value closer to machine zero, this run would have failed the standard deviation convergence criterion. This solution is less accurate than ideally desired for a case without noise and relatively accurate initial values. The major error ranging from 52% to 125% is seen in the relative velocity states (Table 4.11). These errors and σ_{resid} are due to the initial conditions of the relative position variables. This estimation run is considered successful and satisfied its purpose to illustrated a run using the RSS analysis results for data processing. Further cases in this research will make use of the entire data batch containing noise.

4.3 Case II

This will be the first case in which the estimation process is applied to simulated data containing Gaussian noise. This case will involve the following:

- Data Type: Noisy (with Gaussian Error)
- Number of Observational Points: One
- Observational Time Span: 1 Orbital Period
- Estimated States: 12-State & 9-State Versions

The objective of this case is to generate an estimated solution using a single tracked observation point (i.e. one range data set) for comparison with Case III involving multiple observation points. Additional data is provided in Appendix C.

4.3.1 Data Batch. The generated data batch that is processed in both portions of this case has 6053 simulated range measurements with a standard deviation listed below. A negligible difference between the standard deviation of the instrument and the actual standard deviation of the data exists. This is simply due to the user's input of σ_{instr} in the Truth Model script and the pseudo-random number algorithm generating data nearly equal with some difference because of the randomness involved. The value of σ_{instr} will be used in estimation process. The point number used corresponds to the observational points listed in Table 4.4.

Table 4.12 Case II: Data Batch Summary

Point No. n	σ_{instr}	σ_{act}	Batch Size	Start Time $[s]$	End Time $[s]$	Time Step $[s]$
1	0.250	0.248	6053	0	6052	1

4.3.2 12-State Estimation. This portion of the case will involve estimating both the relative motion dynamics and the rotational states of the RSO. Recall the

12-state vector defined as,

$$\mathbf{X} = \left[\begin{array}{cccccccccccc} \delta x & \delta y & \delta z & \delta \dot{x} & \delta \dot{y} & \delta \dot{z} & \omega_1 & \omega_2 & \omega_3 & \theta_1 & \theta_2 & \theta_3 \end{array} \right]^T$$

During several initial runs made during the development of the estimator code, it was determined that the program is generally stable and performs the best when $0.01 \leq k_1 \leq 0.50$. In this case, the estimator setting are provided below

Table 4.13 Case II: Estimator Settings for 12-State Version

i_{max}	σ_{instr}	k_1	k_2	k_3	$States$	$NumPts$	$NoiseMode$
200	0.25	0.50	0.05	0.012	12	1	on

With the settings above, the program ran for approximately $4\,hrs$ where it reached the maximum allowed number of iterations *without* convergence to an acceptable solution. The covariance criterion was met; however, the standard deviation criterion was not. The standard deviation of the residuals from the estimation process was approximately $\sigma_{resid} \approx 14$, as seen in Figure 4.15 while the standard deviation of noise error in the data batch is $\sigma_{instr} \approx 0.25$. Therefore, this reference solution remains only a reference solution and is not considered *the* estimated trajectory. The last reference solution, $\mathbf{X}_{ref}(t_0)$, prior to program termination is provided in the Table 4.14 along with the associated percent relative error from the true states. To illustrate what the non-convergent solution resembles, the resulting reference solution at i_{max} is propagated forward in time to the end of the observational period. The relative position and velocity histories are shown in Figures 4.10 and 4.11. Their respective true error as a function of time is shown in Figures C.8 and C.9 in Appendix C. The six rotational dynamical states of the Target are illustrated in Figures 4.12 and 4.13. Their associated true error plots are shown in Figures C.10 and C.11. The overall solution of the reference trajectory resulted in the predicted range observations shown in Figure 4.14 compared with the actual noisy range data set. Notice that the solution results in a predicted range profile

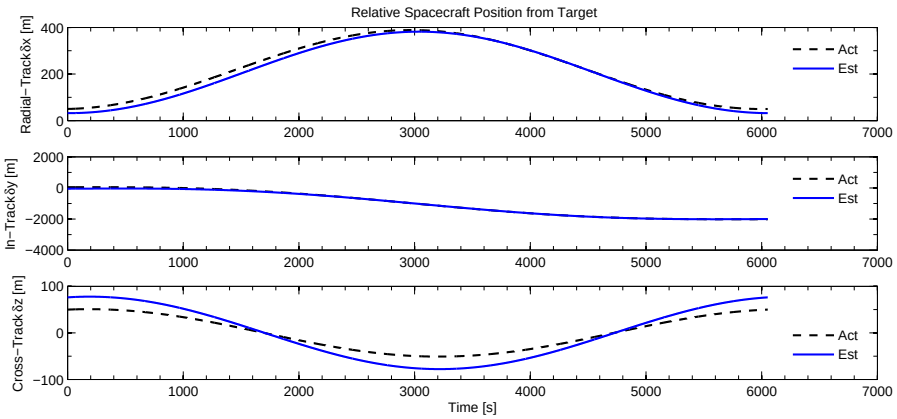

Figure 4.10 Case II: Estimated Relative Position States (12-State)

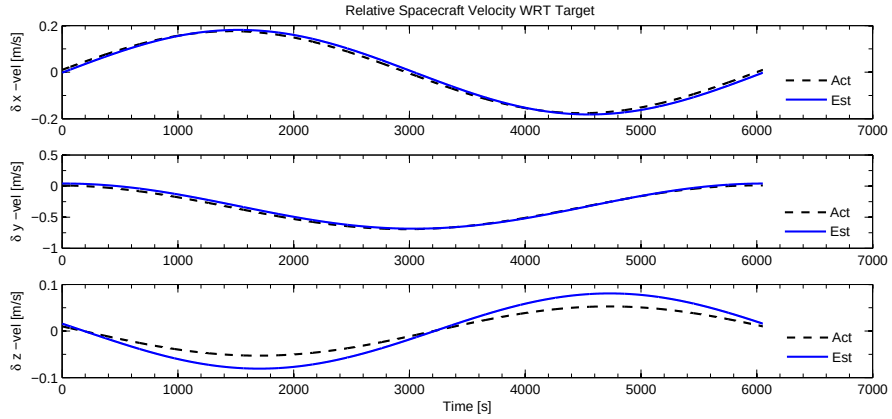

Figure 4.11 Case II: Estimated Relative Velocity States (12-State)

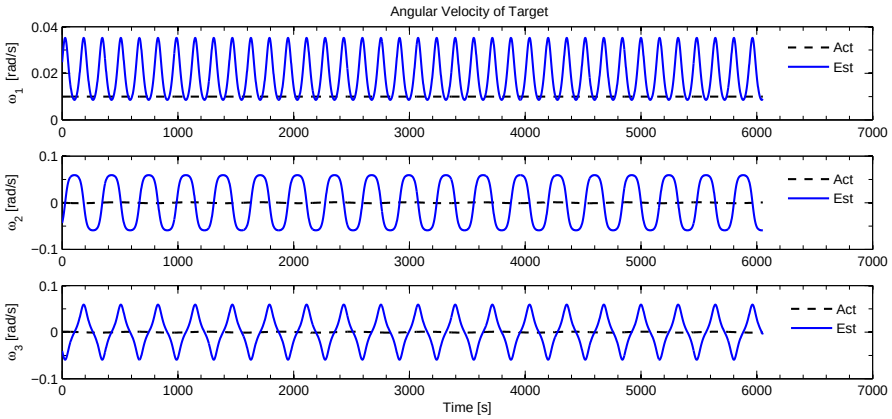

Figure 4.12 Case II: Estimated Angular Velocity States (12-State)

Table 4.14 Case II: Estimated 12-State Results at Epoch

State Variable	Estimate, $\mathbf{X}_{ref}(t_0)$	Truth, $\mathbf{X}(t_0)$	Error
$\delta x \quad [m]$	32.06	50	35.9%
$\delta y \quad [m]$	-52.43	50	204.9%
$\delta z \quad [m]$	76.27	50	52.5%
$\delta \dot{x} \quad [m/s]$	-0.0022	0.01	122%
$\delta \dot{y} \quad [m/s]$	0.0409	0.01	309%
$\delta \dot{z} \quad [m/s]$	0.0159	0.01	59%
$\omega_1 \quad [rad/s]$	0.0248	0.01	0.0148
$\omega_2 \quad [rad/s]$	-0.0434	0	0.0434
$\omega_3 \quad [rad/s]$	-0.0402	0.001	0.0392
$\theta_1 \quad [rad]$	4.7289	0	4.7289
$\theta_2 \quad [rad]$	0.9465	0	0.9465
$\theta_3 \quad [rad]$	8.5974	0	8.5974

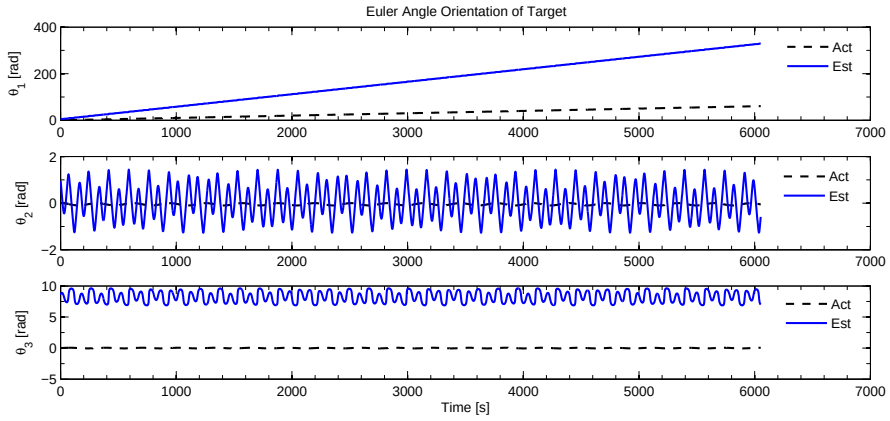

Figure 4.13 Case II: Estimated Euler Orientation Angle States (12-State)

that does generally resemble the true range observations. The true range profile is more nonlinear than it appears in Figure 4.14 simply because of the plot scale. The estimated solution fits the middle portion without much trouble; however, the most nonlinear regions, located approximately from $0 - 2000\,s$ and $4000 - 6050\,s$, posed the greatest difficulty for the estimator in this case. The distribution of the residuals between the predicted range observations and the actual observations provides a means to judge the quality of the solution. Since the noise or error of the simulated measurements is Gaussian in nature (by creation), the residuals of the predicted

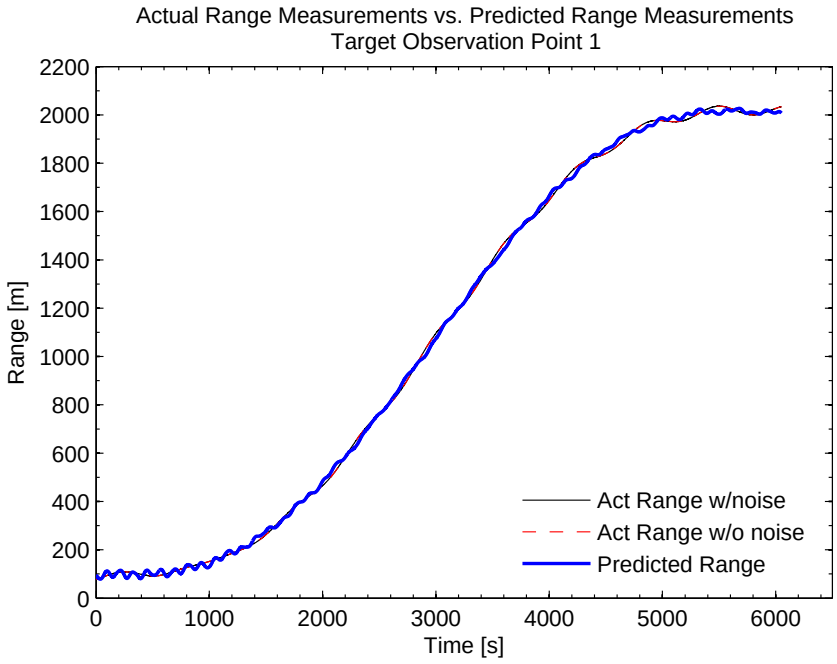

Figure 4.14 Case II: Predicted Range Profile (12-State)

observations should also resemble a Gaussian distribution with a similar standard deviation. However, in this case $\sigma_{resid} \neq \sigma_{instr}$, which is why the convergence criteria failed. With the k_3 setting defined in Table 4.13, the standard deviation criterion required σ_{resid} to fall in the range of $0.247 \leq \sigma_{resid} \leq 0.253$.

Figure 4.15a depicts a residual distribution that loosely resembles a distorted Gaussian curve centered on zero, but with a standard deviation of approximately 14 meters. In Figure 4.15b the distribution of range residuals as a function of observation time is shown to have a desirable mean near zero, as mentioned; however, the spread of residuals is not characteristic of a true normal distribution. From iteration 28 to 200, the standard deviation of the residuals remained at $\sigma_{resid} \approx 14.042$. It would appear that the estimator reached a local minimum indicated by this apparent limit of the standard deviation. This will be discussed further in the last section of this chapter. The covariance criterion was satisfied at iteration 55 till program

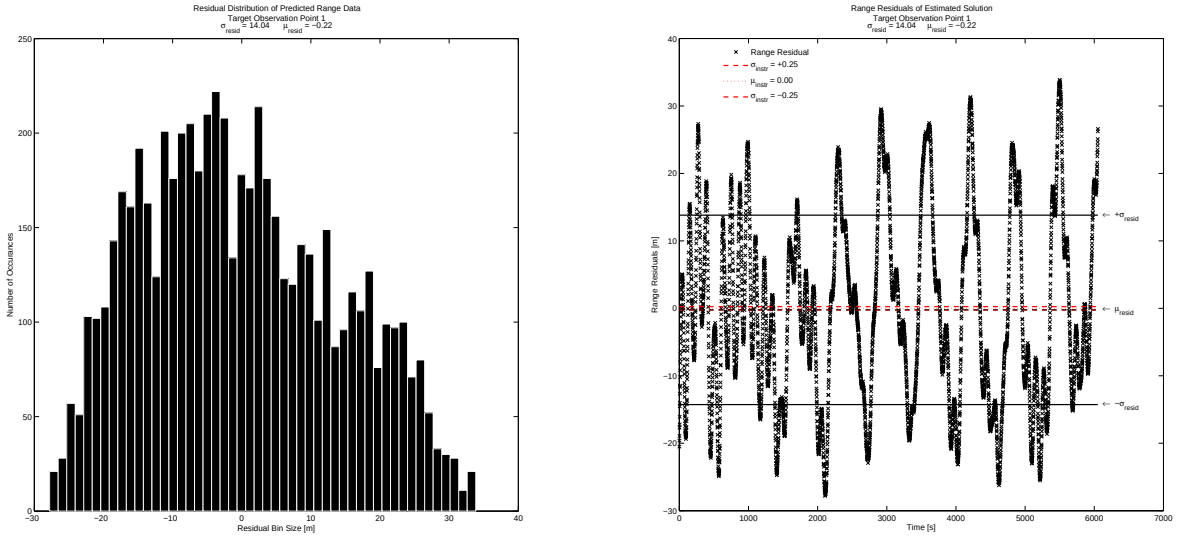

(a) (b)

Figure 4.15 Case II: Residual Distribution for Point No. 1 (12-State)

termination. This estimation attempt, that did not converge in 200 or less iterations with the given filter settings, is considered a *failed* attempt.

4.3.3 9-State Estimation. This portion of Case II will attempt to estimate the rotational states as well as the moments of inertia of the Target. To further explore the ability to estimate the moments of inertia, three trials will be undertaken. Recall the 9-state vector is given as

$$\mathbf{X} = \begin{bmatrix} \omega_1 & \omega_2 & \omega_3 & \theta_1 & \theta_2 & \theta_3 & A & B & C \end{bmatrix}^T$$

The estimator settings for this run are shown in Table 4.15. This case will make

Table 4.15 Case II: Estimator Settings for 9-State Version

i_{max}	σ_{instr}	k_1	k_2	k_3	$States$	$NumPts$	$NoiseMode$
200	0.25	0.50	0.10	0.012	9	1	on

use of the same range data batch from the same single observation point used in the 12-state run. The *a priori* initial estimates for the rotational states are listed

in Table 4.8. Unlike the 12-State portion, this 9-State version of this process will be completed for three trials using the initial conditions listed in Table 4.3 for the moments of inertia. Note that each trial increases the relative error between the initial guess and the true value of the MOI. After running the estimator program for each trial, keeping all initial states besides the moments of inertia the same, results in the following shown in Table 4.16 In this case, all trials satisfied the convergence

Table 4.16 Case II: Estimated 9-State Results at Epoch

Variable	Estimates			Truth
	Trial 1 [10% MOI Error]	*Trial 2* [20% MOI Error]	*Trial 3* [30% MOI Error]	
ω_1 $[rad/s]$	0.0100	0.0100	0.0100	0.01
ω_2 $[rad/s]$	0.0000	0.0000	0.0000	0
ω_3 $[rad/s]$	0.0000	0.0000	0.0000	0.001
θ_1 $[rad]$	0.0002	0.0004	0.0007	0
θ_2 $[rad]$	0.0013	0.0015	0.0000	0
θ_3 $[rad]$	0.0020	0.0015	0.0014	0
A $[m^2kg]$	50.76	53.91	58.54	45
B $[m^2kg]$	32.73	36.10	38.96	30
C $[m^2kg]$	13.19	12.12	10.43	15
σ_{resid} $[m]$	0.249	0.249	0.249	0.247
iterations	9	8	8	-
processing time [s]	98	100	120	-

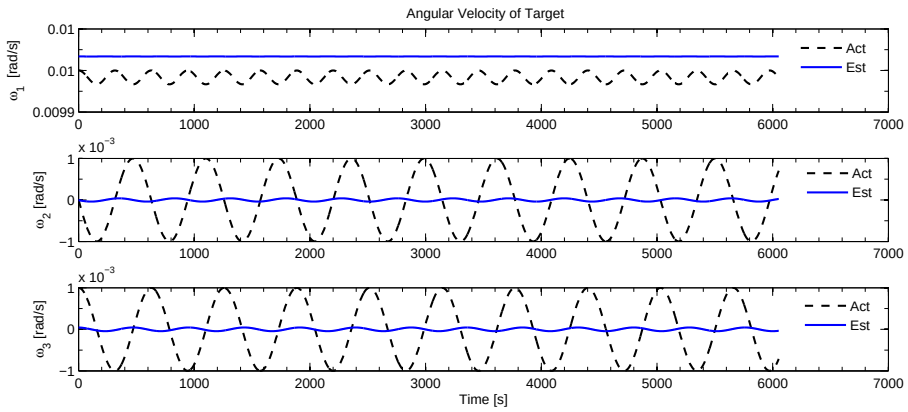

Figure 4.16 Case II: Estimated Angular Velocity States (9-State)

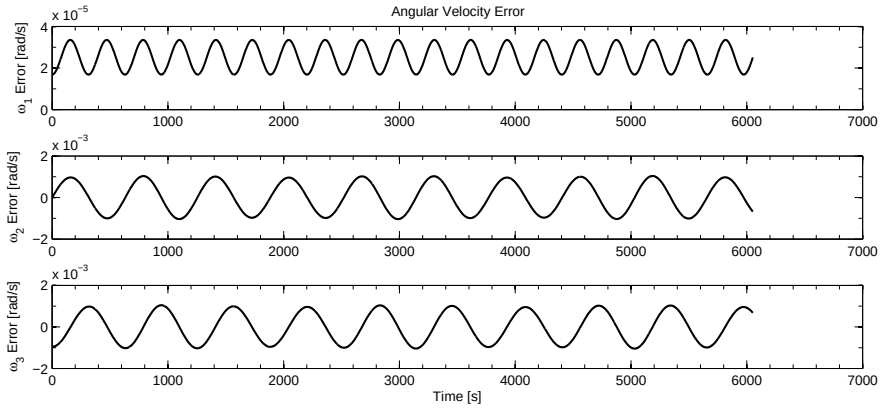

Figure 4.17 Case II: True Error of Estimated Angular Velocities (9-State)

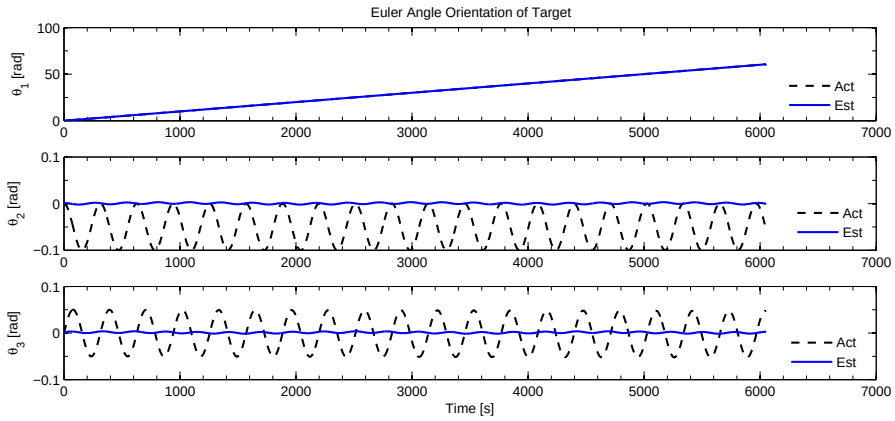

Figure 4.18 Case II: Estimated Euler Orientation Angle States (9-State)

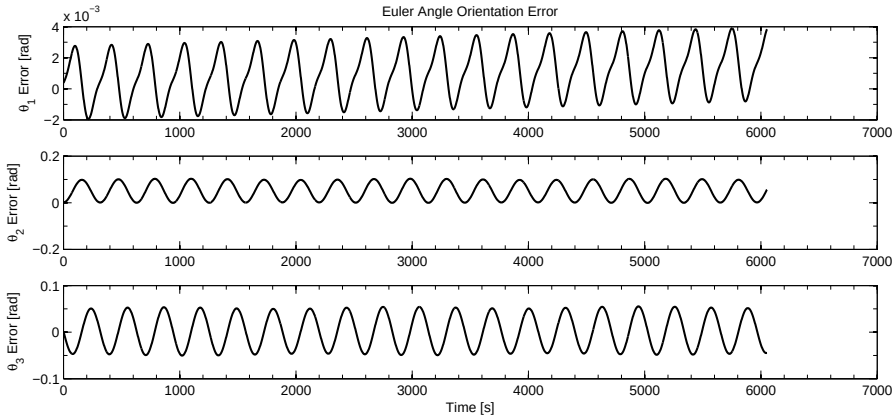

Figure 4.19 Case II: True Error of Estimated Euler Orientation Angles (9-State)

Table 4.17 Case II: Percent Error of 9-State Estimates

Variable	Error of Estimates		
	Trial 1 [10% MOI Error]	*Trial 2* [20% MOI Error]	*Trial 3* [30% MOI Error]
ω_1 $[rad/s]$	0	0	0
ω_2 $[rad/s]$	0	0	0
ω_3 $[rad/s]$	0.001	0.001	0.001
θ_1 $[rad]$	0.0002	0.0004	0.0007
θ_2 $[rad]$	0.0013	0.0015	0
θ_3 $[rad]$	0.0020	0.0015	0.0014
A	12.8%	19.8%	30.1%
B	9.1%	20.3%	29.9%
C	12.1%	19.2%	30.5%
σ_{resid}	0.8%	0.8%	0.8%

criteria. Propagating the estimated solution for Trial 2 forward in time, yields the following results. Using the Trial 2 solution as an example, the predicted range measurements are shown in Figure 4.20. To illustrate that the predicted range is truly a perfect fit to the actual data set and well within the noise, Figure C.12 provides a zoomed in caption of the range profile in the region of $5740-6050\,s$. The distribution of the residuals is provided in Figure 4.21. The histogram (Fig. 4.21a) shows the estimation residuals having a Gaussian distribution comparable to the distribution of the induced measurement error in the data set (e.g. Fig. 3.3). Figure 4.21b illustrates the distribution of the residuals as a function of time with σ_{resid} annotated. This is characteristic of the added Gaussian noise (e.g. Fig. 3.4). This 9-state estimation run is considered a success using only one data set in the estimation process. The only area of concern is that the solution indicates one axis of rotation. This will be discussed in a later section.

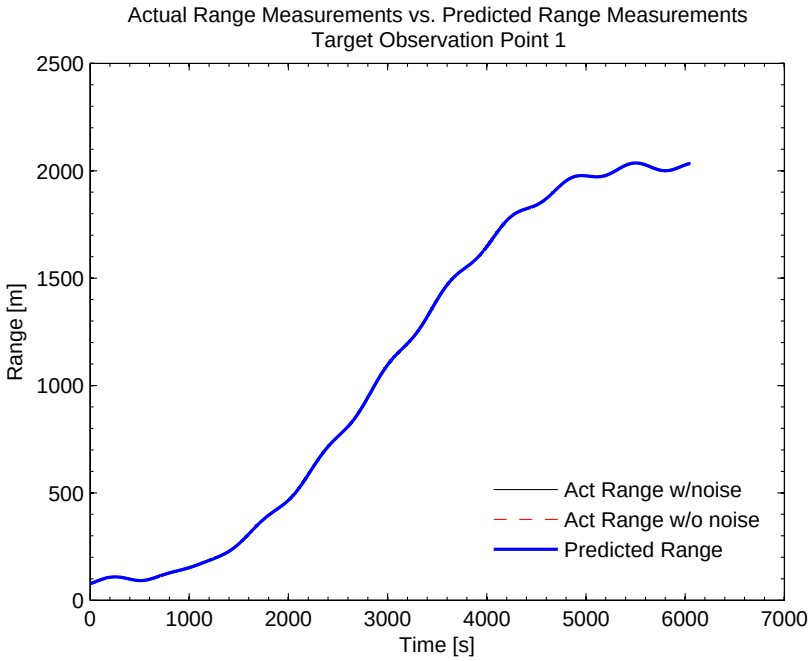

Figure 4.20 Case II: Predicted Range Profile (9-State)

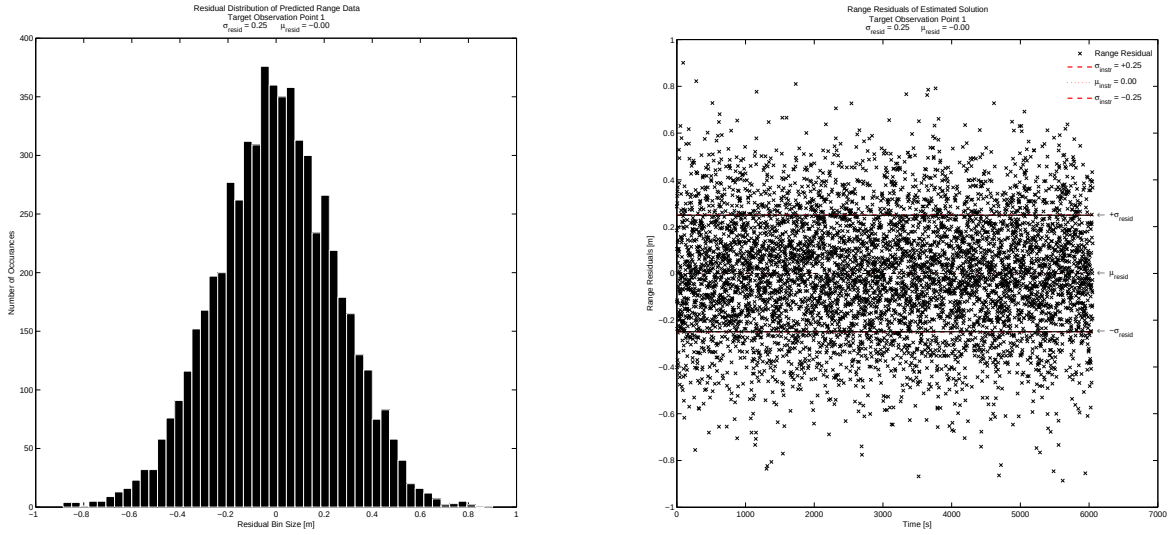

(a) (b)

Figure 4.21 Case II: Residual Distribution for Point No. 1 (9-State)

4.4 Case III

The 12 and 9 state portions of this case will examine the results of the estimation process using two data sets from the observation of two points on the Target body instead of just one. Specifically, this case will involve the following:

- Data Type: Noisy (with Gaussian Error)
- Number of Observational Points: Two
- Observational Time Span: 1 Orbital Period
- Estimated States: 12-State & 9-State Versions

The objective of this case is to determine if processing two data batches (from two observation points) affects the estimated solution versus the solution formed from processing a single data batch. This will be applied to both versions of the state vector. Additional data is provided in Appendix C.

4.4.1 Data Batch. Two data batches are processed in this case. The first data batch associated with observation point 1 is the same data set used in Case II. The second data set used is associated with observation point 2, as listed in Table 4.4. Table 4.18 provides the specifics for the data sets used in this case.

Table 4.18 Case III: Data Batch Summary

Point No. n	σ_{instr}	σ_{act}	Batch Size	Start Time $[s]$	End Time $[s]$	Time Step $[s]$
1	0.250	0.248	6053	0	6052	1
2	0.250	0.247	6053	0	6052	1

4.4.2 12-State Estimation. This portion of the case will involve estimating both the relative motion dynamics and the rotational states of the RSO using two sets of data. The estimator setting are provided Table 4.19.

Table 4.19 Case III: Estimator Settings for 12-State Version

i_{max}	σ_{instr}	k_1	k_2	k_3	$States$	$NumPts$	$NoiseMode$
200	0.25	0.50	0.05	0.012	12	1	on

The program ran for approximately $100\,s$ where it met both the covariance and standard deviation criteria and converged to a solution in 13 iterations. Table 4.20 lists the results of the estimated solution for the 12 states at epoch.

Table 4.20 Case III: Estimated 12-State Results at Epoch

State Variable	Estimate, $\bar{\mathbf{X}}(t_0)$	Truth, $\mathbf{X}(t_0)$	Error
$\delta x \quad [m]$	50.01	50	0.02%
$\delta y \quad [m]$	50.04	50	0.08%
$\delta z \quad [m]$	49.95	50	0.1%
$\delta \dot{x} \quad [m/s]$	0.0100	0.01	0
$\delta \dot{y} \quad [m/s]$	0.0100	0.01	0
$\delta \dot{z} \quad [m/s]$	0.0100	0.01	0
$\omega_1 \quad [rad/s]$	0.0100	0.01	0
$\omega_2 \quad [rad/s]$	0.0000	0	0
$\omega_3 \quad [rad/s]$	0.0010	0.001	0
$\theta_1 \quad [rad]$	-0.0006	0	0.0006
$\theta_2 \quad [rad]$	0.0004	0	0.0004
$\theta_3 \quad [rad]$	0.0018	0	0.0008
$\sigma_{resid_{n=1}} \quad [m]$	0.249	0.248	0.4%
$\sigma_{resid_{n=2}} \quad [m]$	0.251	0.247	1.6%

The estimated states at epoch propagated forward in time to the end of the observational period results in Figures 4.22 and 4.23, along with their true error plots for relative motion shown in Appendix C. The rotational dynamics from the estimated solution are shown in Figures 4.24 and 4.25. Applying the observation function with the estimated dynamics results in the predicted range observations for each observational point shown in Figure 4.26. The residuals from the predicted range observation and the actual range measurements have a distribution illustrated in Figures 4.27 and 4.28 for each data batch.

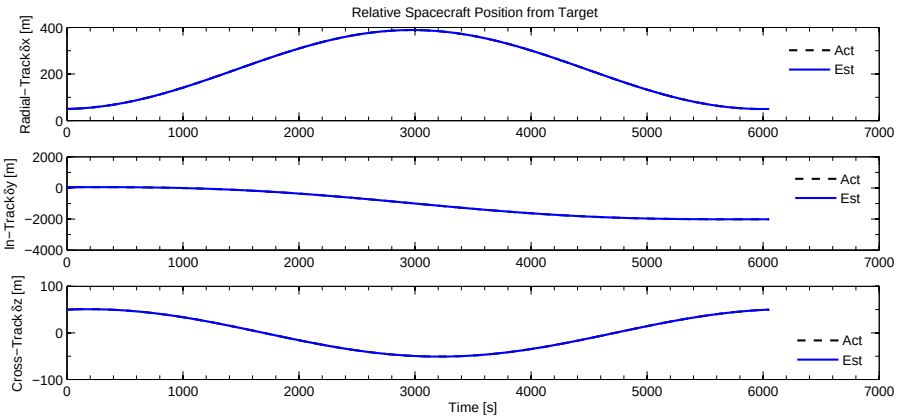

Figure 4.22 Case III: Estimated Relative Position States (12-State)

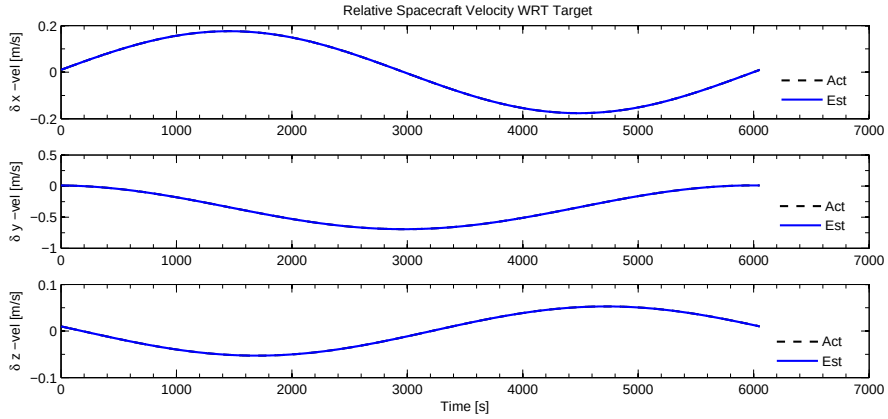

Figure 4.23 Case III: Estimated Relative Velocity States (12-State)

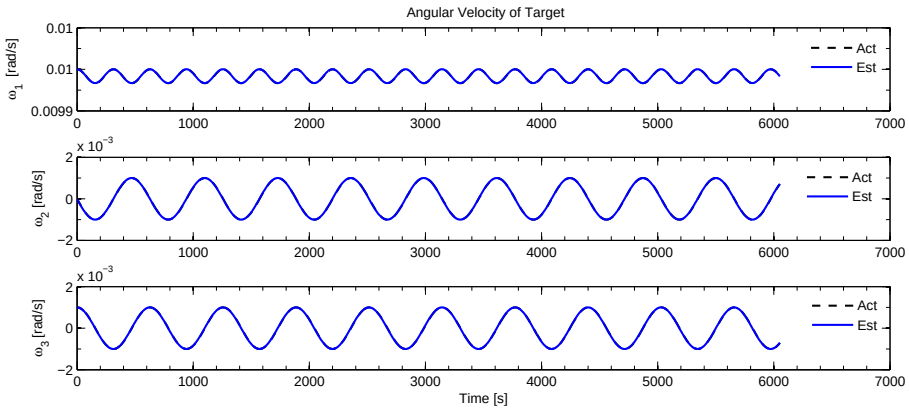

Figure 4.24 Case III: Estimated Angular Velocity States (12-State)

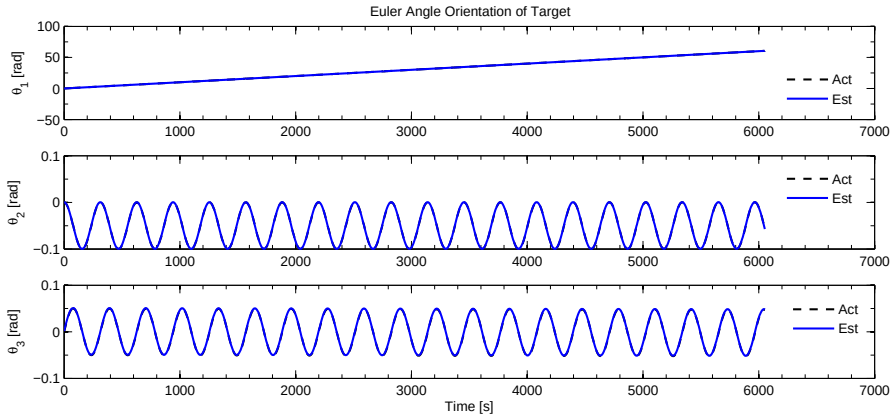

Figure 4.25 Case III: Estimated Euler Orientation Angle States (12-State)

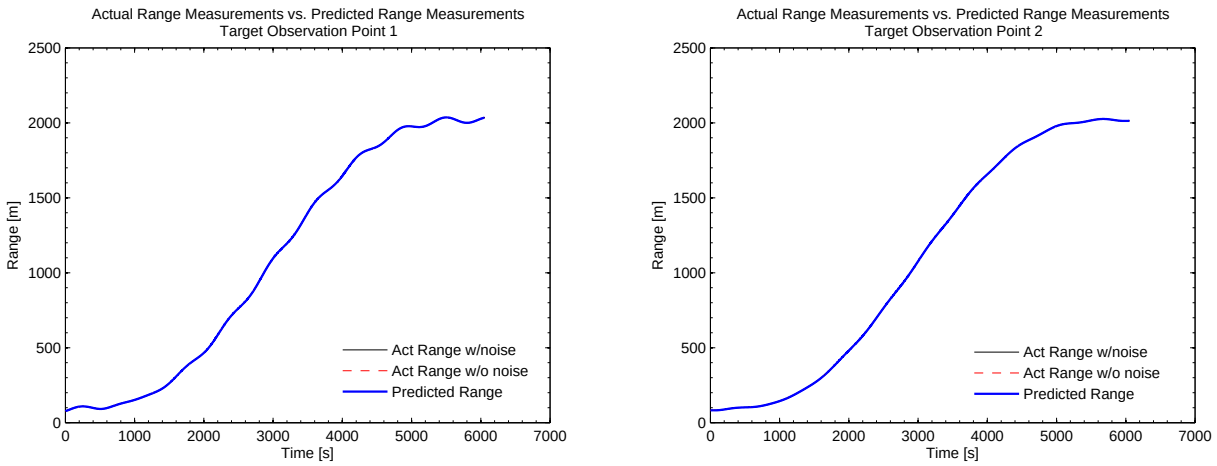

(a) (b)

Figure 4.26 Case III: Predicted Range Profiles (12-State)

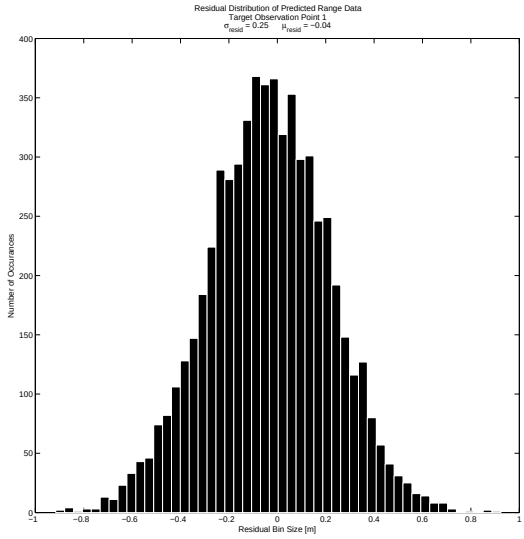

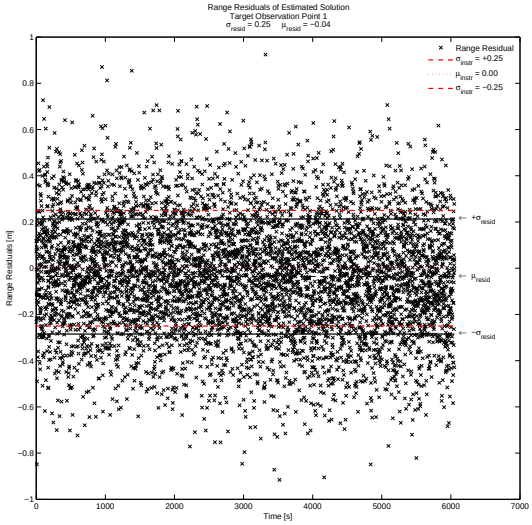

(a) (b)

Figure 4.27 Case III: Residual Distribution for Point No. 1 (12-State)

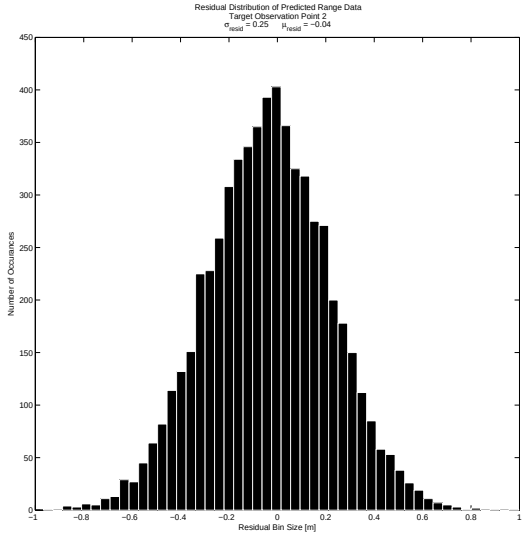

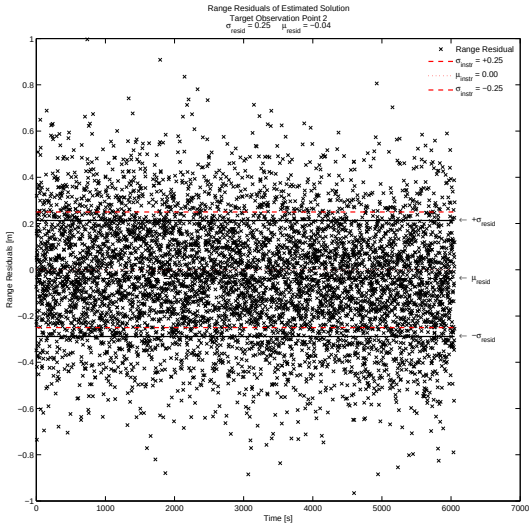

(a) (b)

Figure 4.28 Case III: Residual Distribution for Point No. 2 (12-State)

4.4.3 9-State Estimation. This portion of Case III will attempt to form an estimated solution of the rotational states as well as the moments of inertia of the Target using two data batches from two observation points. This section will also perform three trials of the estimation process for comparison with Case II. The estimator settings for this run are shown in Table 4.21. This case will use the same

Table 4.21 Case III: Estimator Settings for 9-State Version

i_{max}	σ_{instr}	k_1	k_2	k_3	$States$	$NumPts$	$NoiseMode$
200	0.25	0.50	0.10	0.012	9	1	on

data batch from the previous 12-state run. As mentioned, this case will process two data sets, one of which is the same data batch used in Case II. The *a priori* initial states for the angular velocities and the Euler angles are listed in Table 4.8. The the three trials are once again accomplished as listed in Table 4.3. Running the nonlinear least squares estimator program for each trial, resulted in the data presented in Table C.1

Table 4.22 Case III: Estimated 9-State Results at Epoch

Variable	Estimates			Truth
	Trial 1 [10% MOI Error]	*Trial 2* [20% MOI Error]	*Trial 3* [30% MOI Error]	
ω_1 $[rad/s]$	0.0100	0.0100	0.0100	0.01
ω_2 $[rad/s]$	0.0000	0.0000	0.0000	0
ω_3 $[rad/s]$	0.0010	0.0010	0.0000	.001
θ_1 $[rad]$	0.0001	0.0012	0.0004	0
θ_2 $[rad]$	-0.0003	0.0002	-0.0079	0
θ_3 $[rad]$	0.0009	-0.0023	-0.0008	0
A $[m^2kg]$	46.96	52.92	58.21	45
B $[m^2kg]$	38.66	35.60	39.90	30
C $[m^2kg]$	8.28	17.30	9.25	15
$\sigma_{resid_{n=1}}$ $[m]$	0.249	0.252	0.256	0.248
$\sigma_{resid_{n=2}}$ $[m]$	0.249	0.248	0.326	0.247
iterations	18	21	200	-
processing time [s]	213	268	2871	-

Table 4.23 Case III: Percent Error of 9-State Estimation Results

Variable	Percent Error of Estimates		
	Trial 1 [10% MOI Error]	*Trial 2* [20% MOI Error]	*Trial 3* [30% MOI Error]
ω_1 $[rad/s]$	0	0	0
ω_2 $[rad/s]$	0	0	0
ω_3 $[rad/s]$	0	0	0.0010
θ_1 $[rad]$	0.0001	0.0012	0.0004
θ_2 $[rad]$	0.0003	0.0002	0.0079
θ_3 $[rad]$	0.0009	0.0023	0.0008
A $[m^2kg]$	4.4%	17.6%	29.4%
B $[m^2kg]$	28.9%	18.7%	33%
C $[m^2kg]$	44.8%	15.3%	38.3%
$\sigma_{resid_{n=1}}$	0.4%	1.6%	3.2%
$\sigma_{resid_{n=2}}$	0.8%	0.4%	32%

Using the Trial 2 estimated solution, the rotational dynamics is shown in Figures 4.29 and 4.31, along with their associated true error as a function of time.

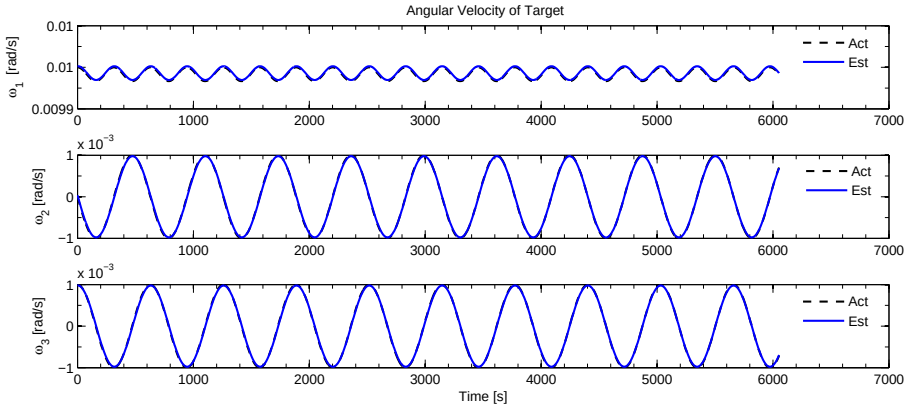

Figure 4.29 Case III: Estimated Angular Velocity States (9-State)

The estimated dynamics results in a predicted range measurement for each observational point shown in Figure 4.33. The associated residuals are illustrated in the Gaussian curves shown in Figure 4.34 and Figure 4.35. The estimation residuals and the measurement error satisfied the condition $\sigma_{resid} \approx \sigma_{instr}$.

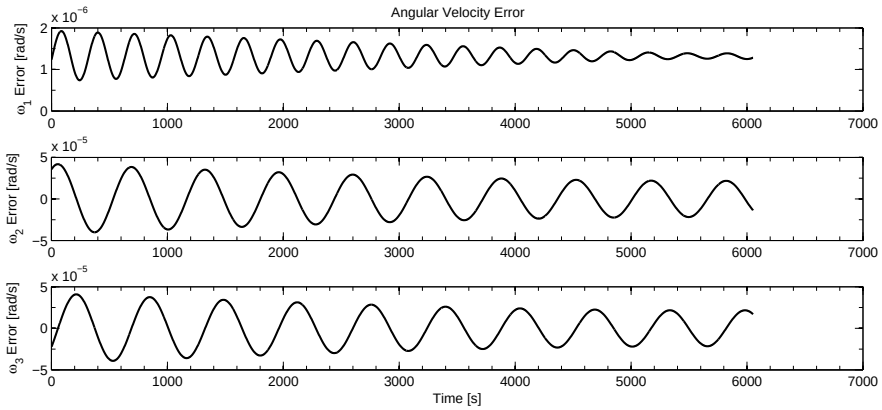

Figure 4.30 Case III: True Error of Estimated Angular Velocities (9-State)

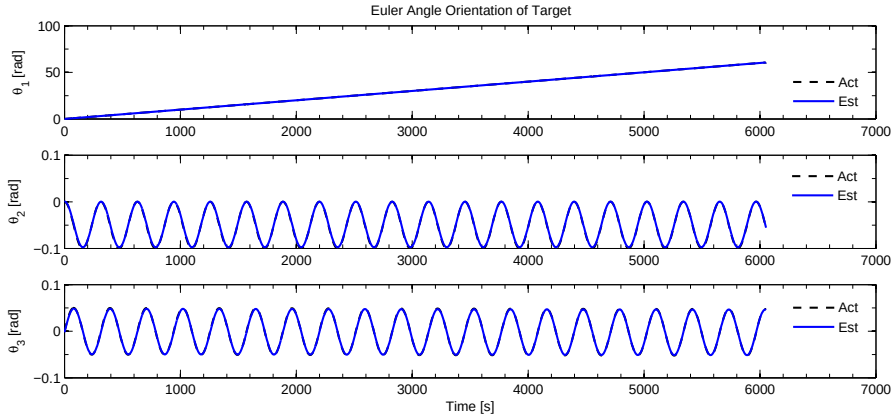

Figure 4.31 Case III: Estimated Euler Orientation Angle States (9-State)

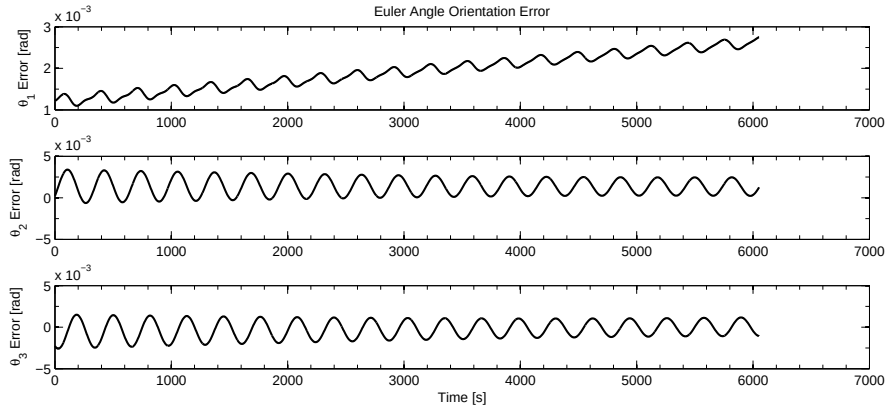

Figure 4.32 Case III: True Error of Estimated Euler Orientation Angles (9-State)

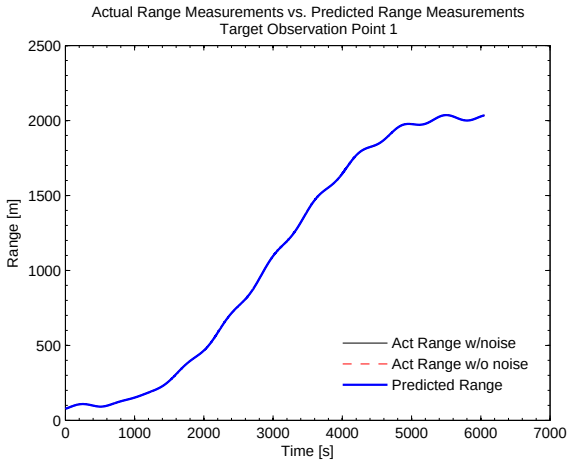

(a)

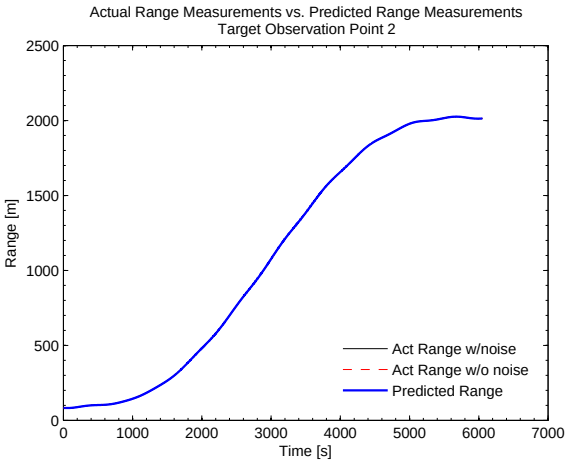

(b)

Figure 4.33 Case III: Predicted Range Profiles (9-State)

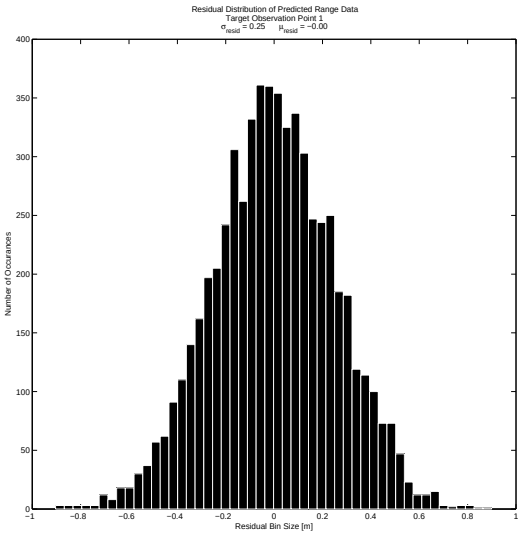

(a)

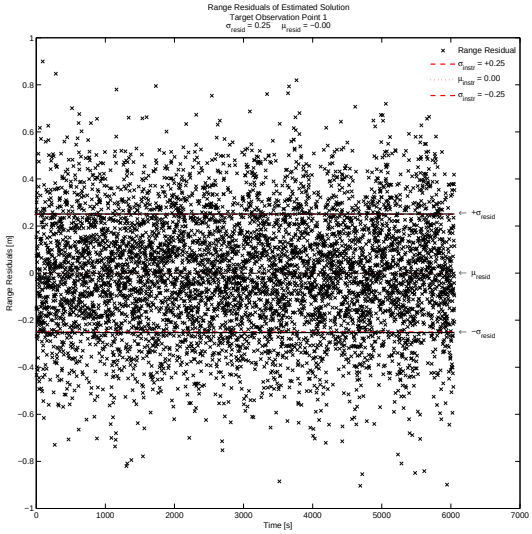

(b)

Figure 4.34 Case III: Residual Distribution for Point No. 1 (9-State)

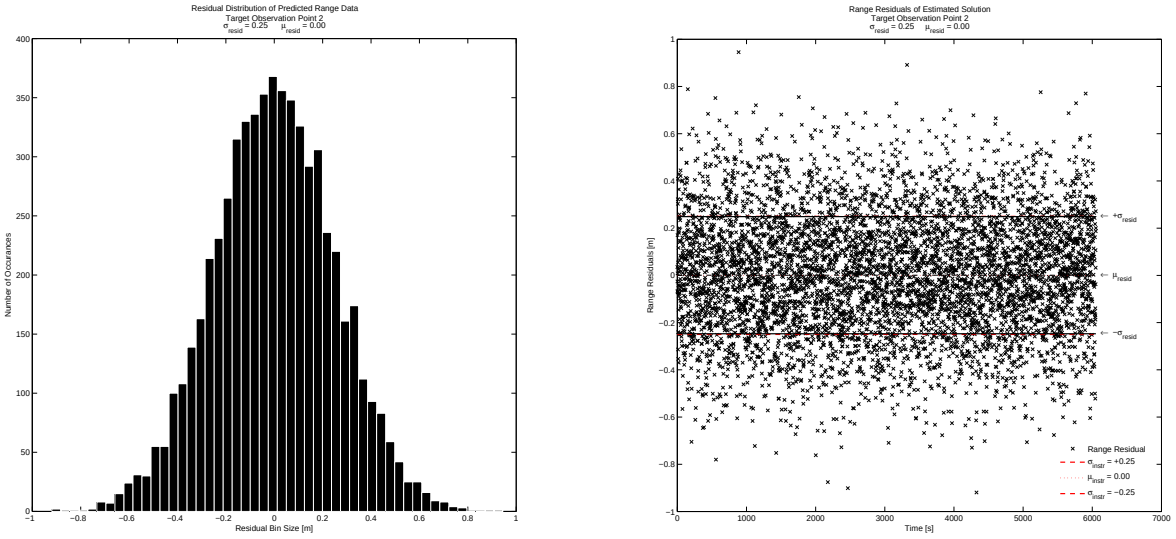

(a) (b)

Figure 4.35 Case III: Residual Distribution for Point No. 2 (9-State)

4.5 Discussion

With the results of the simulation and estimation cases presented, this section will provide a comprehensive discussion of the results through the comparison of solution error and estimator performance parameters.

4.5.1 Case I. The RSS surface and contour plots clearly show how introducing multiple data batches reduces the number of overall solutions that satisfy the observation relation (Equ. 3.11). Recall that Equ. 3.11 has three squared terms, which allows for multiple solutions to exist. Table 4.6 shows that for one data set the error between the estimated and true solutions for parameters 1 and 2 is 50% and 921%, respectively. By processing three data sets, the RSS analysis yields solutions for the two parameters with an error of 0.2% and 3%, respectively. With the drastic improvement, a sample estimation case (Case IA) is attempted using the most accurate RSS result. This estimation case converged and is therefore, considered a success. However, with no noise and with a near-perfect guess for the nonlinear dynamics, one would have expected a nearly perfect estimate with a distribution of

residuals closer to zero. This was not the outcome. In fact, had σ_{instr} been set to a value closer to machine zero, the standard deviation criterion would have failed. This was discovered by allowing the estimator to continue its iterations past convergence where σ_{resid} remained practically constant at 5.77835×10^{-5} from iteration 56 to 200. Several other attempts were made using different values for k_1 with no significant change in the outcome. It appears the estimator reached a limit of some type preventing any improvement of the estimated solution. This limit seen in the standard deviation remaining nearly constant for 144 iterations is most likely due to the estimator finding a local minimum on a nearly level surface closely shared with the desired solution. By adjusting the initial conditions of the relative position states at epoch to values closer to the truth quickly resolved this problem. Case IA simply shows the sensitivity of the estimator and the outcome based solely on the *a priori* values used to start the estimation process.

4.5.2 Case II. Case II (12-State), which used a significantly larger data set (6053 measurements), proved to be a failed estimation attempt without convergence. As mentioned in the results, σ_{resid} remained at 14.042 meters from iteration 28 to 200. The result of this can be seen in the radical rotational dynamics behavior. From Figure 4.13, it appears that the singularity in the Euler angles is contributing to the uncharacteristic rotational dynamics based on the incorrect reference solution at epoch. The existence of multiple solutions is a valid concern here as it was with Case IA, where an accuracy limit was reached by the estimator. The noisy data simply introduces more difficulty for the estimator. In this case, the incorrect reference solution is caught by the convergence criteria; specifically, the distribution of the residuals. The 9-State portion of Case II illustrated the multi-solution problem quite well. All three trials quickly converged to a solution in 8 to 9 iterations in under 120 seconds with $\sigma_{resid} \approx \sigma_{instr}$. However, the difference is best seen in the nonlinear rotational dynamics. The rotational equations of motion are nonlinear and are extremely sensitive to the initial conditions. This is illustrated in the figures

propagating the dynamics. The estimation would lead one to believe that the RSO is in a single-axis spin. The error in the estimated MOI values are clearly related to the error of the *a priori* initial estimates. This highlights the known fact in estimation, that the *better* the initial guess, the *better* the estimate.

4.5.3 Case III. By introducing a second data batch to the estimation process for Case III (12-State), the estimation results radically improved. Using the same number of data points per noisy data set as in Case II, the results of this case far exceed that of Case 1A and certainly Case II (12-State) in terms of accuracy. In 100 seconds and 13 iterations convergence was reached resulting in an estimated solution with σ_{resid} within 0.4% of σ_{instr} for the first data set and 1.6% for the second data set. In the 9-State estimation runs, trials one and two successfully converged in 18 and 21 iterations, respectively and required 213 seconds and 268 seconds of processing time, respectively. The rotational dynamics slightly improved while the moments of inertia suffered. Trial 3 failed the standard deviation criterion and therefore, did not converge on a solution in under 200 iterations (48 minutes). In fact, the Trial 3 run reached a constant $\sigma_{resid} = 0.32618$ meters (for the $n = 2$ data set) at iteration 76 until program termination at iteration 200. With two data sets used in this estimation attempt and after convergence was reached for this trial (using the same *a prior* information) in Case II, it is unlikely that solution ambiguity is the primary fault. The other explanation for this failed attempt may be that the moments of inertia are not fully observable. This possible cause is first apparent in this case.

4.5.4 Case IV. In Appendix C, the results of a fourth case are provided. This extra case uses the same initial conditions and filter settings as the previous 12-State cases; however, three batches of data are processed together. The results of this case are closer to the true values than Case III (12-State), emphasizing the improved accuracy using multiple data sets in the estimation process for the 12-State vector

version. However, the outcome was not successful for the 9-State estimation cases. Using the same settings as in Case II and III (9-State), and making use of a third data set, the estimator did not achieve convergence within the specified criteria and all three trials failed. Details of these runs are found in Appendix C. All three trials failed as a result of the residual distribution of the second data set (associated with $n = 2$). With $\sigma_{resid} \approx 0.327$, similar to Case III (9-State), the convergence criterion was not satisfied for any of the three trials in 200 iterations. It is interesting to note that convergence failure was attributed to data set two and that σ_{resid} for all three trials were nearly equal. This is the first case where the introduction of an additional data set actually resulted in poor performance and estimation failure for all trials. With three data sets, it is difficult to associate the failure mechanism completely to solution ambiguity. In fact, with this case it is more apparent that the moments of inertia may simply not be observable.

4.5.5 Comparison of 12-State Cases. Table 4.24 compares the 12-State estimate errors in terms of the number of data sets processed. As mentioned in the results, the 12-State estimate using one data set took 200 iterations until program termination. The 12-State estimation runs using two and three data sets converged in 13 iterations (approximately 130 seconds). The table illustrates the improvement in estimation accuracy as the number of data sets used is increased and solution ambiguity is decreased.

4.5.6 Comparison of 9-State Cases. A similar comparison can be made using Tables 4.17, 4.23, and the results presented in Appendix C. This section will compare each 9-State estimation trial separately. For each trail, a comparison of the number of data sets used and the resulting error will be made. For Trial 1, the *a priori* estimates for the MOI have an initial error of 10% from the true values. The average MOI errors (the average of components A, B, and C together) for runs made using 1, 2, and 3 data sets are 11%, 26%, and 37%, respectively. In this case, the

Table 4.24 12-State Estimation Error Summary

State	Estimate Error		
	1 Data Set [Case II]	2 Data Sets [Case III]	3 Data Sets [Case IV]
$\delta x \quad [m]$	35.9%	0.02%	0%
$\delta y \quad [m]$	204.9%	0.08%	0%
$\delta z \quad [m]$	52.5%	0.1%	0.0002%
$\delta \dot{x} \quad [m/s]$	122%	0%	0%
$\delta \dot{y} \quad [m/s]$	309%	0%	0%
$\delta \dot{z} \quad [m/s]$	59%	0%	0%
$\omega_1 \quad [rad/s]$	0.0148	0.0000	0.0000
$\omega_2 \quad [rad/s]$	0.0434	0.0000	0.0000
$\omega_3 \quad [rad/s]$	0.0392	0.0000	0.0000
$\theta_1 \quad [rad]$	4.7289	0.0006	0.0001
$\theta_2 \quad [rad]$	0.9465	0.0004	0.0001
$\theta_3 \quad [rad]$	8.5974	0.0008	0.0018

MOI error using a single data set is close to the *a priori* error of 10%. Otherwise, increasing the number of data sets processed increased the moments of inertia error overall while the error for the rotational states slightly decreased.

For Trial 2, the initial *a priori* estimates for the MOI have an error of 20%. In this case, the average MOI error for estimation runs made with 1, 2, and 3 data sets are 20%, 17%, and 18%, respectively. Increasing the number of data batches processed did not improve the moments of inertia estimates yet it slightly improved the rotational dynamics estimates. The average MOI error is relatively close to the *a priori* MOI error.

Trial 3 uses initial values for the moments of inertia which are 30% in error from the true values. In this Trial the two runs using multiple data sets (from Cases III and IV) failed to converge. The average MOI errors for estimation runs involving 1, 2, and 3 data sets are 30%, 34%, and 34%. Once again, the average error is comparable to the initial error used to begin the estimation process.

4.6 Summary of Results

From the data presented here, it can be seen that multiple solutions that satisfy the convergence criteria do in fact exist for this scenario. The solution uncertainty can be significantly reduced while improving solution accuracy for the estimation of the 12-State vector by processing multiple data sets (as shown in the 12-State estimation cases). It can be said that accurate estimation of the relative motion and rotational states proved to be possible. The direct estimation of the moments of inertia however, proved to be more of a challenge with relatively lower accuracy than the other estimated states if the convergence criteria was even achieved. This may be partially due to the existence of multiple solutions but more importantly, the lack of observability of the moments of inertia is the likely cause. If the moments of inertia are not fully observable based on range measurements, the estimator would then not be fully capable of accurately estimating the MOI (based on the equations of motion) yielding poor results for the 9-State solutions. In such a case, processing multiple data sets affects only solution ambiguity but does not improve observability. This explanation best fits the results seen by this research for the 9-State vector estimation runs. Slight improvements in the rotational dynamics are seen which can be attributed to the reduction of multiple solutions using the additional data sets. Unlike the improving rotational state estimates, the additional data sets do not improve the MOI estimates. This conclusion will be discussed further in the next Chapter. Note that for all of the MOI estimates (successful and unsuccessful), the components are all positive and they all satisfy the true MOI relation of $A > B > C$. Therefore, although the individual components of the moment-of-inertia matrix are not well estimated, the proper relationship associated with the major, minor, and intermediate axes of inertia of the simulated Resident Space Object are maintained.

V. Conclusions & Recommendations

5.1 Summary

This thesis demonstrates the basic ability to accurately estimate the relative motion and rotational dynamics of a simulated Resident Space Object using a non-linear least squares estimation filter based on range observations collected during a proximity mission. However, the feasibility of accurately estimating the moments of inertia properties of the RSO is questionable and proved to be challenging. In fact, this research concludes that the moments of inertia of the RSO may not be fully observable using range observations alone. This thesis indicates that processing multiple data batches significantly reduces solution ambiguity and improves estimation accuracy, as seen with the 12-State vector estimation cases. Conclusions from these estimated solutions can be drawn to further improve the understanding of the dynamical and physical properties of the RSO.

5.2 Conclusions

This research indicates that implementing a nonlinear least squares estimator can successfully result in an estimated solution for the relative motion dynamics, rotational dynamics, and moments of inertia of an RSO with certain limitations. The results from Case 1A and Case II (12-State) illustrate the critical role the initial *a priori* estimates play in the overall success or failure of the estimation attempt. The existence of multiple estimation solutions may prove to be quite problematic in the case of an *uncooperative* RSO. One must discern between multiple solutions that are all mathematically valid and the single solution representative of the true states. This is challenging when the luxury of knowing the truth is not always realistic. However taking multiple range measurements of tracked points on the RSO body provides multiple data sets. Each data set significantly reduces the solution ambiguity as shown in the RSS surface plots and demonstrated in Case III and IV

(12-State). This can further enhance one's estimation attempt and increase solution believability and accuracy.

In this research the limitation of estimating the dynamical properties of the RSO is limited to the deterministic two body motion developed in Chapter 2. This is well suited for estimating the dynamics where the RSO is a small heavenly body (e.g. an asteroid). However, when the RSO is a manmade spacecraft, this quickly becomes a complex problem. RSO motion not fully described by classic two-body dynamics would not be suited for the estimator used in this research. Thruster firings for maneuvering or station-keeping, energy dissipation, and external perturbations are all realistic contributors to the overall RSO dynamics, which are not captured by this ideal model. From the model used in this research, and from the simulation, one can say that the simulated RSO is rotating primarily about two axes at certain estimated angular velocities (ω_1 and ω_3). At any instant in time, one could predict the orientation of the RSO body. Also, with some knowledge of the moments of inertia, the geometry, and the estimated angular velocities, one can conclude that the RSO is spinning primarily about its major axis of inertia and is therefore, in a relatively stable state. This study concludes that the relative position, relative velocity, angular velocity, and orientation angle states can be accurately estimated using the 12-State vector version by processing multiple range data sets.

Perhaps a more challenging task is to gain knowledge of the physical properties of a RSO. This is true for both heavenly bodies as well as *uncooperative* Targets. At a very basic level, this research shows that *some* knowledge of the physical properties must be known or estimated beforehand. The RSO center-of-mass location is of key importance to the following: the CW equations (for relative motion dynamics), the coordinate frame transformations, the observational points measured from the CM, and finally, for the moment-of-inertia components themselves. The 9-State cases in this thesis demonstrate that the direct estimation of the moments of inertia using range measurements alone is problematic. This research concludes that the moments

of inertia may not be fully observable using the current dynamics model and range observations. In this case, the use of multiple data sets simply improves solution ambiguity (as seen in the rotational states) but does not affect observability (as seen in the error of the MOI estimates). The quality of the MOI estimated results proved to be directly related to the quality of the *a priori* initial guess. Therefore, a more detailed study is required to examine the observability conditions and expressions needed to accurately and directly estimate the moments of inertia.

5.3 Contributions

In the field of spacecraft proximity operations, this research illustrates the application and performance of a nonlinear least squares estimation filter for relative motion and rotational dynamics using range observations made by a spacecraft in the vicinity of a RSO. Perhaps of more significance, this study exposes the limitations of the implemented dynamics model and estimator in regard to the observability of the moments of inertia of the Resident Space Object.

5.4 Recommendations

There are several areas in which additional research would be worthwhile to pursue with this baseline ability established. Continuing with this nonlinear least squares estimation approach, it would be of benefit to employ some realism to both the truth model and the data sets. This would include incorporating J_2 perturbations, solar radiation pressure, and perhaps, atmospheric drag. To make the truth model robust and versatile it would be beneficial to use quaternions to describe the Target's orientation and avoid singularity limitations. This research used data sets which have data points at constant time intervals. It would be of interest to study the effects of using data sets with measurements not taken entirely at constant time intervals. This would simulate an intermittent data acquisition stream as well as blackout periods when the tracked point is not visible to the sensor due to physi-

cal obstruction. This leads to additional research in the amount of data needed for successfully estimating the true states. LIDAR sensors which are now being used frequently in rendezvous and proximity operations can provide data in a range and two angle set or in a range vector set [12]. Introducing directional information into the data would certainly refine the estimate and also reduce solution ambiguity. Additionally, researching how the selected locations of the observational points on the RSO affect the estimator's results would prove beneficial. Of significant importance, research should be conducted into the observability of the moments of inertia.

It would of interest to incorporate an extended Kalman filter into this estimation process. This would simply involve a rearrangement and modification of the existing matrices in the estimator code. Using at least two data sets for some batch size, a least squares estimation is performed and at some point handed over to the Kalman filter to continue the estimation of the state variables. This would be very useful in the 12-State variable case.

Appendix A. Linearized Observation

This appendix contains the calculations used to develop the partial derivatives which are used to calculate the **H** matrix. Beginning with the derived range observation function

$$\mathbf{G} = r_n = \sqrt{(p_{x_n} - \delta x)^2 + (p_{y_n} - \delta y)^2 + (p_{z_n} - \delta z)^2} \tag{A.1}$$

where the subscript n denotes observation point number n. Recall the definition

$$\mathbf{H}_i(t_i) \equiv \frac{\partial \mathbf{G}}{\partial \mathbf{X}}(\mathbf{X}_{ref}(t_i), t_i) \tag{A.2}$$

Note that the range equation above is a function of δx, δy, δz, p_{x_n}, p_{y_n}, and p_{z_n}. In terms of the dynamics state variables, the range equation is only a function of δx, δy, δz, θ_1, θ_2, and θ_3. For simplicity, all other state variables which the range equation is not a function of are ignored till the end. This results in

$$\mathbf{H} = \frac{\partial \mathbf{G}}{\partial \mathbf{X}} = \begin{bmatrix} \frac{\partial \mathbf{G}}{\partial \delta x} & \frac{\partial \mathbf{G}}{\partial \delta y} & \frac{\partial \mathbf{G}}{\partial \delta z} & \frac{\partial \mathbf{G}}{\partial \theta_1} & \frac{\partial \mathbf{G}}{\partial \theta_2} & \frac{\partial \mathbf{G}}{\partial \theta_3} \end{bmatrix} \tag{A.3}$$

Recalling that p_{x_n}, p_{y_n}, and p_{z_n} are functions of the Euler angles due to the rotation of the Target body, the **H** matrix can simply be found using the chain rule in the following fashion

$$\mathbf{H} = \begin{bmatrix} \frac{\partial \mathbf{G}}{\partial \delta x} & \frac{\partial \mathbf{G}}{\partial \delta y} & \frac{\partial \mathbf{G}}{\partial \delta z} & \frac{\partial \mathbf{G}}{\partial p_{x_n}} & \frac{\partial \mathbf{G}}{\partial p_{y_n}} & \frac{\partial \mathbf{G}}{\partial p_{z_n}} \end{bmatrix} \begin{bmatrix} 1 & 0 & 0 & 0 & 0 & 0 \\ 0 & 1 & 0 & 0 & 0 & 0 \\ 0 & 0 & 1 & 0 & 0 & 0 \\ 0 & 0 & 0 & \frac{\partial p_{x_n}}{\partial \theta_1} & \frac{\partial p_{x_n}}{\partial \theta_2} & \frac{\partial p_{x_n}}{\partial \theta_3} \\ 0 & 0 & 0 & \frac{\partial p_{y_n}}{\partial \theta_1} & \frac{\partial p_{y_n}}{\partial \theta_2} & \frac{\partial p_{y_n}}{\partial \theta_3} \\ 0 & 0 & 0 & \frac{\partial p_{z_n}}{\partial \theta_1} & \frac{\partial p_{z_n}}{\partial \theta_2} & \frac{\partial p_{z_n}}{\partial \theta_3} \end{bmatrix} \tag{A.4}$$

To compute the partial derivatives recall that

$$\|\mathbf{r}_n^e\| = \|[\mathbf{R}^{eb}]\mathbf{R}_n^b - \delta\boldsymbol{\rho}^e\| \tag{A.5}$$

where the position vector in the orbital frame of the observation point is defined as

$$\mathbf{R}_n^e = [\mathbf{R}^{eb}]\mathbf{R}_n^b \tag{A.6}$$

define the position vector in $\mathfrak{F}_e$ as

$$\mathbf{R}_n^e = \begin{Bmatrix} p_{x_n} \\ p_{y_n} \\ p_{z_n} \end{Bmatrix} \tag{A.7}$$

define the position vector in $\mathfrak{F}_b$ as

$$\mathbf{R}_n^b = \begin{Bmatrix} b_{1_n} \\ b_{2_n} \\ b_{3_n} \end{Bmatrix} \tag{A.8}$$

Then substituting the vector definitions into Equation A.6 yields

$$\begin{Bmatrix} p_{x_n} \\ p_{y_n} \\ p_{z_n} \end{Bmatrix} = \begin{bmatrix} \mathrm{c}_2\mathrm{c}_3 & \mathrm{s}_1\mathrm{s}_2\mathrm{c}_3 - \mathrm{c}_1\mathrm{s}_3 & \mathrm{c}_1\mathrm{s}_2\mathrm{c}_3 + \mathrm{s}_1\mathrm{s}_3 \\ \mathrm{c}_2\mathrm{s}_3 & \mathrm{s}_1\mathrm{s}_2\mathrm{s}_3 + \mathrm{c}_1\mathrm{c}_3 & \mathrm{c}_1\mathrm{s}_2\mathrm{s}_3 - \mathrm{s}_1\mathrm{c}_3 \\ -\mathrm{s}_2 & \mathrm{s}_1\mathrm{c}_2 & \mathrm{c}_1\mathrm{c}_2 \end{bmatrix} \begin{Bmatrix} b_{1_n} \\ b_{2_n} \\ b_{3_n} \end{Bmatrix} \tag{A.9}$$

carrying out the matrix multiplication results in the following set of equations

$$\begin{Bmatrix} p_{x_n} \\ p_{y_n} \\ p_{z_n} \end{Bmatrix} = \begin{bmatrix} b_{1_n}\mathrm{c}_2\mathrm{c}_3 + b_{2_n}(\mathrm{s}_1\mathrm{s}_2\mathrm{c}_3 - \mathrm{c}_1\mathrm{s}_3) + b_{3_n}(\mathrm{c}_1\mathrm{s}_2\mathrm{c}_3 + \mathrm{s}_1\mathrm{s}_3) \\ b_{1_n}\mathrm{c}_2\mathrm{s}_3 + b_{2_n}(\mathrm{s}_1\mathrm{s}_2\mathrm{s}_3 + \mathrm{c}_1\mathrm{c}_3) + b_{3_n}(\mathrm{c}_1\mathrm{s}_2\mathrm{s}_3 - \mathrm{s}_1\mathrm{c}_3) \\ -b_{1_n}\mathrm{s}_2 + b_{2_n}\mathrm{s}_1\mathrm{c}_2 + b_{3_n}\mathrm{c}_1\mathrm{c}_2 \end{bmatrix} \tag{A.10}$$

Taking the partial derivatives of each equation with respect to θ_1, θ_2, θ_3 results in

$$\frac{\partial p_{x_n}}{\partial \theta_1} = b_{2_n}\mathrm{s}_2\mathrm{c}_3\mathrm{c}_1 + b_{2_n}\mathrm{s}_3\mathrm{s}_1 - b_{3_n}\mathrm{s}_2\mathrm{c}_3\mathrm{s}_1 + b_{3_n}\mathrm{c}_1\mathrm{s}_3 \tag{A.11}$$

$$\frac{\partial p_{x_n}}{\partial \theta_2} = -b_{1_n}\mathrm{c}_3\mathrm{s}_2 + b_{2_n}\mathrm{s}_1\mathrm{c}_2\mathrm{c}_3 + b_{3_n}\mathrm{c}_1\mathrm{c}_2\mathrm{c}_3 \tag{A.12}$$

$$\frac{\partial p_{x_n}}{\partial \theta_3} = -b_{1_n}\mathrm{c}_2\mathrm{s}_3 - b_{2_n}\mathrm{s}_1\mathrm{s}_2\mathrm{s}_3 - b_{2_n}\mathrm{c}_1\mathrm{c}_3 - b_{3_n}\mathrm{c}_1\mathrm{s}_2\mathrm{s}_3 + b_{3_n}\mathrm{s}_1\mathrm{c}_3 \tag{A.13}$$

$$\frac{\partial p_{y_n}}{\partial \theta_1} = b_{2_n}\mathrm{c}_1\mathrm{s}_2\mathrm{s}_3 - b_{2_n}\mathrm{s}_1\mathrm{c}_3 - b_{3_n}\mathrm{s}_1\mathrm{s}_2\mathrm{s}_3 - b_{3_n}\mathrm{c}_1\mathrm{c}_3 \tag{A.14}$$

$$\frac{\partial p_{y_n}}{\partial \theta_2} = -b_{1_n}\mathrm{s}_2\mathrm{s}_3 + b_{2_n}\mathrm{s}_1\mathrm{c}_2\mathrm{s}_3 + b_{3_n}\mathrm{c}_1\mathrm{c}_2\mathrm{s}_3 \tag{A.15}$$

$$\frac{\partial p_{y_n}}{\partial \theta_3} = b_{1_n}\mathrm{c}_2\mathrm{c}_3 + b_{2_n}\mathrm{s}_1\mathrm{s}_2\mathrm{c}_3 - b_{2_n}\mathrm{c}_1\mathrm{s}_3 + b_{3_n}\mathrm{c}_1\mathrm{s}_2\mathrm{c}_3 + b_{3_n}\mathrm{s}_1\mathrm{s}_3 \tag{A.16}$$

$$\frac{\partial p_{z_n}}{\partial \theta_1} = b_{2_n}\mathrm{c}_1\mathrm{c}_2 - b_{3_n}\mathrm{s}_1\mathrm{c}_2 \tag{A.17}$$

$$\frac{\partial p_{z_n}}{\partial \theta_2} = -b_{1_n}\mathrm{c}_2 - b_{2_n}\mathrm{s}_1\mathrm{s}_2 - b_{3_n}\mathrm{c}_1\mathrm{s}_2 \tag{A.18}$$

$$\frac{\partial p_{z_n}}{\partial \theta_3} = 0 \tag{A.19}$$

Now taking the partial derivatives of the range function, Equation A.1, with respect to δx, δy, and δz results in

$$\frac{\partial \mathbf{G}}{\partial \delta x} = \frac{\delta x - p_{x_n}}{\sqrt{(p_{x_n} - \delta x)^2 + (p_{y_n} - \delta y)^2 + (p_{z_n} - \delta z)^2}} \tag{A.20}$$

$$\frac{\partial \mathbf{G}}{\partial \delta y} = \frac{\delta y - p_{y_n}}{\sqrt{(p_{x_n} - \delta x)^2 + (p_{y_n} - \delta y)^2 + (p_{z_n} - \delta z)^2}} \tag{A.21}$$

$$\frac{\partial \mathbf{G}}{\partial \delta z} = \frac{\delta z - p_{z_n}}{\sqrt{(p_{x_n} - \delta x)^2 + (p_{y_n} - \delta y)^2 + (p_{z_n} - \delta z)^2}} \tag{A.22}$$

These 12 partial derivatives are coded into a MATLAB function file in the form of Equation A.4. The computer carries out the matrix multiplication, and by the chain rule, solves for the **H** matrix. Depending on which version of the state matrix is used, the program forms the proper version of the **H** matrix.

For the 12-state vector version defined as

$$\mathbf{X} = \left[\begin{array}{cccccccccccc} \delta x & \delta y & \delta z & \delta \dot{x} & \delta \dot{y} & \delta \dot{z} & \omega_1 & \omega_2 & \omega_3 & \theta_1 & \theta_2 & \theta_3 \end{array} \right]^T$$

the linearized observation function is the solution to

$$\mathbf{H} = \left[\begin{array}{cccccccccccc} \frac{\partial \mathbf{G}}{\partial \delta x} & \frac{\partial \mathbf{G}}{\partial \delta y} & \frac{\partial \mathbf{G}}{\partial \delta z} & 0 & 0 & 0 & 0 & 0 & 0 & \frac{\partial \mathbf{G}}{\partial \theta_1} & \frac{\partial \mathbf{G}}{\partial \theta_2} & \frac{\partial \mathbf{G}}{\partial \theta_3} \end{array} \right] \tag{A.23}$$

For the 9-state vector version defined as

$$\mathbf{X} = \left[\begin{array}{ccccccccc} \omega_1 & \omega_2 & \omega_3 & \theta_1 & \theta_2 & \theta_3 & A & B & C \end{array} \right]^T$$

the linearized observation function is the solution to

$$\mathbf{H} = \left[\begin{array}{ccccccccc} 0 & 0 & 0 & \frac{\partial \mathbf{G}}{\partial \theta_1} & \frac{\partial \mathbf{G}}{\partial \theta_2} & \frac{\partial \mathbf{G}}{\partial \theta_3} & 0 & 0 & 0 \end{array} \right] \tag{A.24}$$

Appendix B. Linearized Dynamics

Recall an analytical solution to the Clohessy-Wiltshire equations exists. This solution was presented in the form of a state transition matrix, $\mathbf{\Phi}_{cw}$, in Chapter 2. Therefore, the state transition matrix for the rotational portion of the dynamics is in need. As defined in Chapter 2, the rotational state vector is

$$\mathbf{X}_{rot}(t) = \begin{bmatrix} \omega_1 & \omega_2 & \omega_3 & \theta_1 & \theta_2 & \theta_3 \end{bmatrix}^T \tag{B.1}$$

The time-derivative of the rotational state vector is then given below. The vector function, $\mathbf{f}$, is then associated with each state equation of motion.

$$\dot{\mathbf{X}}_{rot}(t) = \begin{Bmatrix} \dot{\omega}_1 \\ \dot{\omega}_2 \\ \dot{\omega}_3 \\ \dot{\theta}_1 \\ \dot{\theta}_2 \\ \dot{\theta}_3 \end{Bmatrix} = \begin{Bmatrix} f_1 \\ f_2 \\ f_3 \\ f_4 \\ f_5 \\ f_6 \end{Bmatrix} = \mathbf{f} \tag{B.2}$$

The A matrix is defined as the matrix containing the partial derivatives of the equations of motion with respect to the state variables.

$$A = \begin{bmatrix} \frac{\partial f_1}{\partial \omega_1} & \frac{\partial f_1}{\partial \omega_2} & \frac{\partial f_1}{\partial \omega_3} & \frac{\partial f_1}{\partial \theta_1} & \frac{\partial f_1}{\partial \theta_2} & \frac{\partial f_1}{\partial \theta_3} \\ \frac{\partial f_2}{\partial \omega_1} & \frac{\partial f_2}{\partial \omega_2} & \frac{\partial f_2}{\partial \omega_3} & \frac{\partial f_2}{\partial \theta_1} & \frac{\partial f_2}{\partial \theta_2} & \frac{\partial f_2}{\partial \theta_3} \\ \frac{\partial f_3}{\partial \omega_1} & \frac{\partial f_3}{\partial \omega_2} & \frac{\partial f_3}{\partial \omega_3} & \frac{\partial f_3}{\partial \theta_1} & \frac{\partial f_3}{\partial \theta_2} & \frac{\partial f_3}{\partial \theta_3} \\ \frac{\partial f_4}{\partial \omega_1} & \frac{\partial f_4}{\partial \omega_2} & \frac{\partial f_4}{\partial \omega_3} & \frac{\partial f_4}{\partial \theta_1} & \frac{\partial f_4}{\partial \theta_2} & \frac{\partial f_4}{\partial \theta_3} \\ \frac{\partial f_5}{\partial \omega_1} & \frac{\partial f_5}{\partial \omega_2} & \frac{\partial f_5}{\partial \omega_3} & \frac{\partial f_5}{\partial \theta_1} & \frac{\partial f_5}{\partial \theta_2} & \frac{\partial f_5}{\partial \theta_3} \\ \frac{\partial f_6}{\partial \omega_1} & \frac{\partial f_6}{\partial \omega_2} & \frac{\partial f_6}{\partial \omega_3} & \frac{\partial f_6}{\partial \theta_1} & \frac{\partial f_6}{\partial \theta_2} & \frac{\partial f_6}{\partial \theta_3} \end{bmatrix} = \left[\begin{array}{c|c} A_{11} & 0^{3\times 3} \\ \hline A_{21} & A_{22} \end{array}\right] \tag{B.3}$$

The A matrix is partitioned in for clarity. The partial derivatives comprising each sub-matrix are given as

$$A_{11} = \begin{bmatrix} 0 & \frac{B-C}{A}\omega_3 & \frac{B-C}{A}\omega_2 \\ \frac{C-A}{B}\omega_3 & 0 & \frac{C-A}{B}\omega_1 \\ \frac{A-B}{C}\omega_2 & \frac{A-B}{C}\omega_1 & 0 \end{bmatrix} \tag{B.4}$$

$$A_{21} = \begin{bmatrix} 1 & \mathrm{s}_1\mathrm{t}_2 & \mathrm{c}_1\mathrm{t}_2 \\ 0 & \mathrm{c}_1 & -\mathrm{s}_1 \\ 0 & \mathrm{s}_1\sec_2 & \mathrm{c}_1\sec_2 \end{bmatrix} \tag{B.5}$$

$$A_{22} = \begin{bmatrix} \omega_2\mathrm{c}_1\mathrm{t}_2 - \omega_3\mathrm{t}_2\mathrm{s}_1 & \omega_2\mathrm{s}_1\sec_2^2 + \omega_3\mathrm{c}_1\sec_2^2 & 0 \\ -\omega_2\mathrm{s}_1 - \omega_3\mathrm{c}_1 & 0 & 0 \\ \omega_2\mathrm{c}_1\sec_2 - \omega_3\mathrm{s}_1\sec_2 & \omega_2\mathrm{s}_1\sec_2\mathrm{t}_2 + \omega_3\mathrm{c}_1\sec_2\mathrm{t}_2 & 0 \end{bmatrix} \tag{B.6}$$

where $\mathrm{s}_x = \sin\theta_x$, $\mathrm{c}_x = \cos\theta_x$, $\mathrm{t}_x = \tan\theta_x$, $\sec_x = \sec\theta_x$, and $\sec_x^2 = \sec^2\theta_x$. These partial derivatives are coded into a MATLAB function file for the A matrix.

The state transition matrix for the rotational portion is defined as

$$\mathbf{\Phi}_{rot} = \begin{bmatrix} \phi_{11} & \phi_{12} & \phi_{13} & \phi_{14} & \phi_{15} & \phi_{16} \\ \phi_{21} & \phi_{22} & \phi_{23} & \phi_{24} & \phi_{25} & \phi_{26} \\ \phi_{31} & \phi_{32} & \phi_{33} & \phi_{34} & \phi_{35} & \phi_{36} \\ \phi_{41} & \phi_{42} & \phi_{43} & \phi_{44} & \phi_{45} & \phi_{46} \\ \phi_{51} & \phi_{52} & \phi_{53} & \phi_{54} & \phi_{55} & \phi_{56} \\ \phi_{61} & \phi_{62} & \phi_{63} & \phi_{64} & \phi_{65} & \phi_{66} \end{bmatrix} \tag{B.7}$$

and the time-derivative of the state transition matrix is simply defined as

$$\dot{\mathbf{\Phi}}_{rot} = \begin{bmatrix} \dot{\phi}_{11} & \dot{\phi}_{12} & \dot{\phi}_{13} & \dot{\phi}_{14} & \dot{\phi}_{15} & \dot{\phi}_{16} \\ \dot{\phi}_{21} & \dot{\phi}_{22} & \dot{\phi}_{23} & \dot{\phi}_{24} & \dot{\phi}_{25} & \dot{\phi}_{26} \\ \dot{\phi}_{31} & \dot{\phi}_{32} & \dot{\phi}_{33} & \dot{\phi}_{34} & \dot{\phi}_{35} & \dot{\phi}_{36} \\ \dot{\phi}_{41} & \dot{\phi}_{42} & \dot{\phi}_{43} & \dot{\phi}_{44} & \dot{\phi}_{45} & \dot{\phi}_{46} \\ \dot{\phi}_{51} & \dot{\phi}_{52} & \dot{\phi}_{53} & \dot{\phi}_{54} & \dot{\phi}_{55} & \dot{\phi}_{56} \\ \dot{\phi}_{61} & \dot{\phi}_{62} & \dot{\phi}_{63} & \dot{\phi}_{64} & \dot{\phi}_{65} & \dot{\phi}_{66} \end{bmatrix} \tag{B.8}$$

The matrices above are coded into the estimation program and using a Runga-Kutta algorithm, the numerical solution to

$$\dot{\mathbf{\Phi}}_{rot}(t, t_0) = A(t)\mathbf{\Phi}_{rot}(t, t_0) \tag{B.9}$$

is solved for resulting in $\mathbf{\Phi}_{rot}(t, t_0)$. Incorporating the CW portion results in the 12×12 state transition matrix for the 12-state vector version used in the estimation process

$$\mathbf{\Phi} \quad = \quad \left[\begin{array}{c|c} \mathbf{\Phi}_{cw}^{6\times 6} & 0^{6\times 6} \\ \hline 0^{6\times 6} & \mathbf{\Phi}_{rot}^{6\times 6} \end{array}\right] \tag{B.10}$$

In a similar fashion, the 9-state vector version of the A matrix and the state transition matrix $\mathbf{\Phi}$ is found. This section should be treated separate from the 12-state version above. Re-defining similar variables, omitting the CW portion of the state vector, and including the moment-of-inertia variables, the 9-state version is formed. Beginning with the 9-state vector defined as

$$\mathbf{X} = \begin{bmatrix} \omega_1 & \omega_2 & \omega_3 & \theta_1 & \theta_2 & \theta_3 & A & B & C \end{bmatrix}^T$$

the time-derivative of the state variables are taken resulting in

$$\dot{\mathbf{X}}(t) = \begin{Bmatrix} \dot{\omega}_1 \\ \dot{\omega}_2 \\ \dot{\omega}_3 \\ \dot{\theta}_1 \\ \dot{\theta}_2 \\ \dot{\theta}_3 \\ \dot{A} \\ \dot{B} \\ \dot{C} \end{Bmatrix} = \begin{Bmatrix} f_1 \\ f_2 \\ f_3 \\ f_4 \\ f_5 \\ f_6 \\ f_7 \\ f_8 \\ f_9 \end{Bmatrix} = \mathbf{f} \tag{B.11}$$

The 9-state version of the A matrix is defined as

$$A = \begin{bmatrix} \frac{\partial f_1}{\partial \omega_1} & \frac{\partial f_1}{\partial \omega_2} & \frac{\partial f_1}{\partial \omega_3} & \frac{\partial f_1}{\partial \theta_1} & \frac{\partial f_1}{\partial \theta_2} & \frac{\partial f_1}{\partial \theta_3} & \frac{\partial f_1}{\partial A} & \frac{\partial f_1}{\partial B} & \frac{\partial f_1}{\partial C} \\ \frac{\partial f_2}{\partial \omega_1} & \frac{\partial f_2}{\partial \omega_2} & \frac{\partial f_2}{\partial \omega_3} & \frac{\partial f_2}{\partial \theta_1} & \frac{\partial f_2}{\partial \theta_2} & \frac{\partial f_2}{\partial \theta_3} & \frac{\partial f_2}{\partial A} & \frac{\partial f_2}{\partial B} & \frac{\partial f_2}{\partial C} \\ \frac{\partial f_3}{\partial \omega_1} & \frac{\partial f_3}{\partial \omega_2} & \frac{\partial f_3}{\partial \omega_3} & \frac{\partial f_3}{\partial \theta_1} & \frac{\partial f_3}{\partial \theta_2} & \frac{\partial f_3}{\partial \theta_3} & \frac{\partial f_3}{\partial A} & \frac{\partial f_3}{\partial B} & \frac{\partial f_3}{\partial C} \\ \frac{\partial f_4}{\partial \omega_1} & \frac{\partial f_4}{\partial \omega_2} & \frac{\partial f_4}{\partial \omega_3} & \frac{\partial f_4}{\partial \theta_1} & \frac{\partial f_4}{\partial \theta_2} & \frac{\partial f_4}{\partial \theta_3} & \frac{\partial f_4}{\partial A} & \frac{\partial f_4}{\partial B} & \frac{\partial f_4}{\partial C} \\ \frac{\partial f_5}{\partial \omega_1} & \frac{\partial f_5}{\partial \omega_2} & \frac{\partial f_5}{\partial \omega_3} & \frac{\partial f_5}{\partial \theta_1} & \frac{\partial f_5}{\partial \theta_2} & \frac{\partial f_5}{\partial \theta_3} & \frac{\partial f_5}{\partial A} & \frac{\partial f_5}{\partial B} & \frac{\partial f_5}{\partial C} \\ \frac{\partial f_6}{\partial \omega_1} & \frac{\partial f_6}{\partial \omega_2} & \frac{\partial f_6}{\partial \omega_3} & \frac{\partial f_6}{\partial \theta_1} & \frac{\partial f_6}{\partial \theta_2} & \frac{\partial f_6}{\partial \theta_3} & \frac{\partial f_6}{\partial A} & \frac{\partial f_6}{\partial B} & \frac{\partial f_6}{\partial C} \\ \frac{\partial f_7}{\partial \omega_1} & \frac{\partial f_7}{\partial \omega_2} & \frac{\partial f_7}{\partial \omega_3} & \frac{\partial f_7}{\partial \theta_1} & \frac{\partial f_7}{\partial \theta_2} & \frac{\partial f_7}{\partial \theta_3} & \frac{\partial f_7}{\partial A} & \frac{\partial f_7}{\partial B} & \frac{\partial f_7}{\partial C} \\ \frac{\partial f_8}{\partial \omega_1} & \frac{\partial f_8}{\partial \omega_2} & \frac{\partial f_8}{\partial \omega_3} & \frac{\partial f_8}{\partial \theta_1} & \frac{\partial f_8}{\partial \theta_2} & \frac{\partial f_8}{\partial \theta_3} & \frac{\partial f_8}{\partial A} & \frac{\partial f_8}{\partial B} & \frac{\partial f_8}{\partial C} \\ \frac{\partial f_9}{\partial \omega_1} & \frac{\partial f_9}{\partial \omega_2} & \frac{\partial f_9}{\partial \omega_3} & \frac{\partial f_9}{\partial \theta_1} & \frac{\partial f_9}{\partial \theta_2} & \frac{\partial f_9}{\partial \theta_3} & \frac{\partial f_9}{\partial A} & \frac{\partial f_9}{\partial B} & \frac{\partial f_9}{\partial C} \end{bmatrix} = \left[\begin{array}{c|c} A_{rot}^{6\times 6} & \begin{array}{c} B^{3\times 3} \\ \hline 0^{3\times 3} \end{array} \\ \hline 0^{3\times 9} & \end{array}\right] \tag{B.12}$$

The sub-matrix $A_{rot}^{6\times 6}$ is further partitioned into

$$A_{rot}^{6\times 6} = \left[\begin{array}{c|c} A_{11} & 0^{3\times 3} \\ \hline A_{21} & A_{22} \end{array}\right] \tag{B.13}$$

where sub-matrices A_{11}, A_{21}, A_{22}, are equal to Equations B.4, B.5, and B.6, respectively. The solution to sub-matrix B is

$$B^{3\times3} = \begin{bmatrix} -\frac{(B-C)}{A^2}\omega_2\omega_3 & \frac{1}{A}\omega_2\omega_3 & -\frac{1}{A}\omega_2\omega_3 \\ -\frac{1}{B}\omega_1\omega_3 & -\frac{(C-A)}{B^2}\omega_1\omega_3 & \frac{1}{B}\omega_1\omega_3 \\ \frac{1}{C}\omega_1\omega_2 & -\frac{1}{C}\omega_1\omega_2 & -\frac{(A-B)}{C^2}\omega_1\omega_2 \end{bmatrix} \tag{B.14}$$

This completes the solution to the 9×9 matrix A . The 9×9 state transition matrix is then defined as

$$\mathbf{\Phi} = \begin{bmatrix} \phi_{11} & \phi_{12} & \phi_{13} & \phi_{14} & \phi_{15} & \phi_{16} & \phi_{17} & \phi_{18} & \phi_{19} \\ \phi_{21} & \phi_{22} & \phi_{23} & \phi_{24} & \phi_{25} & \phi_{26} & \phi_{27} & \phi_{28} & \phi_{29} \\ \phi_{31} & \phi_{32} & \phi_{33} & \phi_{34} & \phi_{35} & \phi_{36} & \phi_{37} & \phi_{38} & \phi_{39} \\ \phi_{41} & \phi_{42} & \phi_{43} & \phi_{44} & \phi_{45} & \phi_{46} & \phi_{47} & \phi_{48} & \phi_{49} \\ \phi_{51} & \phi_{52} & \phi_{53} & \phi_{54} & \phi_{55} & \phi_{56} & \phi_{57} & \phi_{58} & \phi_{59} \\ \phi_{61} & \phi_{62} & \phi_{63} & \phi_{64} & \phi_{65} & \phi_{66} & \phi_{67} & \phi_{68} & \phi_{69} \\ \phi_{71} & \phi_{72} & \phi_{73} & \phi_{74} & \phi_{75} & \phi_{76} & \phi_{77} & \phi_{78} & \phi_{79} \\ \phi_{81} & \phi_{82} & \phi_{83} & \phi_{84} & \phi_{85} & \phi_{86} & \phi_{87} & \phi_{88} & \phi_{89} \\ \phi_{91} & \phi_{92} & \phi_{93} & \phi_{94} & \phi_{95} & \phi_{96} & \phi_{97} & \phi_{98} & \phi_{99} \end{bmatrix} \tag{B.15}$$

and the time-derivative of the state transition matrix is defined as

$$\dot{\mathbf{\Phi}} = \begin{bmatrix} \dot{\phi}_{11} & \dot{\phi}_{12} & \dot{\phi}_{13} & \dot{\phi}_{14} & \dot{\phi}_{15} & \dot{\phi}_{16} & \dot{\phi}_{17} & \dot{\phi}_{18} & \dot{\phi}_{19} \\ \dot{\phi}_{21} & \dot{\phi}_{22} & \dot{\phi}_{23} & \dot{\phi}_{24} & \dot{\phi}_{25} & \dot{\phi}_{26} & \dot{\phi}_{27} & \dot{\phi}_{28} & \dot{\phi}_{29} \\ \dot{\phi}_{31} & \dot{\phi}_{32} & \dot{\phi}_{33} & \dot{\phi}_{34} & \dot{\phi}_{35} & \dot{\phi}_{36} & \dot{\phi}_{37} & \dot{\phi}_{38} & \dot{\phi}_{39} \\ \dot{\phi}_{41} & \dot{\phi}_{42} & \dot{\phi}_{43} & \dot{\phi}_{44} & \dot{\phi}_{45} & \dot{\phi}_{46} & \dot{\phi}_{47} & \dot{\phi}_{48} & \dot{\phi}_{49} \\ \dot{\phi}_{51} & \dot{\phi}_{52} & \dot{\phi}_{53} & \dot{\phi}_{54} & \dot{\phi}_{55} & \dot{\phi}_{56} & \dot{\phi}_{57} & \dot{\phi}_{58} & \dot{\phi}_{59} \\ \dot{\phi}_{61} & \dot{\phi}_{62} & \dot{\phi}_{63} & \dot{\phi}_{64} & \dot{\phi}_{65} & \dot{\phi}_{66} & \dot{\phi}_{67} & \dot{\phi}_{68} & \dot{\phi}_{69} \\ \dot{\phi}_{71} & \dot{\phi}_{72} & \dot{\phi}_{73} & \dot{\phi}_{74} & \dot{\phi}_{75} & \dot{\phi}_{76} & \dot{\phi}_{77} & \dot{\phi}_{78} & \dot{\phi}_{79} \\ \dot{\phi}_{81} & \dot{\phi}_{82} & \dot{\phi}_{83} & \dot{\phi}_{84} & \dot{\phi}_{85} & \dot{\phi}_{86} & \dot{\phi}_{87} & \dot{\phi}_{88} & \dot{\phi}_{89} \\ \dot{\phi}_{91} & \dot{\phi}_{92} & \dot{\phi}_{93} & \dot{\phi}_{94} & \dot{\phi}_{95} & \dot{\phi}_{96} & \dot{\phi}_{97} & \dot{\phi}_{98} & \dot{\phi}_{99} \end{bmatrix} \tag{B.16}$$

The A, $\mathbf{\Phi}$, and $\dot{\mathbf{\Phi}}$ matrices above are coded into the estimation program and using a Runga-Kutta numerical integration algorithm, the numerical solution to

$$\dot{\mathbf{\Phi}}(t, t_0) = A(t)\mathbf{\Phi}(t, t_0) \tag{B.17}$$

is solved for. This results in the numerical solution of the 9×9 state transition matrix $\mathbf{\Phi}(t, t_0)$ for the 9-variable state vector.

Appendix C. Additional Data

Truth Model Data

The Truth Model program settings and constants are shown in Figure C.17

```
================================================================================
                        CONSTANTS & USER PARAMETERS
================================================================================
 mu, Earth = 398600.44 [km^3/sec^2]           Radius of Earth, Re =  6378.14 [km]
 Mean Orb Motion, Target = 1.0381e-003 [rad/s]     Orbital Period =     6052 [s]
 Target Altitude         =  800.00 [km]
 Tgt Orbit Incl          = 28.50 [deg]             Tgt Orbit RAAN = 0.00 [deg]
 Assumed Target MOI:   A =  45.0000          B =  30.0000       C =  15.0000

================================================================================
                        INITIAL STATE CONDITIONS
================================================================================
 POSITION [m]      VELOCITY [m/s]        ANGULAR VEL [rad/s]     EULER ANGLE [rad]
--------------------------------------------------------------------------------
 dx= 50.0000      dx_dot= 0.0100        omega1= 0.01000000       th1= 0.00000000
 dy= 50.0000      dy_dot= 0.0100        omega2= 0.00000000       th2= 0.00000000
 dz= 50.0000      dz_dot= 0.0100        omega3= 0.00100000       th3= 0.00000000

================================================================================
 # of ORBITAL PERIODS      START TIME [s]      END TIME [s]      Int Step-Size [s]
--------------------------------------------------------------------------------
        1.0000               0.0000            6052.0000              1.0000
```

Figure C.1 Truth Model

Case I Additional Data

Additional data from Case 1A are provided in the figures below.

Case II Additional Data

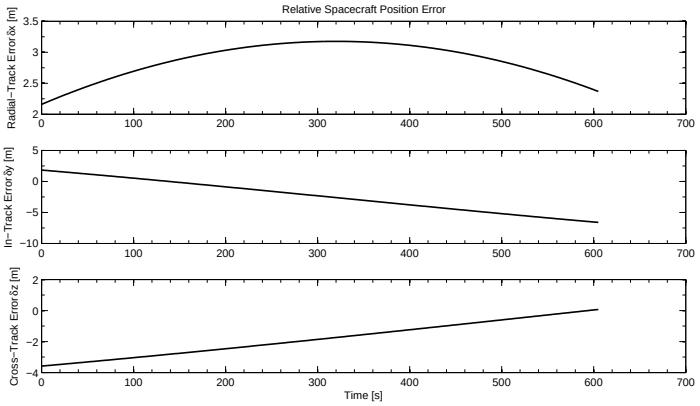

Figure C.2 Case I: True Error of Relative Position Estimates

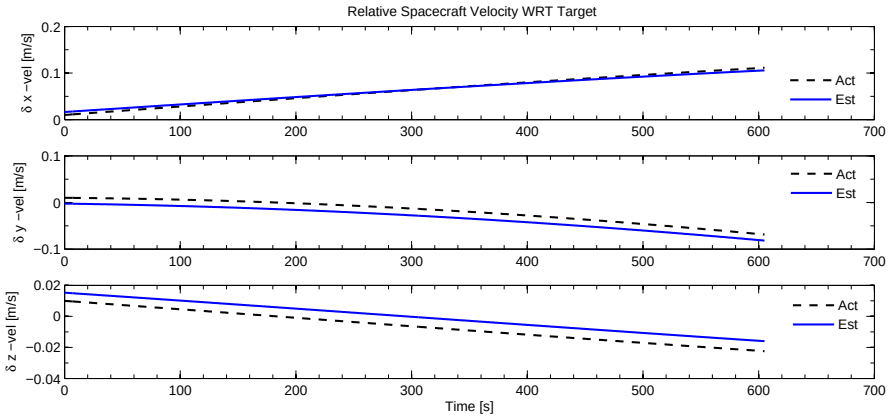

Figure C.3 Case I: Estimated Relative Velocity States

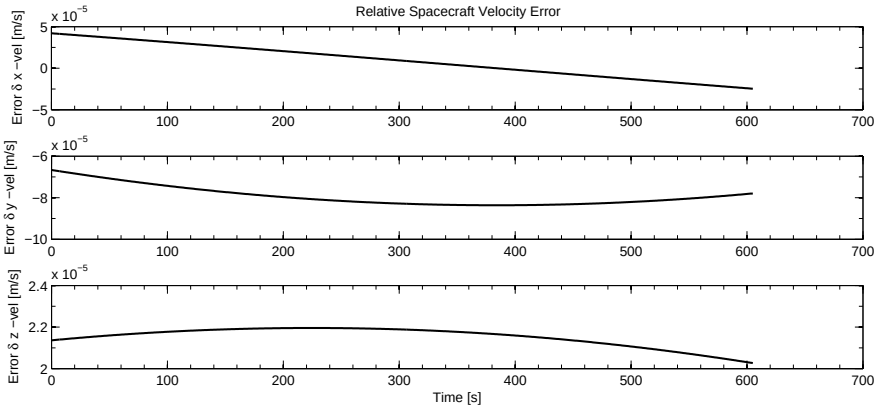

Figure C.4 Case I: True Error of Relative Velocity Estimates

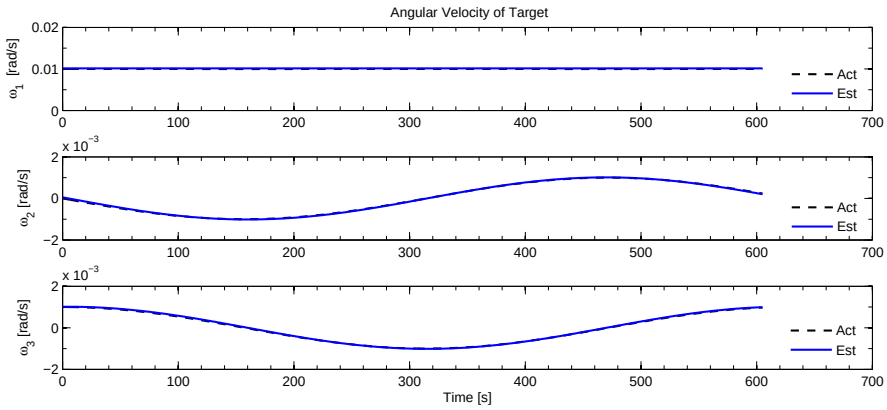

Figure C.5 Case I: Estimated Angular Velocity States

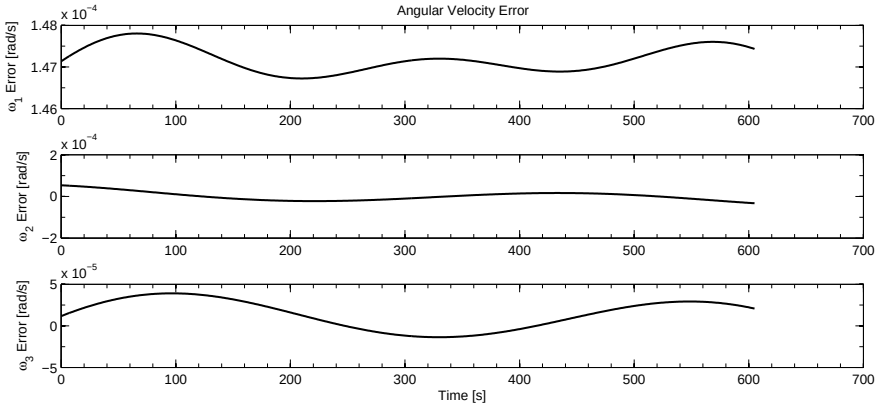

Figure C.6 Case I: True Error of Angular Velocity Estimates

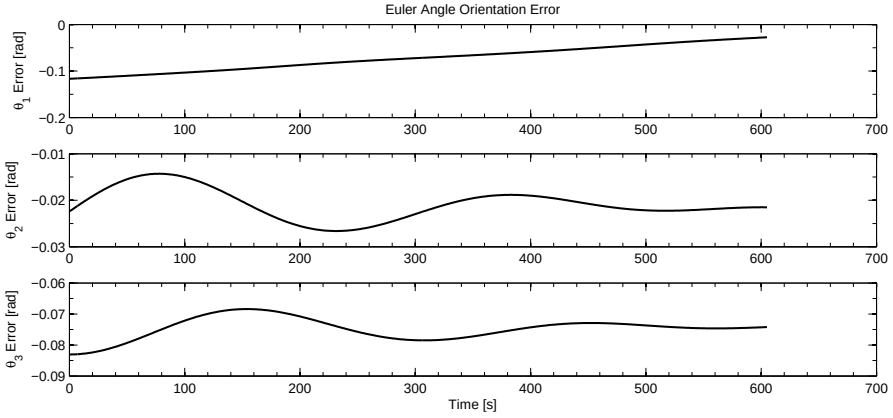

Figure C.7 Case I: True Error of Euler Orientation Angle Estimates

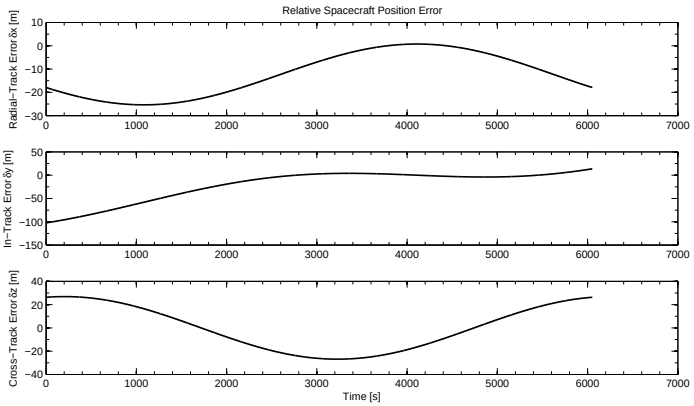

Figure C.8 Case II: True Error of Relative Position Estimates(12-State)

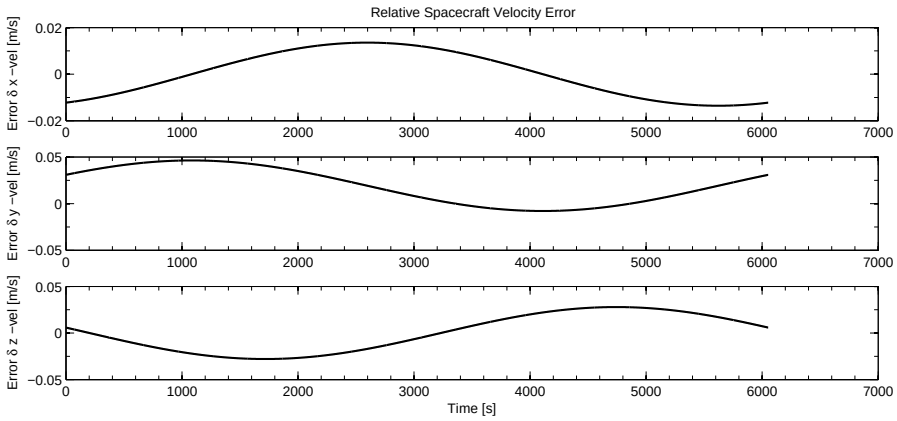

Figure C.9 Case II: True Error of Relative Velocity Estimates (12-State)

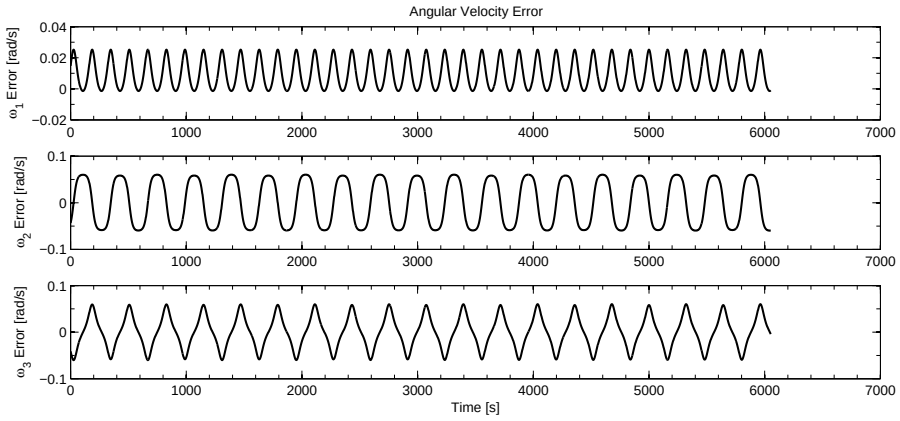

Figure C.10 Case II: True Error of Angular Velocity Estimates (12-State)

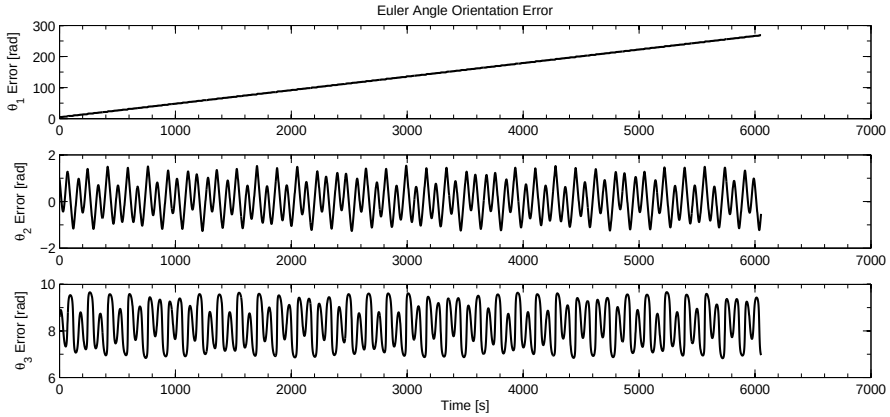

Figure C.11 Case II: True Error of Euler Orientation Angle Estimates (12-State)

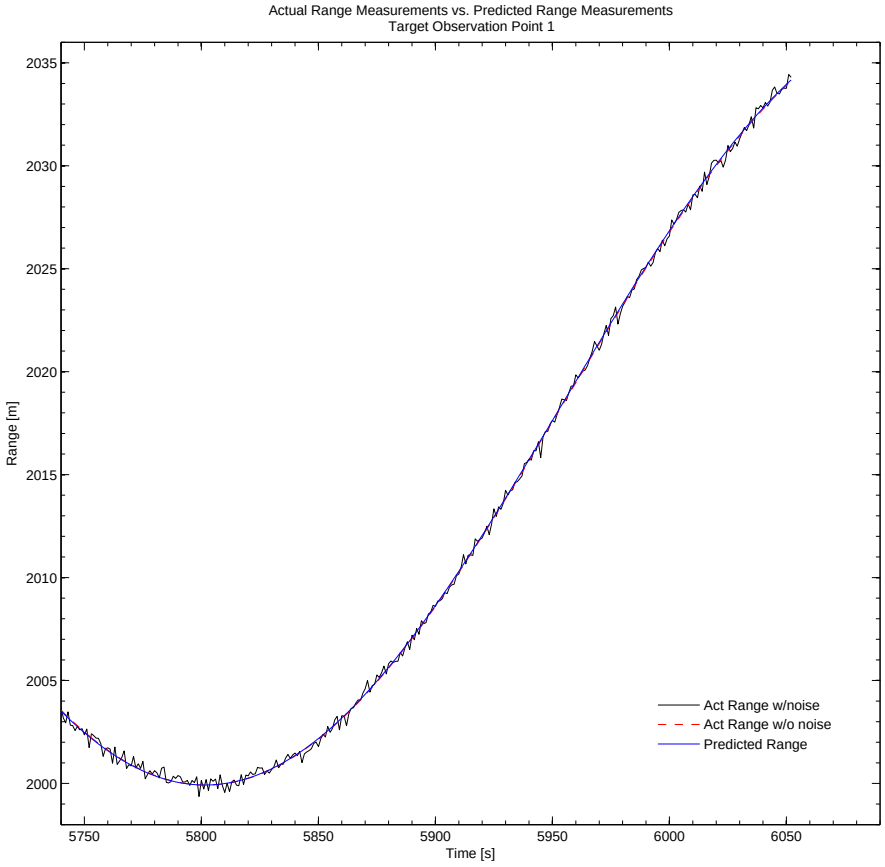

Figure C.12 Case II: Range Profile Close-Up View (9-State)

Case III Additional Data

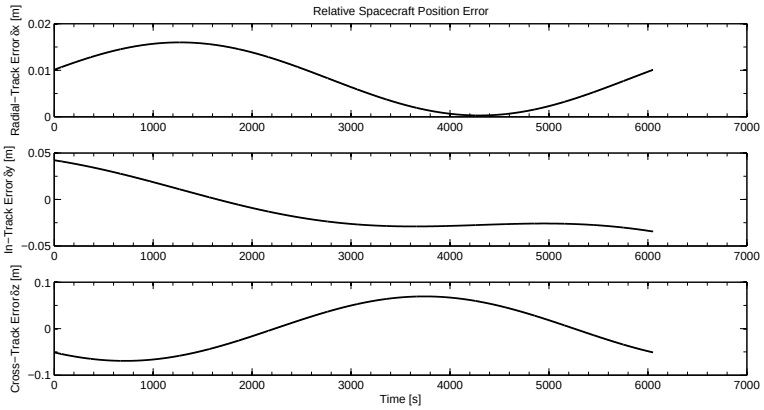

Figure C.13 Case III: True Error of Relative Position (12-State)

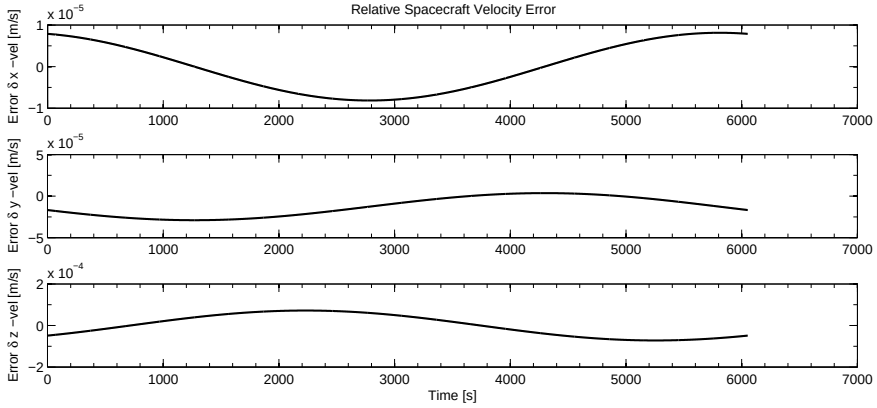

Figure C.14 Case III: True Error of Relative Velocity (12-State)

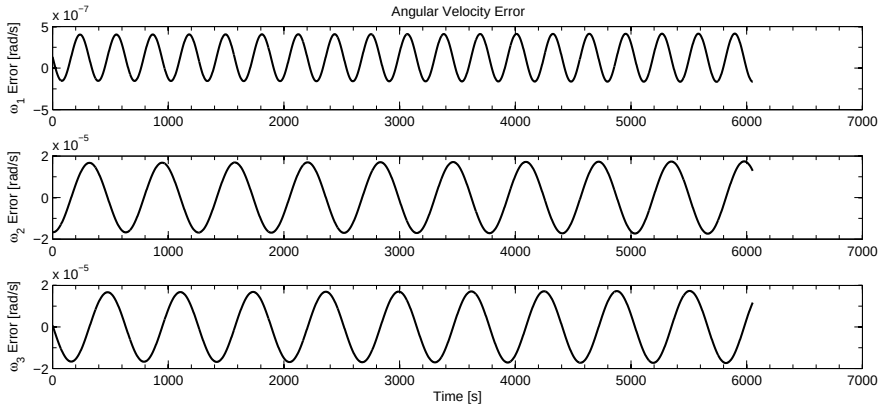

Figure C.15 Case III: True Error of Angular Velocities (12-State)

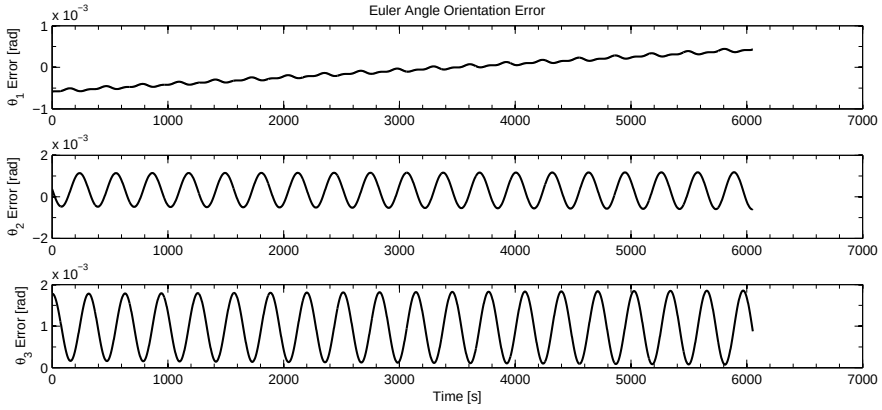

Figure C.16 Case III: True Error of Euler Orientation Angles (12-State)

Case IV Data

```
================================================================================
                              RANGE DATA TO PROCESS
================================================================================
 Number of Observations =     6053     Obs Time-Step = 1.00 [s]
 Start Epoch Obs Time = 0.00 [s]   End Obs Time = 6052.00 [s]

================================================================================
                              FILTER PERFORMANCE
================================================================================
 Convergence Status: DID CONVERGE
 Filter Terminated on Iteration Number:     13
 Standard Deviation of Data Residuals from Final Iteration: 0.2479376954
 Standard Deviation of Data Residuals from Final Iteration: 0.2496057646
 Standard Deviation of Data Residuals from Final Iteration: 0.2522780251
 CPU Processing Time = 129.26714852 [s]

********************************************************************************
                          N-LSQ ESTIMATOR RESULTS
********************************************************************************

 POSITION [m]      VELOCITY [m/s]        ANGULAR VEL [rad/s]     EULER ANGLE [rad]
--------------------------------------------------------------------------------
 dx= 50.00097336     dxdot= 0.01000286      omg1= 0.00999977      th1= -0.00007261
 dy= 50.00165926     dydot= 0.00999858      omg2= -0.00001788      th2= 0.00009480
 dz= 49.99363954     dzdot= 0.00996686      omg3= 0.00100841      th3= 0.00176362

Version: 12-State Vector Mode>>
```

Figure C.17 Case IV: Estimation Results

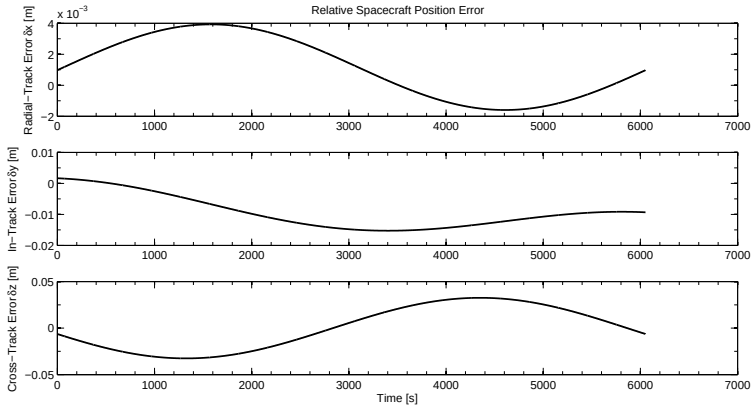

Figure C.18 Case IV: True Error of Relative Position Estimates (12-State)

All three cases satisfied the covariance criterion at approximately iteration 10. The standard deviation criterion was *not* satisfied for any of the three trials. Interestingly, the σ_{resid} for all three data sets, and for all three trials, remained approximately constant to 4 significant digits near iteration 15 till program termination at $i_{max} = 200$. The similar estimated values for the rotational states, regardless of

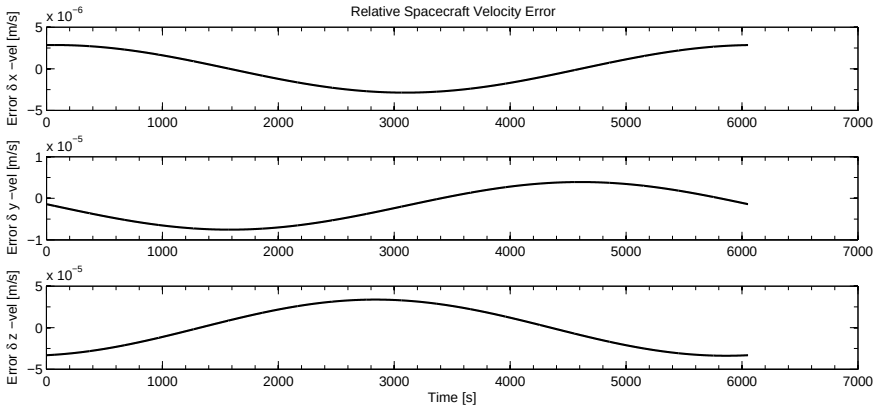

Figure C.19 Case IV: True Error of Relative Velocity Estimates (12-State)

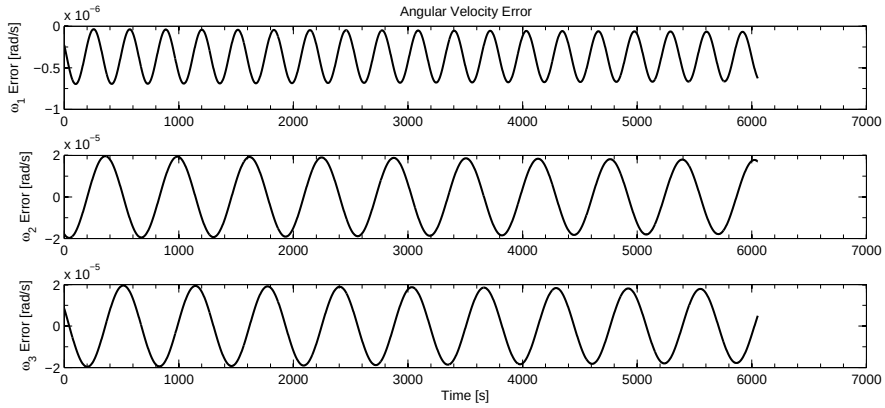

Figure C.20 Case IV: True Error of Angular Velocity Estimates (12-State)

the MOI, might suggest a multiple solution. It is also possible that the differential equations for the MOI components are the cause. Closer investigation should be accomplished to determine the cause of these solutions which seem to be reaching some limit of accuracy with respect to the residuals. Completing a RSS surface plot for this case might provide insight to this unpredicted behavior. It would be interesting to use data sets from other points to see if the apparent σ_{resid} limits changes. It should be mentioned that different values of k_1 were tried with no significant change in the outcome.

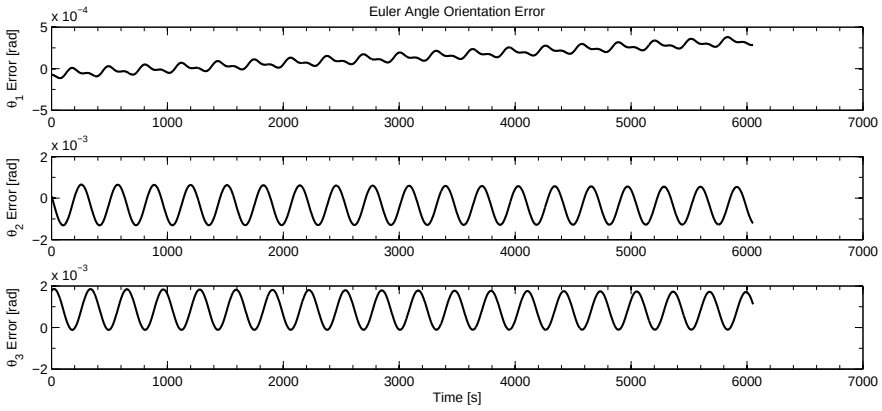

Figure C.21 Case IV: True Error of Euler Angle Estimates (12-State)

Table C.1 Case IV: Estimated 9-State Results at Epoch

Variable	Estimates			Truth
	Trial 1 [10% MOI Error]	*Trial 2* [20% MOI Error]	*Trial 3* [30% MOI Error]	
ω_1 $[rad/s]$	0.0100	0.0100	0.0100	0.01
ω_2 $[rad/s]$	0.0001	0.0000	0.0000	0
ω_3 $[rad/s]$	-0.0001	-0.0001	0.0000	.001
θ_1 $[rad]$	0.0004	0.0004	0.0000	0
θ_2 $[rad]$	-0.0107	-0.0107	-0.0091	0
θ_3 $[rad]$	-0.0100	0.0007	0.0005	0
A $[m^2kg]$	46.68	54.55	58.07	45
B $[m^2kg]$	40.62	34.99	40.01	30
C $[m^2kg]$	4.09	12.50	9.08	15
$\sigma_{resid_{n=1}}$ $[m]$	0.257	0.257	0.257	0.248
$\sigma_{resid_{n=2}}$ $[m]$	0.323	0.327	0.327	0.247
$\sigma_{resid_{n=3}}$ $[m]$	0.287	0.285	0.285	0.250
iterations	200	200	200	-
processing time [s]	2535	2436	2659	-

Bibliography

1. Scheeres, D.J. "Close Proximity Operations for Implementing Mitigation Strategies". AIAA Planetary Defense Conference, Orange County CA, 2004.
2. Zimpfer D., S. Tuohy, P. Kackmar. "Autonomous Rendezvous, Capture, and In-Space Assembly: Past, Present, and Future". Space Exploration Conference, Orlando FL, 2005.
3. Agency, Japan Aerospace Exploration. "Missions: Hayabusa (MUSES-C)", 2006.
4. Bilstein, Roger E. *Flight in America: From the Wrights to the Astronauts*. John Hopkins University Press, Baltimore MD, 3 edition, 2001.
5. Siddiqi, Asif A. *Sputnik and the Soviet Space Challenge*. University Press of Florida, Gainesville FL, 2003.
6. Aeronautics, National and (NASA), Space Administration. "Mission Archives: STS-51I". www.nasa.gov, 2006.
7. Air Force Researh Laboratory, Space Vehicle Directorate. "Fact Sheet: XSS-11 Micro Satellite", December 2005.
8. Aeronautics, National and (NASA), Space Administration. "Mission Archives: Hayabusa (MUSES-C)". www.jpl.nasa.gov, 2006.
9. Wiesel, William E. *Space Flight Dynamics*. McGraw-Hill Co., New York NY, 2 edition, 1997.
10. Feucht, Uwe. "Seminar: Fundamentals of Attitude". European Space Operation Centre, European Space Agency, Darmstadt, Germany, May 2006.
11. S. Kim, Y. Cheng A. Fosbury J. Junkins, J. Crassidis. "Kalman Filtering for Relative Spacecraft Attitude and Position Estimation". *AIAA Guidance, Navigation, and Control*, 2005. AIAA Paper 2005-6087.
12. F. Pelletier, A. Allen, D. Golla. "Lidar-based Rendezvous Navigation for MSR". AIAA/AAS Astrodynamics Specialist Conference and Exhibit, Providence RI, 2004.
13. D. Scheeres, S. Ostro L. Benner, S. Broschart. "The Dynamical Environment about Asteroid 25143 Itokawa: Target of the Hayabusa Mission". AIAA/AAS Astrodynamics Specialist Conference and Exhibit, Providence RI, 2004.
14. Wie, Bong. *Space Vehicle Dynamics and Control*. American Institute of Aeronautics and Astronautics, Inc., Reston VA, 1998.

15. Wiesel, William E. *Modern Orbit Determination*. Aphelion Press, Beavercreek OH, 1 edition, 2003.

16. Meirovitch, Leonard. *Methods of Analytical Dynamics*. Dover Publications, Inc., Mineola NY, 1998.

17. Curtis, Howard D. "Introduction to Space Mechanics", 2002. Course Booklet, Embry-Riddle Aeronautical University.

18. Schaub, H. "Relative Orbit Geometry Through Classical Orbit Differences". *Journal of Guidance, Control, and Dynamics*, 2004.

19. Clohessy, W.H. and Wiltshire, R.S. "Terminal Guidance System for Satellite Rendezvous". *Journal of the Aerospace Sciences*, 1960.

20. Wiesel, William E. *Modern Astrodynamics*. Aphelion Press, Beavercreek OH, 1 edition, 2003.

21. Walpole, Myers, Myers and Ye. *Probablity and Statistics for Engineers and Scientists*. Prentice Hall, Upper Saddle River NJ, 7 edition, 2002.

22. City of Goettingen, Gauss-Gesellschaft e.V. and of Goettingen, G.-A. University. "Gauss 2005". www.gaussjahr.de, 2005.

23. Lexikon, THG. "Method of Least Squares". www.tomshardware.de/lexikon/Methode_ der_ kleinsten_ Quadrate.

24. T. Mizuno, E. Okumura M. Nakayama, K. Tsuno. "LIDAR in Hayabusa Mission". Presentation by JAXA/NEC/Toshiba, 2006.

25. Inc., Optech. "Intelligent Laser Ranging and Imaging System". Technical Specification Document, 2006.

26. D. Mehrholz, W. Flury R. Jehn H. Klinkrad M. Landgraf, L. Leushacke. "Detecting, Tracking and Imaging Space Debris". *Eurpean Space Agency Bulletin 109*, 2002.

27. Leushacke, L. "100 Years of Radar, TIRA, FGAN-FHR". Presentation, 2004.

28. O'Hair, J. "Introduction to Radar and Synthetic Aperture Radar Systems". National Geospatial Intelligence School, CMSR, 2006.

Vita

Lt Abraham Franz Brunner attended Martin-Luther Gymnasium, Germany, and King George High School, Virginia. He began his undergraduate study at Embry-Riddle Aeronautical University, Daytona Beach, Florida while also working at the Naval Surface Warfare Center, Dahlgren, Virginia, as an Engineering Technician and Analyst in the Standard Missile Lethality & Weapons Effectiveness Branch. Upon graduation with a Bachelor of Science degree in Aerospace Engineering, he received his commission in the U.S. Air Force in 2003. His first assignment was at Vandenberg A.F.B. in Lompoc, California, where he served as a Launch Vehicle Engineer and Launch Group Mission Manager. He was accepted into the National Reconnaissance Office Advanced Academic Degree Program in 2004. One year later, he was assigned to the Air Force Institute of Technology, Dayton, Ohio, to receive his Master of Science degree in Astronautical Engineering. Upon graduation, Lt Brunner will be assigned to the Headquarters of the National Reconnaissance Office in Chantilly, Virginia.

REPORT DOCUMENTATION PAGE

Form Approved
OMB No. 0704–0188

1. REPORT DATE *(DD–MM–YYYY)*	2. REPORT TYPE	3. DATES COVERED *(From — To)*
22–03–2007	Master's Thesis	Sep 2005 – Mar 2007

4. TITLE AND SUBTITLE

SPACECRAFT PROXIMITY OPERATIONS USED TO ESTIMATE THE DYNAMICAL & PHYSICAL PROPERTIES OF A RESIDENT SPACE OBJECT

5a. CONTRACT NUMBER

5b. GRANT NUMBER

5c. PROGRAM ELEMENT NUMBER

6. AUTHOR(S)

Brunner, Abraham F., 1Lt, USAF

5d. PROJECT NUMBER

5e. TASK NUMBER

5f. WORK UNIT NUMBER

7. PERFORMING ORGANIZATION NAME(S) AND ADDRESS(ES)

Air Force Institute of Technology
Graduate School of Engineering and Management
2950 Hobson Way, Building 640
WPAFB OH 45433-7765

8. PERFORMING ORGANIZATION REPORT NUMBER

AFIT/GA/ENY/07-M03

9. SPONSORING / MONITORING AGENCY NAME(S) AND ADDRESS(ES)

N/A

10. SPONSOR/MONITOR'S ACRONYM(S)

11. SPONSOR/MONITOR'S REPORT NUMBER(S)

12. DISTRIBUTION / AVAILABILITY STATEMENT

APPROVAL FOR PUBLIC RELEASE; DISTRIBUTION IS UNLIMITED.

13. SUPPLEMENTARY NOTES

14. ABSTRACT

When conducting a space proximity operation, developing high-fidelity estimates of the dynamical and physical properties of a Resident Space Object (RSO) based on post-rendezvous observational data acquired, is imperative for the understanding of the RSO itself and the operating environment. This research investigates the estimation of relative motion dynamics, rotational dynamics, and the feasibility of estimating the moments of inertia of a RSO. Using the Hill-Clohessy-Wiltshire equations, rigid-body dynamics, and estimation theory, a nonlinear least squares estimation algorithm is implemented in the processing of range data from tracked observation points on the RSO body. Through simulation, it was determined that accurately estimating the relative motion and rotational dynamics is possible. However directly estimating the moments of inertia using range data proved to be problematic and exposed a possible observability limitation. Yet in general, the solutions were heavily dependent on the quality of the a priori knowledge as well as the reduction of solution ambiguity through the use of multiple observational data sets.

15. SUBJECT TERMS

Proximity Operation, Least Squares, Estimation, Relative Motion, LIDAR, Resident Space Object, Rotational Dynamics, Clohessy-Wiltshire, Euler Angle Kinematics

16. SECURITY CLASSIFICATION OF:			17. LIMITATION OF ABSTRACT	18. NUMBER OF PAGES	19a. NAME OF RESPONSIBLE PERSON
a. REPORT	b. ABSTRACT	c. THIS PAGE			Dr. William E. Wiesel, USAF (AFIT/ENY)
U	U	U	U	147	19b. TELEPHONE NUMBER *(include area code)* (937) 255–6565, ext 4312